CERN–2013–006
EuCARD-CON-2014-001
21 November 2013

ORGANISATION EUROPÉENNE POUR LA RECHERCHE NUCLÉAIRE
CERN EUROPEAN ORGANIZATION FOR NUCLEAR RESEARCH

WAMSDO: Workshop on Accelerator Magnet Superconductors, Design and Optimization

CERN, Switzerland, 15–16 January 2013

Proceedings

Editor: E. Todesco

GENEVA
2013

ISBN 978–92–9083–394–9
ISSN 0007–8328
DOI 10.5170/CERN–2013–006

Copyright © CERN, 2013

Creative Commons Attribution 3.0

Knowledge transfer is an integral part of CERN's mission.

CERN publishes this report Open Access under the Creative Commons Attribution 3.0 license (`http://creativecommons.org/licenses/by/3.0/`) in order to permit its wide dissemination and use.

This report should be cited as:

Proceedings of WAMSDO: Workshop on accelerator magnet superconductors, design and optimization edited by E. Todesco, CERN-2013-006 (CERN, Geneva, 2013), DOI: 10.5170/CERN–2013–006

A contribution in this report should be cited as:

[Author name(s)], in Proceedings of WAMSDO: Workshop on accelerator magnet superconductors, design and optimization, edited by E. Todesco, CERN-2013-006 (CERN, Geneva, 2013), pp. [first page]–[last page], DOI: 10.5170/CERN-2013-006.[firstpage]

Abstract

This report contains the proceedings of the Workshop on Accelerator Magnet Superconductor, Design and Optimization (WAMSDO) held at CERN from 15 to 16 January 2013. This fourth edition of the WAMSDO workshop is focussed on aspects related to quench protection.

Preface

This is the fourth workshop on magnet design organized in the framework of the European Programmes FP6 and FP7. The first workshop, WAMS, was focused on superconductors; the second one, WAMDO, on magnet design and optimization; in the third one, WAMSDO, we included both aspects, to make the present status and to draw perspectives for the future R&D activities. This fourth workshop is focussed on a special topic, namely quench protection in superconducting magnets for particle accelerators. Quench protection has been identified as a critical aspect, and maybe a possible showstopper, for future accelerator magnet based on Nb_3Sn technology. In these magnets, the energy density is about 50 % larger than in the Nb-Ti magnets, and the reaction time is reduced from the 100-200 ms of Nb-Ti to about 50 ms. This is imposing very strong requirements on the protection system performance and reliability. An additional critical issue is the detection time in HTS superconductors, where the large temperature margins correspond to quench propagation velocities about 100 slower than in Nb-Ti and Nb_3Sn. This makes the quench detection a very critical issue in HTS magnets.

We start with an overview of the quench phenomena, summarizing the physics and the main equations, and setting the scene for the accelerator magnets which have been built in the past, based on Nb-Ti, and for the future devices relying on Nb_3Sn (see the contributions from L. Bottura and E. Todesco). Nb_3Sn magnets will work with high energy densities, typically 1.5 to twice larger than the Nb-Ti cases, and in many cases cannot rely on an energy extraction. This makes the quench protection of these devices more challenging, requiring to reach unprecedented capabilities of detection, reaction time and quench heater performance.

An overview of the requirements and of the present state of the art for Nb-Ti magnets is given in the contribution of G. Kirby. The experience gathered in three Nb_3Sn programs, namely the triplet and the 11 T dipole for the LHC upgrade, and the Fresca2 test facility, are given in the papers of G. Ambrosio, G. Chaladize and P. Fazilleau. An overview of the modeling tools which are available is given in the contribution of H. Felice. Most accelerator magnets are protected through quench heaters, which are fired as soon as the quench is detected, and that should quench all the magnet as fast as possible to provoke the rapid rise of the resistance. An essential brick of this problem is the capability of understanding the process of quench induced by the quench heaters, which is covered both from an experimental and modeling point of view by T. Salmi. Several new techniques are being developed to face the increasing challenges of quench protection: the contribution of M. Marchevsky is focussed on the acoustic detection, which is being tested on Nb_3Sn magnets.

HTS poses special problems to quench protection, due to its large temperature margin with quench propagation velocities which are 100 times smaller than low temperature superconductors as Nb-Ti or Nb_3Sn. The resistance growth is so slow that quench detection becomes the problem. The case of HTS is treated in the papers of J. Schwartz and A. Stenvall. Finally, the efficiency of the quench protection relies on the low resistivity of the stabilizer, typically copper. This property can be modified in the environment of the accelerator, especially for the magnets closer to the interaction points. The contribution of R. Flukinger addresses this issue, setting the scene for the case of the LHC luminosity upgrade.

Further information on the workshop can be accessed from its home web site,
`http://indico.cern.ch/conferenceDisplay.py?confId=28832`.

Conference organizing committee: G. De Rijk, H. Felice, T. Ogitsu, M. Sorbi, F. Rodrigues-Mateos.

These proceedings have been published in paper and electronic form.

Electronic copies can be retrieved through:
`https://indico.cern.ch/conferenceDisplay.py?ovw=True&confId=199910`.

The compilation of these proceedings would not have been possible without the help of the conveners and speakers. The organizational support by the workshop secretary Rachelle Decreuse is also gratefully acknowledged. In particular, we would like to thank all the participants for their stimulating contributions and lively discussions.

The WAMSDO workshop was sponsored and supported by the European Community-Research Infrastructure Activity under the FP7 project HiLumi LHC, GA no. 284404, co-funded by the DoE, USA and KEK, Japan. It was co-funded by the European Commission under the FP7 Research Infrastructures project EuCARD, grant agreement no. 227579.

Geneva, 31 June 2013

E. Todesco

Contents

Magnet quench 101 *L. Bottura* 1
Quench protection for the LHC[1] *A. Verweij*
Quench limits in the next generation of magnets *E. Todesco* 10
New ideas on quench detection and protection[1] *G. De Rijk*
Quench protection analysis in accelerator magnets, a review of the tools *H. Felice* 17
Quench in high temperature superconductor magnets *J. Schwartz* 21
Modeling heat transfer from quench protection heaters to superconducting cables in Nb_3Sn magnets
T. Salmi 30
Acoustic detection in superconducting magnets for performance characterization and diagnostics
M. Marchevsky 38
Propagation speed[1] *H. Ten Kate*
Quenching HTS coils[1] *M. Dalban-Canassy*
Maximum allowable temperature during quench in Nb_3Sn accelerator magnets *G. Ambrosio* 43
Experimental results and analysis from the 11 T DS Nb_3Sn dipole *G. Chlachidze* 47
Models and experimental results from the wide aperture Nb-Ti magnets for the LHC upgrade *G. Kirby* 57
Protection of the 13 T Nb_3Sn Fresca II dipole *P. Fazilleau* 65
Protection of the 6 T YBCO insert in the 13 T Nb_3Sn Fresca II dipole *A. Stenvall* 70
The behaviour of copper in view of radiation damage in the LHC luminosity upgrade *R. Flukiger* 76

[1] A paper was not submitted to the proceedings. However, the slides presented are available in electronic form at `http://indico.cern.ch/conferenceDisplay.py?confId=199910`.

MAGNET QUENCH 101

L. Bottura, CERN, Geneva, Switzerland

Abstract

This paper gives a broad summary of the physical phenomena associated with the quench of a superconducting magnet.

INTRODUCTION

Quench ([1], [2], [3], [4]) is the result of a resistive transition in a superconducting magnet, leading to the appearance of voltage, a temperature increase, differential thermal expansion and electro-magnetic forces, cryogen pressure increase and expulsion. In this process the magnetic energy stored in the magnet, and the power provided by the power supply, are converted into heat in a percentage that can go from a small fraction to its totality. Superconducting magnets, operating at large magnetic fields, store large energies, and the damage potential by excess temperature is considerable. In addition, the operating current density of superconducting magnets is high (few hundreds of A/mm^2), the rate of joule power is large, and the rate of temperature increase is fast, so that quick action is necessary to prevent a quench from damaging the magnet. A quench must be detected rapidly, and will invariably lead to a shutdown of the power supply, and the discharge of the magnet, either by dissipation of the magnetic energy onto its own thermal mass, or externally, on a dump resistor.

The occurrence of quench, and the strategy to protect the magnet from degradation and damage, must be carefully included in the design process. A number of issues must be considered when looking into the consequences of a quench, and implementing the necessary mitigation:

- Temperature increase at the so-called hot-spot, which can degrade or permanently damage materials, and temperature gradients that induce thermal stresses and can induce structural failure;
- Voltages within the magnet, and from the magnet to ground, including the whole circuit, that could lead to excessive electrical stress and, in the worst case, to arcing;
- Forces caused by thermal and electromagnetic loads during the magnet discharge transient, where the electromagnetic load conditions may deviate from the envelope of normal operating conditions, especially in case of inductively coupled systems;
- Cryogen pressure increase caused by heating that can induce large mechanical loads on the cryogen containment, and thermally induced expulsion, to be accommodated by proper sizing of venting lines and valves.

In the next sections we will review the governing physics during the quench initiation and propagation, and apply simplifications to derive some useful scaling that relate magnet design parameters to quench indicators.

PHYSICS OF QUENCH

The initiation and propagation of quench is governed by classical balance and circuital equations that can be written most conveniently in the form of a coupled system of partial and ordinary differential equations. Although the situation in accelerator magnets is three dimensional, we report below a version of these equations written in one dimension, along the length of the conductor. This is a most natural way to visualize the propagation of a quench, and although incomplete in terms of length and time scales, already provides a very good basis to establish simplified scaling laws. Note also that the length scales along the conductor (hundreds of m) and in the coil cross section (mm) are largely different, and a split of these scales when modeling quench, using 1-D for the direction of the developed conductor length, is quite natural.

Equations

The temperature of the conductor T_{co} is obtained from a heat diffusion equation:

$$A\bar{C}\frac{\partial T_{co}}{\partial t}-\frac{\partial}{\partial x}\left(A\bar{k}\frac{\partial T_{co}}{\partial x}\right)=A\dot{q}'''_{Joule}+p_w h\left(T_{he}-T_{co}\right) \qquad (1)$$

where we introduced averaged heat capacity, and thermal conductivity of the composite conductor, based on the area fraction f_i of the component i in the cross section, or:

$$\bar{C}=\sum_i f_i\rho_i c_i$$
$$\bar{k}=\sum_i f_i k_i$$

The joule heat term rises from zero when the temperature is under the current sharing temperature T_{cs}, to the value corresponding to the current fully in the stabilizer, above the critical temperature T_c:

$$\dot{q}'''_{Joule}=\bar{\eta}J^2$$

where J is the cable current density and we have used an average electrical resistivity, defined as

$$\frac{1}{\bar{\eta}}=\sum_i\frac{f_i}{\eta_i}$$

In practice, the only component of low electrical conductivity in a cable is often the stabilizer, and the above definition can be simplified as follows:

$$\bar{\eta} \approx \frac{\eta_{stab}}{f_{stab}}$$

where f_{stab} is the fraction of stabilizer (e.g. copper) and η_{stab} its resistivity. The last term of Eq. (1) models the cooling, in case of the presence of a helium flow or bath at temperature T_{he}, through a heat coefficient h at a wetted perimeter p_w.

For pool-boiling helium cooling, the time scale of the magnet quench is such that the temperature of the bath does not change significantly. Only at later time, as the energy is transferred to the helium, the bath can increase in temperature and pressure. In case of a forced-flow cooled cable, the behavior of the coolant during a quench can be modeled using the following simplified set of mass, momentum and energy conservation equations for the helium density ρ_{he}, velocity v_{he} and temperature T_{he}:

$$\begin{gathered}\frac{\partial \rho_{he}}{\partial t} + \frac{\partial v_{he}\rho_{he}}{\partial x} = 0 \\ \frac{\partial p_{he}}{\partial x} = -2\frac{f_{he}}{D_{he}}\rho_{he}\left|v_{he}\right|v_{he} \\ \rho_{he}c_{he}\frac{\partial T_{he}}{\partial t} + \rho_{he}v_{he}c_{he}\frac{\partial T_{he}}{\partial x} = 2\frac{f_{he}}{D_{he}}\rho_{he}\left|v_{he}\right|v_{he}^2 + \frac{p_w h}{A_{he}}\left(T_{co} - T_{he}\right)\end{gathered} \tag{2}$$

where p_{he} is the pressure, and f_{he} is the friction factor of the flow. Note that the above relation holds when friction dominates the momentum balance, which is usually the case in coils cooled by long pipes. Depending on the heating rate, heat transfer and flow characteristics, heating induced flow can be significant and participate to the quench propagation.

The final element is an equation for the whole electrical circuit, which consists in principle of a set of coupled coils, powered by a number of power supplies, and developing internal resistances that depend on the quench evolution. The currents in the coils **I** are most conveniently modeled solving a system of ordinary differential equations:

$$\mathbf{L}\frac{d\mathbf{I}}{dt} + \mathbf{RI} = \mathbf{V} \tag{3}$$

where **L** and **R** are the matrices of inductance and resistance of the circuit, and **V** are the voltage sources provided by, e.g., the power supplies in the circuit. Capacitive effects are neglected in Eq. (3). Although the circuit capacitance can affect voltage differences, its contribution to the current waveforms is generally negligible. Note that the resistance the circuits contain non-linear resistances (the quench resistance), non-linear voltage sources (e.g. diodes), and switching actions can change the circuit topology.

The set of Eqs. (1)-(3) is strongly coupled, and in particular:

- The heat generated by Joule heat in can transfer to the coolant as from Eq. (1), which expands and is expulsed from the normal zone, as from Eq. (2) ;
- The flow of warm coolant described by Eq. (2) next to a superconducting wire couples heat back into Eq. (1), and is a possible mechanism of quench propagation;
- The resistance of the quenched conductor from Eq. (1) enters the resistance matrix in the circuit equation Eq. (3) ;
- The current in the conductor from Eq. (3) enters in the evaluation of the Joule heat in Eq. (1).

The above equations contain material properties that, as well known, are highly dependent on temperature at cryogenic conditions. In practice, an analytic treatment of the complete set of coupled equations is impossible, and one has to resort to approximations. In the following sections we will discuss such approximations.

HOT SPOT

The main concern in case of quench is to limit the maximum temperature in the magnet. The peak temperature location, the so called hot-spot, is invariably at the location of the initial transition to the normal zone, where the Joule heating is acting for the longest time*. A conservative estimate of the hot-spot is obtained using the heat balance Eq. (1), by assuming adiabatic conditions, resulting in the following equation:

$$\bar{C}\frac{dT_{co}}{dt} = \bar{\eta}J^2$$

that can be integrated [1, 2, 4]:

$$\int_{T_{op}}^{T_{\max}} \frac{\bar{C}}{\bar{\eta}}dT = \int_0^{\infty} J_{op}^2 dt \tag{4}$$

Equation (4), which is the analogous of the design method for electrical fuses, was originally proposed for superconducting cables by Maddock and James [5]. It has the advantage that the left-hand side (lhs) is a property of the materials in the cable, while the right-hand side (rhs) is only dependent on the response of the circuit.

The integral on the lhs of Eq. (4) defines a function, $\Gamma(T_{max})$

* We make here the assumption that in no other part of the inductively coupled coil system the joule heating rate exceeds the one in the portion examined. This is not necessarily the case, especially for coupled solenoids as used in MRI and NMR systems.

$$\Gamma(T_{\max}) = \int_{T_{op}}^{T_{\max}} \frac{\bar{C}(\theta)}{\bar{\eta}(\theta)} d\theta \approx f_{stab} \int_{T_{op}}^{T_{\max}} \frac{\bar{C}(\theta)}{\eta_{stab}(\theta)} d\theta$$

that can be evaluated for the various materials used in a superconducting cable, and the approximation is valid when the composite resistivity is dominated by the stabilizer. One such evaluation example is shown in Fig. 1 for pure copper of different RRR, at zero magnetic field. The function $\Gamma(T_{max})$ can be approximated in the temperature range of interest (100 K to 300 K) by a simple power-law expression [1]:

$$\Gamma(T_{\max}) \approx f_{stab}\Gamma_0 \left(\frac{T_{\max}}{T_\Gamma}\right)^{1/2} \qquad (5)$$

where the two constants Γ_0 and T_Γ are fit parameters.

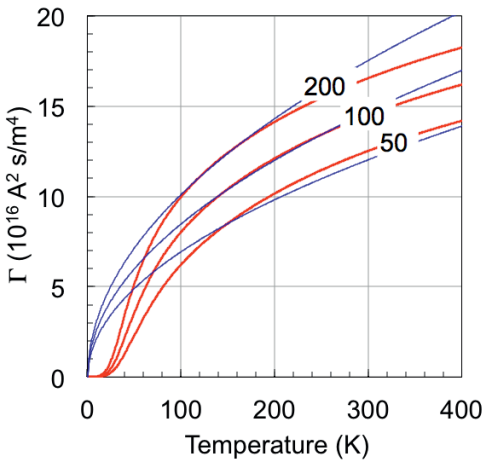

Figure 1: Sample evaluation of the function $\Gamma(T_{max})$ for copper in zero field, and taking RRR as a parameter. Also shown the power-law approximation defined in the text.

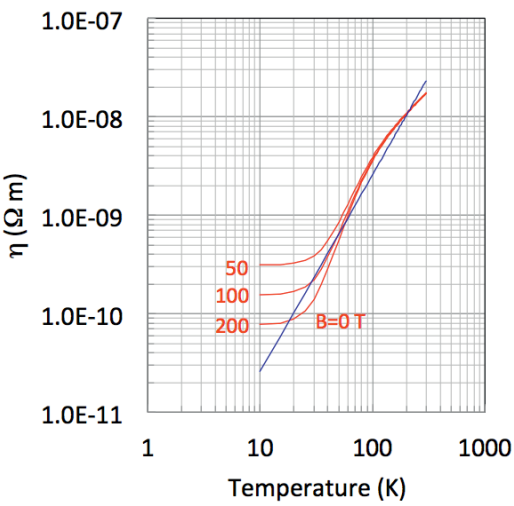

Figure 2: Resistivity $\eta(T)$ for copper in zero field, and taking RRR as a parameter. Also shown the power-law approximation defined in the text.

As we will discuss later, for the evaluation of the coil resistance during quench we also need a simple analytical expression for the stabilizer resistivity η_{stab}. This is known to be highly dependent on temperature and field. Sample data for copper are reported in Fig. 2. As also demonstrated in Fig. 2, a suitable approximation in the temperature range of interest is obtained fitting material data with the power-law:

$$\eta_{stab}(T) \approx \eta_0 \left(\frac{T}{T_\eta}\right)^n \qquad (6)$$

where η_o and T_η are the fitting constants.

The analytical approximation Eq. (5) is much simpler to handle than the general integral, but this is not yet sufficient to allow complete analytical treatment of the adiabatic balance Eq. (4). Indeed, the rhs integral in Eq. (4) depends on the current waveform, which in the general case contains an implicit dependence on the resistivity and the size of the normal zone, i.e. the quench resistance R_{quench}, and on the external resistance where the magnetic energy is dumped, at least in part, i.e. the dump resistance R_{dump}. Suitable bounds for the current waveform can be obtained by considering two extreme cases, namely the case when the magnet is dumped on an external resistance, which is much larger than the quench resistance (*external dump*), and the case in which the whole magnet is quenched at once (e.g. by heaters) and the external resistance is negligible (*internal dump*).

External dump

In this case a dump resistance $R_{dump} >> R_{quench}$ is put in series with the magnet of inductance L, and the current waveform is a simple exponential. The integral at the lhs of Eq. (4) yields:

$$\int_0^\infty J^2 dt = J_{op}^2 \left(\tau_{detection} + \frac{\tau_{dump}}{2}\right)$$

where J_{op} is the initial cable current density, $\tau_{detection}$ is the time spent at constant current to detect the quench and trigger the system dump (including switching actions), and the time constant of the exponential dump is

$$\tau_{dump} = \frac{L}{R_{dump}} = \frac{2E_m}{V_{\max} I_{op}}$$

which can be written as indicated using the magnetic energy E_m, the operating current I_{op} and the peak discharge voltage V_{max}.

We can use the above approximations in the adiabatic heat balance Eq. (4) to obtain a relation for the maximum temperature:

$$T_{\max} = \frac{T_\Gamma}{f_{stab}^2 \Gamma_0^2} J_{op}^4 \left(\tau_{detection} + \frac{E_m}{V_{\max} I_{op}}\right)^2 \qquad (7).$$

The relation above is very useful in indicating functional dependencies of the hot-spot temperature on design and operation parameters. In the case of an external dump of a magnet with given magnetic energy E_m (determined by the geometrical configuration) and operating at given current density J_{op} (as high as practical for winding efficiency and cost reasons) the hot-spot temperature can be reduced by:

- using materials with a large Γ (i.e. large heat capacity, small resistivity), and large stabilizer fraction f_{stab};
- detecting rapidly (small $\tau_{detection}$);
- discharging under the largest possible terminal voltage V_{max};
- choosing cable designs with large operating current I_{op} (decrease the magnet inductance).

Equation (7) can be studied parametrically, as shown in Fig. 3. The family of curves plotted there represent the relation between the operating current density and the maximum magnetic energy in the magnet system, resulting in a hot-spot temperature of 300 K, and taking the detection time as a parameter. The model cable parameters considered are of a Cu/Nb_3Sn composite with a Cu:non-Cu ratio of 1.2, operating current of 10 kA, and a discharge voltage of 1 kV. The fit parameters for the approximation of $\Gamma(T_{max})$ are $\Gamma_0 = 45\times10^3$ A^2 s/mm^4 and $T_\Gamma = 100$ K.

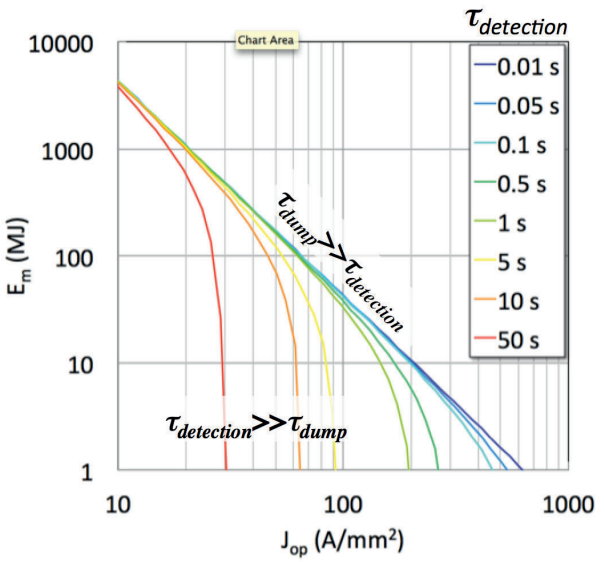

Figure 3: Case study of external dump. Relation between operating current density and maximum magnetic energy yielding a hot-spot temperature of 300 K in a Cu/Nb_3Sn strand with Cu:non-Cu ratio of 1.2, 10 kA operating current and 10 kV discharge voltage.

We recognize in the plot two regimes. If the detection is fast, and the energy is dissipated mostly during the dump time, the allowable magnetic energy of the system decreases like the inverse of the square of the operating current density. This is the upper envelope in the family of curves, marked in Fig. 3 as $\tau_{dump} >> \tau_{detection}$. This limit, in practice, gives the highest possible size of a magnetic system designed for a given operating current density, assuming protection based on external dump and complete energy extraction. To fix orders of magnitude, with the parameters chosen it is not possible to limit the hot-spot temperature below 300 K in a magnet with stored energy in the range of 10 MJ and an operating current density above 200 A/mm^2 if the maximum discharge voltage is 1 kV. Once the hot-spot limit, the magnetic energy, and the operating current density are given, the only means to extend this limit is by increasing the operating current I_{op} or the terminal voltage V_{max}.

The second regime is found when the dump happens rapidly with respect to the time required for detection and switching, so that most magnetic energy is dissipated by Joule heat during the latter time. This regime is the region identified in Fig. 3 as $\tau_{detection} >> \tau_{dump}$. In this regime the hot-spot reaches the maximum allowed at the end of the detection time, under the Joule heating at constant current. This happens more or less rapidly depending on the operating current density, irrespective of the magnetic energy in the system. The limit becomes hence a simple relation between $\tau_{detection}$ and J_{op}, and lines in the plot become vertical. Once again, to fix orders of magnitude, the maximum allowable detection time to limit the hot-spot temperature below 300 K, at an operating current density of 200 A/mm^2, is of the order of 1 s, irrespective of operating current, terminal voltage, and magnet stored energy.

Internal dump

In the case of an internal dump, the dump resistance is negligible, and the energy is completely dissipated in the magnet system. Still, without the knowledge of the evolution of the quench resistance $R_{quench}(t)$ it is not possible to compute the current in the system, and evaluate the integral at the lhs of Eq. (4). Indeed, the general case requires the knowledge of the initiation and propagation of the normal zone, which is quite complex. To further simplify, and obtain analytical estimates, we make the assumption that the magnet is quenched completely once a normal zone is detected. This is a situation of relevance for accelerator magnets, where heaters are fired to spread the normal zone, and to hasten the dump. Following Wilson, we finally make the hypothesis that the current waveform can be approximated by a step function, with the current remaining constant for a time τ_{quench} necessary to dissipate the whole stored magnetic energy, and dropping to zero instantaneously after this time [1]. In this case the adiabatic balance Eq. (4) simplifies, as the integral of the current density becomes trivial, and using Eq. (5) we obtain the following approximation for the temperature evolution of the magnet bulk:

$$T \approx \frac{T_\Gamma}{f_{stab}^2 \Gamma_0^2} J_{op}^4 t^2 \qquad (8)$$

which holds until the time τ_{quench}. To evaluate τ_{quench}, we equate the joule heat dissipated in the magnet to the magnetic energy, or:

$$V_m J_{op}^2 \int_0^{\tau_{quench}} \bar{\eta}(t)\,dt = E_m$$

where V_m is the volume of conductor in the magnetic system, and we remark that the only integral required is that of the conductor resistivity. At this point we make use of the power-law approximation for the resistivity, Eq. (6), and the temperature waveform given by Eq. (8) to obtain the following approximate expression for the quench time:

$$\tau_{quench} = (2n+1)^{\frac{1}{2n+1}} \left(\frac{e_m}{\alpha}\right)^{\frac{1}{2n+1}} \frac{f_{stab}}{J_{op}^2} \qquad (9)$$

where we introduced the stored energy per unit coil volume $e_m = E_m/V_m$, and the parameter α is a constant that depends on the cable materials and design, given by:

$$\alpha \approx \eta_0 \left(\frac{T_\Gamma}{T_\eta \Gamma_0^2}\right)^n$$

At this point, knowing the time τ_{quench}, and using Eq. (8) we arrive at the estimate of the maximum temperature in the magnet bulk:

$$T_{bulk} \approx (2n+1)^{\frac{2}{2n+1}} \frac{T_\Gamma}{\Gamma_0^2} \left(\frac{e_m}{\alpha}\right)^{\frac{2}{2n+1}} \qquad (10)$$

It is interesting to note that the bulk temperature of the magnet only depends on the magnetic energy per unit volume, and material properties. The hot-spot temperature will be higher than the magnet bulk temperature given by Eq. (10) because of the time required to detect the normal zone and quench the magnet. Note that in this case the *detection* time is intended to include the heater firing and heater delay times, until the magnet is actually in normal state. Using again Eq. (8), and substituting for α, the hot-spot temperature will be:

$$T_{\max} = \frac{T_\Gamma}{f_{stab}^2 \Gamma_0^2} J_{op}^4 \left(\tau_{\det ection} + (2n+1)^{\frac{1}{2n+1}} \left(\frac{e_m}{\alpha}\right)^{\frac{1}{2n+1}} \frac{f_{stab}}{J_{op}^2}\right)^2 \qquad (11)$$

We note in Eq. (11) two components for the hot-spot temperature, i.e. the temperature increase at constant current, which depends on the operating current density and the detection time, and the temperature increase generated by the dump of the magnetic energy in the magnet, which only depends on the cable properties and the magnetic energy per unit volume of coil (see the analogy with Eq. (10)). This second component does not depend on the cable dimensions, nor its operating current density, as one would expect from first principles.

Similarly to what done for the case of external dump, we can study the functional dependence of Eq. (11) by choosing typical magnet parameters of interest. We take the same model cable parameters, i.e. a Cu/Nb_3Sn composite with a Cu:non-Cu ratio of 1.2. The fit parameters for the approximation of $\Gamma(T_{max})$ are the same as before, while for the approximation of $\eta_{stab}(T)$ we take η_0 = 4.1×10^{-9} Ωm and T_η = 125.6 K. Assuming once again a hot spot temperature of 300 K, we can plot a family of curves giving the maximum stored energy per unit coil volume as a function of the operating current density, in Fig. 4.

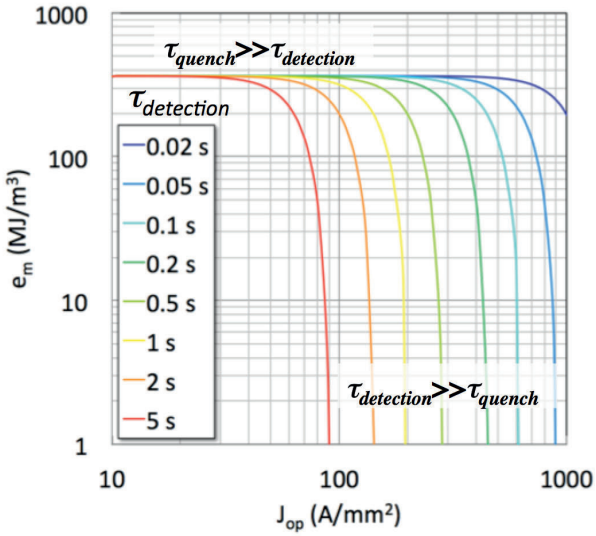

Figure 4: Case study of internal dump. Relation between operating current density and maximum magnetic energy per unit volume yielding a hot-spot temperature of 300 K in a Cu/Nb_3Sn strand with Cu:non-Cu ratio of 1.2.

As in the previous analysis, we can distinguish two regimes, depending on whether the magnet quench time is significantly longer or shorter than the detection time. In the first case, fast detection, identified by the asymptote marked in Fig. 4 as $\tau_{quench} >> \tau_{detection}$, the contribution of Joule heating to the hot-spot temperature is negligible, and the limit is a horizontal line given by the energy per unit coil mass, as discussed above, independent of the cable current density. Note how the typical cable parameters chosen indicate that an energy density of 350 MJ/m^3 seems to be an absolute upper limit for protection, irrespective of operating current density and detection time.

The other limit is obtained when the quench time is fast with respect to the detection and heating time. This is typically the case at high current density, when resistance grows fast and the magnetic energy is dumped rapidly. In this regime, the Joule heating before detection dominates the hot-spot temperature, irrespective of the energy stored in the magnet, and the lines of constant hot-spot

temperature become vertical. Note that this limit is asymptotically identical for an internal and external dump, i.e. Figs. 3 and 4 are coincident in the low energy range. As to the order of magnitude, we remark that with the cable parameters chosen, and assuming an operating current density of 400…500 A/mm^2, it is mandatory to detect and quench a magnet even with little stored energy per unit volume within 200 ms to limit the hot-spot to less than 300 K.

QUENCH PROPAGATION AND DETECTION

The discussion on the hot-spot temperature scaling has shown how important it is to detect a quench rapidly, so that the heat capacity reserve can be exploited to absorb the magnetic energy stored in the system, rather than being wasted taking the external power provided from the power supply. A rapid quench trigger depends on the method used to detect a normal zone, and on the threshold setting necessary to discriminate among spurious events and a real quench. Nowadays, voltage measurements are the simplest and most direct means to detect a normal zone. It is therefore of interest to estimate the time required to see a given voltage, which gives a lower bound for the detection time defined earlier.

The resistive voltage in the initial phase of a quench grows in time because the temperature of the initial normal zone increases (which causes an increase of the resistivity per unit length), and because the quench propagates in the magnet. Making the assumption that the initial normal zone is small, as would be the case for a quench triggered by a perturbation at the scale of the Minimum Propagating Zone (MPZ) [6], we see that to estimate the detection time we need to know the quench propagation velocity.

Quench propagation has been the topic of many analytical and experimental studies. A sample of early theoretical work can be found in [7-12] and the review of Turck [13], as well as the extensive reference list of [14]. Interesting later works are the theory for super-stabilized cables [15], and the mapping of propagation regimes in force-flow cooled CICC's from [16-19]. Indeed, the quench propagation velocity depends on the conductor geometry, properties, and most important on the cooling conditions. To give a sense for the differences among the different regimes, we report below typical estimates for the quench propagation velocities calculated in an adiabatic winding, a pool-boiling winding, and a force-flow cooled winding.

The expression for the quench propagation velocity in an adiabatic conductor $v_{adiabatic}$ is the following classical solution of the conduction equation developed as early as 1960 [7] and quoted by Wilson [1]:

$$v_{adiabatic} = \frac{J_{op}}{\bar{C}} \sqrt{\frac{\bar{\eta}\bar{k}}{\left(T_{Joule} - T_{op}\right)}} = \beta J_{op} \qquad (12)$$

where we used the earlier definitions for the conductor properties, and we have introduced a transition temperature T_{Joule} that is generally taken between the current sharing temperature T_{cs} and the critical temperature T_c to account for the gradual onset of Joule heating (Wilson takes the average of the two). The above expression, which is valid only for constant material properties, has been much modified by several authors to take into account variable properties. Note, however, the interesting feature that the propagation velocity is proportional to the operating current density [20].

In the case of cooling at the conductor surface, as is the case in a pool-boiling magnet, the propagation velocity v_{cooled} can be obtained correcting the above expression as follows, as detailed once again by Wilson [1]:

$$v_{cooled} = \frac{1-2y}{\sqrt{1-y}} v_{adiabatic} \qquad (13)$$

where the correction factor is given by:

$$y = \frac{p_w h\left(T_{Joule} - T_{op}\right)}{A\bar{\eta}J_{op}^2} \propto \frac{1}{\alpha_{Stekly}} \qquad (14)$$

which shows explicitly the proportionality relation to the Stekly "alpha" parameter α_{Stekly} [21], thus recalling the fact that a quench never propagates in a cryostable conductors ($\alpha_{Stekly} < 1$).

To represent the case of a force-flow cooled conductor, we resort to the theory of quench propagation in Cable-in-Conduit Conductors (CICC's) of Shajii and Freidberg, who mapped all possible cases in a universal scaling plot [18-19]. The case of most relevance, obtained for a short initial normal zone, is that of a small pressure rise, in which case is the quench velocity v_{CICC} is obtained using the following expression [18]:

$$v_{CICC} = \frac{R\rho_0 L_{INZ}}{2p_0} \frac{\bar{\eta}J_{op}^2}{\bar{C}} \qquad (15)$$

where ρ_0 and p_0 are the initial density pressure of helium, R is the gas constant in the perfect gas state equation, and L_{INZ} is the length of the initial normal zone.

The expressions above have very different structure, which depends on the physical mechanism mediating the quench propagation, but they all show that at constant properties and current the quench velocity is constant in time. Any deviation from a constant velocity implies a change in properties (e.g. a quench propagating into a zone of higher or lower field), or the on-set of an additional mechanism of propagation, a quench-back.

One such mechanism is transverse propagation, i.e. a quench jump from one turn to the next, or from one layer to the neighboring one, across the coil, rather than along the conductor. Estimates for the transverse propagation velocity are complex. On one hand, the characteristic longitudinal length is typically three orders of magnitude

larger than the transversal one. On the other hand, this is compensated by a similar difference in thermal diffusivity in the two directions. Orders of magnitude estimates can be obtained by dimensional analysis, resulting in the case of an adiabatic winding in the following relation [1,22]:

$$\frac{v_{transverse}}{v_{longitudinal}} \approx \sqrt{\frac{\bar{k}_{transverse}}{\bar{k}_{longitudinal}}} = \kappa \qquad (16)$$

where averages are intended over the typical unit winding cell, and we have introduced a propagation anisotropy factor κ. The reader is advised that Eq. (16) only gives a scaling, and may require large correction factors to reflect reality [22].

Given the above elements, and assuming a small initial normal zone propagating in a winding pack of sufficiently large dimension, we can estimate the voltage V_{NZ} generated at constant current from a volume integral of the resistivity in the normal zone, a method devised and used extensively in [1] as well as many analytic or semi-analytic quench codes. The result of the evaluation yields the following scaling relation:

$$V_{NZ} \approx \frac{8\pi}{(2n+1)(2n+2)(2n+3)} \alpha\kappa^2 \frac{J_{op}^{4n+1} v_q^3}{A} t^{2n+3}$$

where the parameters are defined earlier. With the value of n=2, we obtain:

$$V_{NZ} \approx \frac{4\pi}{105} \alpha\kappa^2 \frac{J_{op}^9 v_q^3}{A} t^7 \qquad (17).$$

We can make use of Eq. (17), and one of the above expressions for the quench propagation velocity to study the dependence of the detection time for a given detection threshold. We show the results of the exercise in Fig. 5, where we have taken the same conductor parameters already used earlier, we have considered an adiabatic winding (i.e. quench velocity given by Eq. (12)) and a propagation anisotropy of κ=10^{-3}. We have reported there the detection time as a function of the operating current density in the conductor and computed using the detection threshold as a parameter in the range of 10 mV to 2 V. For reference, we have also added the evaluation of the quench velocity.

The detection time scales inversely to a power, around 2, of the current density. This is due to the combined effect of the resistivity growth with temperature and to the propagation velocity, both increasing functions of the current density. This supports the common wisdom that a quench in a high current density conductor is "easier" to detect than at low current density. At an operating current density of relevance, around J_{op}=400 A/mm^2, typical values of quench velocity v_q=20 m/s are obtained from Eq. (12), which is the order of magnitude observed in magnet tests. At this J_{op} the resulting detection time is in the range of one to few ms, depending on the voltage threshold. This is relatively short, also because detection filters and delays are not included in this simple analysis. Indeed, as we anticipated, the scaling study does not attempt to provide exact values, but rather proper functional dependencies.

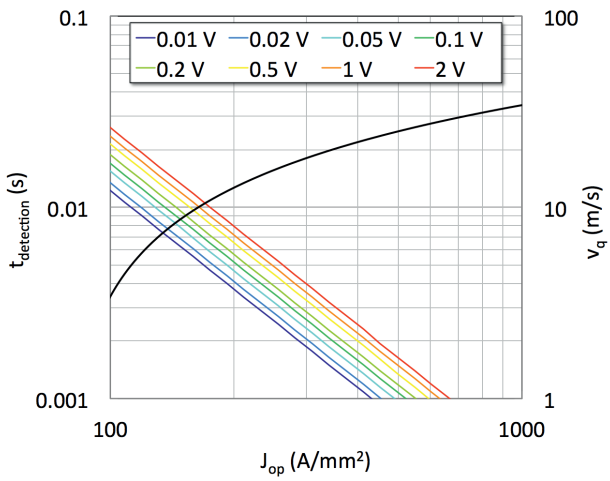

Figure 5: Relation between operating current density and detection time per unit volume yielding a hot-spot temperature of 300 K in a Cu/Nb_3Sn strand with Cu:non-Cu ratio of 1.2.

An interesting feature of Fig. 5 is that a variation of the detection threshold of two orders of magnitude (e.g. from 10 mV to 1 V) only results in an increase of the detection time by a factor 2 (e.g. from slightly above 1 ms to slightly above 2 ms at 400 A/mm^2). The reason is that once the quench is developed, the rate of temperature and voltage increase is fast (see the high power of the time function in Eq. (16)), and the difference in time among different voltage criteria is hence small. It would be interesting to test this somewhat surprising result of the scaling in a controlled experiment.

QUENCH VOLTAGES

The resistive voltage generated in the normal zone, and the inductive voltage associated with the current variations, can be the source of a significant electrical stress in the magnetic system. An electrical failure is naturally of much concern, especially in systems of large stored energy, which is why it is important to have a good evaluation of the maximum voltage associated with a quench, both internal to the magnet (turn-to-turn and layer-to-layer) and to ground. We need to distinguish here between the two cases discussed earlier, namely the external dump and the internal dump.

In case of an external dump, the quench resistance is small with respect to the external dump resistance. The voltage seen by the coil will be maximum at the terminals and the beginning of the discharge:

$$V_{\max} = R_{dump} I_{op} .$$

The internal voltages in this case distribute in the coil according to the inductance of each portion, and can be easily deduced from the terminal voltage. Similarly, the maximum ground voltage can be obtained from the terminal voltage, once the grounding scheme of the circuit is known.

The case of an internal dump is much more complex. In this case the terminal voltage is approximately zero, as the dump resistance is much smaller than the quench resistance. The internal voltage, however, is not. The local potential results from a distributed component, the inductive voltage associated to the current variation, and a localized component, the resistive voltage in the normal zone. Unless the normal zone extends over the whole magnet (true only at late stages in the quench), and the inductance and resistance per unit length are constant in the magnet (never true), the local value of the potential can rise to relatively large values, still maintaining a value close to zero at the terminals. In this case the analysis of the voltage requires the knowledge of the extent and temperature of the normal zone. Following again Wilson, it is possible to obtain estimates by writing first the circuit equations of the whole magnet [1,3]:

$$L\frac{dI}{dt}+R_{quench}I=0$$

which is obtained from Eq. (3), assuming a single circuit, and postulating zero voltage at the terminals. This equation is complemented by an equation for the quench voltage in the normal zone:

$$V_{quench}=R_{quench}I-M_{NZ}\frac{dI}{dt}$$

where we indicate with M_{NZ} the mutual inductance between the whole magnet and the normal zone itself. M_{NZ} is a function of time, according to the normal zone propagation and the geometry of the magnet, and varies from a small value, when the normal zone forms, to the magnet inductance L, when the normal zone extends over the whole length.

Combining the two relations above, Wilson obtains an equation for the quench voltage:

$$V_{quench}(t)=I(t)R_{quench}(t)\left(1-\frac{M_{NZ}(t)}{L}\right) \qquad (18).$$

Without entering into the complex details of an evaluation of Eq. (18), we remark that during a quench the current $I(t)$ decreases, as well as the inductance term $(1-M_{NZ}(t)/L)$, while the resistance $R_{quench}(t)$ increases. This results in a maximum of the quench voltage during the transient, whose accurate evaluation generally requires a numerical simulation

HELIUM PRESSURE AND EXPULSION

Under the large heating of a quench, and in case the winding is cooled directly by a bath or a flow of helium, the coolant undergoes a pressure increase which is caused either by the vaporization of the liquid, or the large decrease of density of supercritical helium as temperature increases. Considering here large-scale applications, where the amount of heating per unit coolant volume is considerable, the pressure increase can be very large, and provisions are taken to vent helium to buffers or, eventually, the atmosphere. The design and analysis of the cryogenic aspects of a quench are fairly complex matters, and are best dealt with semi-analytical or numerical simulation codes that take into account the transient energy deposition into the helium, and the process of expulsion.

It is however useful to fix order of magnitudes to give a feeling for the severity of a quench from the point of view of the cryogenic system. To do this, we give estimates for the pressure increase in a bath-cooled magnet, and an expression for the pressure increase in a quenching force-flow cooled conductor.

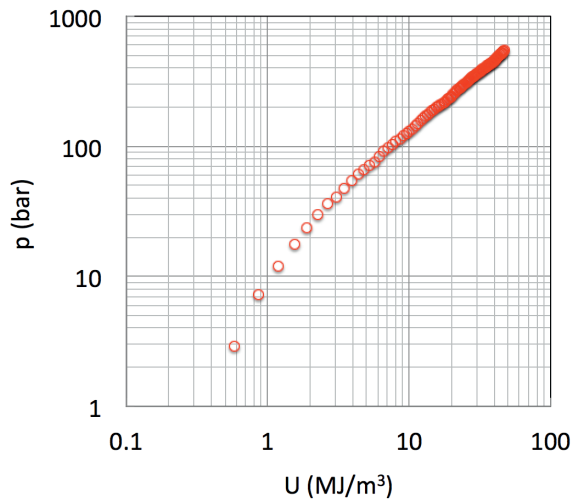

Figure 6: Relation between pressure p and internal energy density variation U at constant helium density, from an initial operating point at 1.9 K and 1 bar (case of the LHC dipole).

In the first case, we take the simple case of a bath at constant volume, which is a good approximation of the real case before the openings of quench valves. The pressure can be simply evaluated from helium thermodynamic properties, knowing the initial state, and the energy deposition in the bath. If we take the example of the LHC dipoles, with an initial state at 1.9 K and 1 bar, Fig. 6 gives the helium pressure as a function of the energy per unit volume. In the case of the LHC dipoles, the helium volume is of the order of 0.3 m^3, and the stored energy is 10 MJ per dipole. If all the energy were deposited in the helium bath, the pressure under constant volume condition would reach values in the range of 400 bar. Even if a small fraction of the dipole energy, less than 10 %, would be deposited in the helium, this would lead to a pressure increase above the limit of 20 bar for the

cold mass, which is why a system of quench relief valves opens in case of quench, and allows helium discharge into the large buffer provided by the cryogenic lines.

In force-flow cooled magnets, the helium cannot escape freely from the quenched portion: the pressure rises and drives a heating-induced flow, which is limited by friction. Dresner developed a theory for the pressure increase in a helium pipe, and showed that the peak pressure increase p_{max} in the rather conservative case of heating over the full length of the pipe is [23]:

$$p_{\max} \approx 0.65\left[\frac{f}{D_h}\left(\frac{L}{2}\right)^3\left(\frac{\overline{\eta}J_{op}^2}{f_{he}}\right)^2\right]^{0.36} \qquad (19)$$

where f and D_h are the friction factor and the hydraulic diameter of the flow, L is the length of the cooling channel, and f_{he} is the fraction of helium in the conductor.

Lue, Miller and Dresner [23] validated the above relation against experiments, see Fig. 7, and demonstrated that the pressure increase in a long pipe can reach very high values (hundreds of bar) under heating rates per unit volume that are applicable to the situation of a quench in a force-flow cooled conductor such as a CICC. In this case the conduit must be designed to withstand the quench expulsion pressure, or the conductor length reduced.

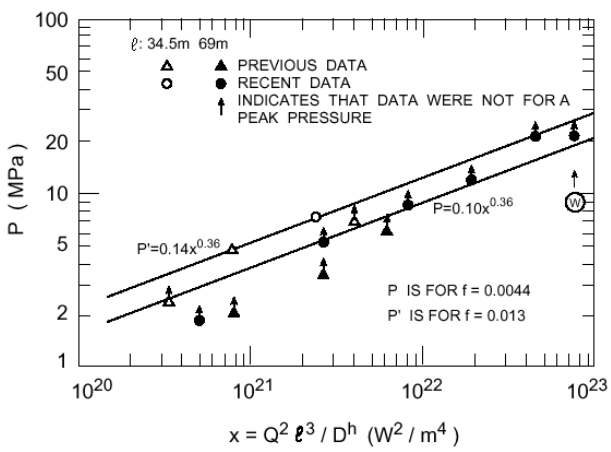

Figure 7: Experimental data on peak pressure in a heated conduit of helium, showing the results of the scaling relation Eq. (18) (from [23]).

REFERENCES

[1] M.N. Wilson, Superconducting Magnets, Plenum Press, 1983.

[2] Y. Iwasa, Case Studies in Superconducting Magnets, Plenum Press, 1994

[3] B. Seeber ed., Handbook of Applied Superconductivity, IoP, 1998.

[4] P.J. Lee ed., Engineering Superconductivity, J. Wiley & Sons, 2001.

[5] B.J. Maddock, G.B. James, "Protection and Stabilization of Large Superconducting Coils," Proc. IEE, 115 (4), 543, 1968.

[6] S.L. Wipf, Stability and Degradation of Superconducting Current-Carrying Devices, Los Alamos Scientific Laboratory Report, LA7275, 1978.

[7] W.H. Cherry, J.L. Gittleman, Thermal and Electrodynamic Aspects of the Superconductive Transition Process, Solid State Electronics, 1(4), 287, 1960.

[8] V.E. Keilin, E.Yu. Klimenko, M.S. Kremlev. N.B. Samoilev , Les Champs Magnetiques Intenses, Paris, CNRS, 231, 1967.

[9] L. Dresner, Propagation of normal zones in composite superconductors, Cryogenics, 16, 675, 1976.

[10] L. Dresner, Analytic Solution for the Propagation Velocity in Superconducting Composites, IEEE Trans. Mag., 15(1), 328, 1979.

[11] K. Ishibashi, M. Wake, M. Kobayashi, A. Katase, Propagation velocity of normal zones in a SC braid, Cryogenics, 19, 467, 1979.

[12] Yu.M. Lvovsky, M.O. Lutset, Transient heat transfer model for normal zone propagation. Part 1 – Theory of a bare helium-cooled superconductor, Cryogenics, 22, 581, 1982.

[13] B. Turck, About the propagation velocity in superconducting composites, Cryogenics, 20, 146, 1980.

[14] A. Devred, General Formulas for the Adiabatic Propagation Velocity of the Normal Zone. IEEE Trans. Mag., 25(2), 1698, 1989.

[15] A. Devred, Quench propagation velocity for highly stabilized conductors. Cryogenics, 33, 449, 1993.

[16] L. Dresner, Proc. 10th Symp. Fus. Eng.ng, 2040, 1983.

[17] L. Dresner, Proc. 11th Symp. Fus. Eng.ng, 1218, 1985.

[18] A. Shajii, J. Freidberg, J. Appl. Phys., 76 (5), 477-482, 1994.

[19] A. Shajii, J. Freidberg, Int J. Heat Mass Transfer, 39(3), 491-501, 1996.

[20] J.R. Miller, J.W. Lue, L. Dresner, IEEE Trans. Mag., 13 (1), 24-27, 1977.

[21] Z. J. J. Stekly and J. L. Zar, Stable Superconducting Coils, March 1965, Research Report 210, Also IEEE Trans. Nucl. Sci. NS-12, 367 1965.

[22] C.H. Joshi, Y. Iwasa, Prediction of current decay and terminal voltages in adiabatic superconducting magnets, Cryogenics, 29, 157, 1989.

[23] J.R. Miller, L. Dresner, J.W. Lue, S.S. Shen, H.T. Yeh, Proc. ICEC-8, 321, 1980.

QUENCH LIMITS IN THE NEXT GENERATION OF MAGNETS

E. Todesco, CERN, Geneva, Switzerland

Abstract

Several projects around the planet aim at building a new generation of superconducting magnets for particle accelerators, relying on Nb_3Sn conductor, with peak fields in the range of 10-15 T. In this paper we give an overview of the main challenges for protecting this new generation of magnets. The cases of isolated short magnets, in which the energy can be extracted on an external dump resistor, and chain of long magnets, which have to absorb their stored energy and have to rely on quench heaters, are discussed. We show that this new generation of magnets can pose special challenges, related to both the large current density and to the energy densities.

INTRODUCTION

Protection of superconducting magnet is a fascinating subject that involves different branches of physics and engineering, as material properties at low temperatures, superconductivity, heat propagation and magnet design. For the new generation of accelerator magnets, aiming at the 10-15 T range provided by Nb_3Sn, protection becomes a critical aspect.

It is usually stated that higher fields mean larger stored energies and this entails more challenging protection. This statement is not completely correct, since for long magnets the physical limit for hotspot temperatures is on the energy density in the coil rather than on the magnet stored energy. Indeed, this density in many Nb_3Sn models is twice w.r.t. previous Nb-Ti accelerator magnets: there is no doubt that the new generation of magnets enters a new regime from the protection point of view: including protection from the start of the magnet design process is a must.

Here we will try to address the main issues in the interaction between magnet design and protection for accelerator superconducting magnets. We will give a special emphasis to the case of Nb_3Sn conductor, which is being considered for the LHC upgrades. Starting with a discussion of the hotspot temperature, we outline the protection strategies with and without external dump, providing the relation to the main design parameters as current and inductance.

We then introduce the concept of time margin for protection, i.e. the time available to the protection system to quench all magnet before it reaches the limit in the hotspot temperature. We estimate this parameter for several cases, and we give the dependence on the design features, pointing out the relevance of the current density. The time margin is consumed by different operations of the protection system: we discuss here the detection time, related to the initial quench velocity, and the time needed by the heaters to quench the entire coil, which are two essential features of the problem. We conclude with a discussion of the inductive voltages which arise by an unbalance between parts of the magnet that are quenched and parts that are still superconductive.

HOTSPOT TEMPERATURE

Recall of adiabatic approximation

The basis of our analysis is the adiabatic equation of balance between heat given by Joule effect and specific heats

$$\int_0^\infty [I(t)]^2 dt = \nu A^2 \int_{T_0}^{T_\infty} \frac{c_p^{ave}(T)}{\rho_{Cu}(T)} dT \qquad (1)$$

where I is the current in the magnet, A the cross sectional surface of the cable, ν the fraction of copper, c_p^{ave} the average volumetric specific heat, and ρ_{Cu} the copper resistivity. Together with the Joule heating equation, one has a set of coupled nonlinear equations giving the current decay in the magnet I(t), in the adiabatic approximation [1], and one can estimate the final temperature T_∞ in the coil. Note that since the resistivity depends on the magnetic field, the final temperature also depends on the position in the coil.

The right hand side of (1), integrated up the maximum acceptable temperature T_{max}, is our "quench capital", i.e. what nature gives us to spend in terms of specific heats and resistivity to absorb the energy of the magnet:

$$\Gamma(T_{max}) \equiv \nu A^2 \int_{T_0}^{T_{max}} \frac{c_p^{ave}(T)}{\rho_{Cu}(T)} dT = \nu A^2 \int_{T_o}^{T_{max}} \gamma(T) dT \; ; \qquad (2)$$

its physical units are square of current times seconds, usually expressed in MIITs. The quench capital Γ depends only on the composition of the cable and on the magnetic field. It <u>scales with the square of the cross-sectional surface of the cable A, and is proportional to the copper fraction ν</u>.

The left hand side of Eq. (1) is the "quench tax", i.e. what is consumed by the magnet

$$\Gamma_q \equiv \int_0^\infty [I_q(t)]^2 dt \qquad (3)$$

The quench tax depends on the features of the magnet as inductance, current, and on the circuit (energy extraction, etc). It <u>scales with the square of the current</u>.

What to include in the capital

In the adiabatic approximation one has to make a hypothesis about the elementary cell that takes the heat. The most conservative hypothesis is to take the strand, i.e. the mix of superconductor and stabilizer. One can also assume that the Joule heating is also shared by the insulation and the epoxy (for impregnated coils). If the coil is not impregnated and operates in superfluid Helium,

the contribution of HeII to the specific heat is very large below the transition temperature 2.17 K, so it plays a major role in the initial part of the heating. On the other hand, it becomes negligible w.r.t. the strands when the specific heat is integrated up to room temperature.

Elements which are more far from the original source of heating will take more time to contribute to the enthalpy. With typical time scales of the current discharge (0.1-0.5 s) the usual approximation takes into account of strand and insulation, but not wedges of the mechanical structure around the coil, see [2, 3] for more details.

In the following we will make the usual assumption of adiabatic codes, i.e., that the whole insulated coil shares the Joule heating, and the quantities in (1)-(3) will be referred to the insulated cable.

Limits to hotspot temperature

What is the maximum tolerable hotspot temperature guaranteeing no permanent degradation of magnet performances? A conservative limit can be established at 150 K [4, 5], and in most cases room temperature is considered to be safe. Some experiments on Nb_3Sn magnets showed no degradation up to 400 K [3], and even more. For Nb_3Sn magnets the temperature where the impregnation undergoes a phase transition can be considered a hard limit, see [3] for more details.

Since the quench capital Γ approximately scales with the square root of the temperature [1], from 300 to 400 K one gets about 15% more, i.e. not such a dramatic increase. In the following, we will consider 300 K as a limit, knowing that this is a conservative value.

PROTECTION STRATEGIES

External dump resistor

We first assume that the energy can be extracted to an external dump resistor R_d. The larger the dump resistance, the faster the decay:

$$I(t) = I_0 \exp\left(-\frac{t}{\tau}\right) \tag{4}$$

where, neglecting the magnet resistance, the time constant can be expressed as:

$$\tau = \frac{L}{R_d}, \tag{4}$$

The faster decay, the smaller is the quench tax Γ_q (see Eq. 3). The limit to having large resistors is given by the voltage on the magnet

$$R_d < \frac{V_{\max}}{I_o} \tag{5}$$

where the maximum voltage is of the order of 1 kV. Taking the maximum allowed limit, the quench tax Γ_q is given by

$$\Gamma_q = \int_0^\infty [I(t)]^2 dt = I_o^2 \int_0^\infty \exp\left(-\frac{2t}{\tau}\right) dt = \frac{L}{R_d}\frac{I_o^2}{2} = \frac{UI_o}{V_{\max}} \tag{6}$$

Where U is the magnet energy (we assume the linear case with constant inductance). So the condition of protection reads

$$\Gamma > \Gamma_q = \frac{UI_o}{V_{\max}}; \tag{7}$$

The first observation is that Γ is independent of the magnet length, whereas Γ_q is proportional to the length through the energy U. Therefore for longer and longer magnets the dump resistor strategy is less and less effective, due to the voltage limitation, i.e. the external dump resistor strategy is not independent of the magnet length. The second remark is that given an energy U, a magnet with larger cable (and less turns, i.e. lower inductance) has a more favourable energy extraction. In fact, the quench capital scales with the square of the area of the cable, whereas the quench tax scales with the current (see r.h.s. of Eq. 7), i.e. with the area of the cable. So in a case of external dump resistor, larger cable, higher currents and lower inductance ease protection, possibly allowing to satisfy the condition (7).

As an example, we show the case of the insertion quadrupole Q4 for the LHC upgrade. This magnet has to provide 550 T of integrated gradient, and is individually powered. Considering a two-layer coil with 8.8 mm width cable, one obtains 128 T/m operational gradient with 20% margin on the loadline. This option does not satisfy the quench protection requirement (7), i.e. the external dump resistor cannot provide a full protection (see Table 1). On the other hand, a one layer option with double width cable of 15 mm allows a protection with the dump resistor only as Γ becomes greater than Γ_q.

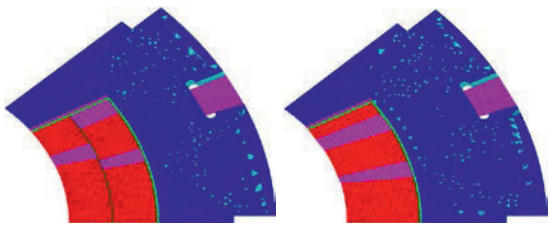

Figure 1: Cross-section of Q4 quadrupole for the LHC upgrade, one layer (left) and two layers (right) [6].

Table 1: Two options for the design of Q4 in LHC upgrade

		Two layers	One layer	Ratio
Integrated gradient	(T)	544	544	1.00
Gradient	(T/m)	128	120	1.07
Cable width	(mm)	8.8	15.1	0.58
Cable thickness	(mm)	1.00	1.74	0.57
Cable cross-section	(mm^2)	8.96	26.11	0.34
Length	(m)	4.25	4.53	0.94
Inductance	(H)	0.086	0.0069	12.46
Current	(A)	4865	16188	0.30
Dump resistor	(Ω)	0.164	0.049	3.33
Time constant	(s)	0.523	0.140	3.75
Γ	(MIITs)	3.2	30	0.11
Γ_q	(MIITs)	6.2	18.4	0.34

No external dump resistor

If the dump resistor extracts only a negligible fraction of the stored energy, the magnet itself has to take this energy. Since the quench propagation is too slow (of the order of 1 s for a 10-m-long magnet), one makes use of quench heaters that induce a fast (of the order of 10-50 ms) transition to resistive state in most of the magnet.

The best that one can do is to evenly spread this energy all over the magnet, and a trivial limit is the balance between the energy to dissipate and the energy needed to bring the coil to T_{max}. This sets an intrinsic limit to protection without dump resistor. We therefore consider the integral of the specific heat of the coil

$$C_p^{ave} \equiv \int_{T_o}^{T_{max}} c_p^{ave}(t)dt \;; \qquad (8)$$

this value depends on the materials (see Table 2). Nb-Ti has larger values than Nb_3Sn, but including insulation and voids (for Nb-Ti), they have a rather similar value of 0.5 J/mm^3. HTS materials have an enthalpy which is also in the same order of magnitude: here a reference cable is less established, and in Table 2 we give the YBCO tape used for FrescaII insert [7] and a BSSCO Rutherford cable.

Table 2: Typical integral of specific heat from 1.9 K to 300 K for superconducting coil used in accelerator magnets

	SC		Stabilizer		Insulation		Total
	(J/mm^3)	(%)	(J/mm^3)	(%)	(J/mm^3)	(%)	(J/mm^3)
Nb-Ti	0.64	0.33	0.71	0.33	0.27	0.18	0.49
Nb_3Sn	0.46	0.33	0.71	0.33	0.27	0.33	0.48
BSSCO	0.55	0.18	0.57	0.53	*0.27*	*0.18*	0.44
YBCO	negligible		0.65	0.67	*0.27*	*0.33*	0.53

Having found the hard limit, how far are we from it? An analysis of magnets built in the past 10-20 years, both short models and full-feature accelerator magnets as the LHC main dipoles, show that Nb-Ti magnets have an energy density of about 0.05 J/mm^3, i.e. about a factor 10 lower than the enthalpy limit. Since the energy scales with the square of the current, these magnets have about a factor three safety in current. For Nb_3Sn magnets we are entering a new regime, with energy densities of 0.10-0.12 J/mm^3, i.e., doubling the values of Nb-Ti and reducing the current margin from a factor 3 to a factor 2 only (see Fig. 2).

The capital Γ is independent of magnet length, and depends only on cable size. The tax in the case of no dump resistor is also independent of length, since both R and L scale with magnet length:

$$I_q = I_o \exp\left(-t\frac{R(t)}{L}\right); \qquad (9)$$

So the good news is that the <u>no dump strategy is independent of magnet length</u> – in this approximation, what works for a 1-m-long model will also work for 15-m-long magnet. Other phenomena, as quench-back, helping to spread the quench and increase the resistance may have a dependence on the magnet length.

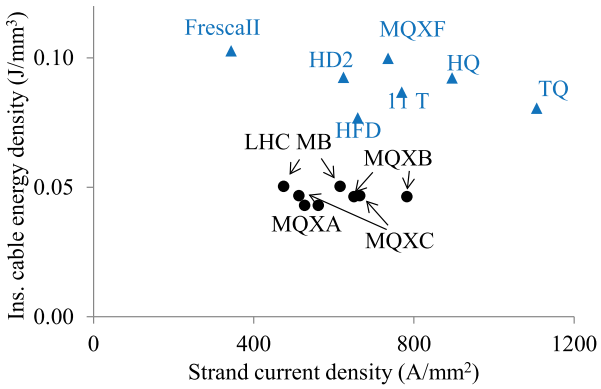

Figure 2: Energy density in the insulated coil for Nb-Ti (black circles), Nb_3Sn (blue triangles), and sketch of the limit given by the integral of specific heat.

TIME MARGIN

Definition

Many margins have been defined for superconducting magnets, as the loadline margin, the temperature margin, and the current margin. Here we define a margin for protection in case of no dump resistor. We define the capital as in (2), and the tax as in (3), and we consider a discharge of the magnet shorted on itself, without dump resistor, and having the whole magnet quenched at t=0. This is defining an ideal protection system that is able to quench the entire magnet instantaneously - difficult to make something better.

Instead of defining the margin in terms of "fiscal pressure", i.e. the ratio between tax and capital, we see how much of what is left after tax can be spent staying at operational current (see Fig. 3).

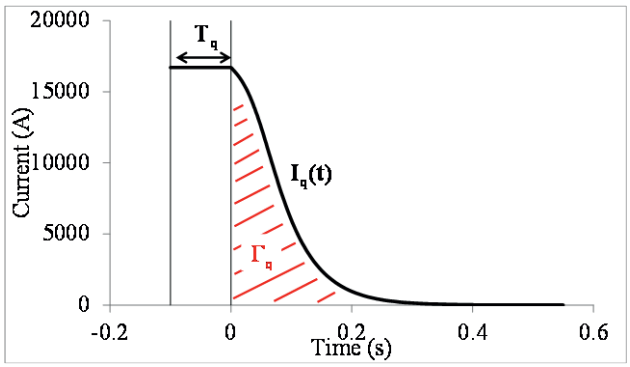

Figure 3: Definition of protection time margin.

$$I_0^2 T_q(T_{max}) + \Gamma_q = \Gamma(T_{max}) \qquad (6)$$

$$T_q(T_{max}) \equiv \frac{\Gamma(T_{max}) - \Gamma_q}{I_0^2} \qquad (7)$$

This is the time margin for protection, allowing to judge if the reaction time of the quench protection system is sufficient or not. The advantage is that the capital left is divided by the square of the current, allowing direct comparison between magnets with different currents (and therefore different cable cross-section, inductances, etc.).

Scaling

If we consider two cases as in Fig. 1, i.e. if we go from two to one layer, doubling the coil width, and keeping the same energy density, the time margin does not change. We remind the reader that to compute the time margin we always consider the case with a magnet fully quenched at time zero. In fact current will double, inductance will be divided by four, but resistance as well (a factor two from shorter cable, and a factor two from cross-section) so the time constant is preserved. So in case of no external dump, rearranging the same coil with less layers and larger cables does not affect the time margin.

Dependence on magnet features

An estimate of the time margin for several accelerator magnets is given in Fig. 4. One can see that Nb-Ti magnets as the LHC main dipole and the Nb-Ti option for the inner triplet upgrade have a time margin of 100-200 ms (depending on the layer, since the magnet is graded). Many cases of the new generation of Nb_3Sn have a time margin reduced by more than a factor two, to about 50 ms (HD2, HFD, MQXF and 11 T). The 90 mm and 120 mm LARP quadrupole have even lower margin, 20-30 ms. It is interesting to see that the copper fraction which is usually considered to be the crucial parameter for protection, is not the only player in the game. An important variable is also the current density, which plays a major role. One can prove [8] that the time margin scales with the inverse of the square of the current density

$$T_q = \frac{\nu}{\overline{\rho} j_0^2}\left[C_p^{ave} - \eta U_d\right] \qquad (8)$$

and, moreover, it depends on some intensive properties of the magnet as the integral of specific heat as defined in (8) and the energy density U_d over the coil, the copper fraction, and an average resistivity $\overline{\rho}$ of the stabilizer. Here η is a parameter that depends on the magnet design (in our case in the range of 2-3 for most magnets) which hides the complexity of the problem.

This equation points out several interesting features:

- Provided that you manage to spread the quench in the whole magnet, relevant quantities for hotspot are intensive properties (energy density, current density, resistivity, copper fraction) and not extensive ones (energy, inductance, current). So large stored energies are not a problem for hot spot, but large energy densities are.
- There is a strong dependence on the current density, so an effective way of improving the aspects related hotspot temperature is to avoid too large current densities. This is clearly visible in Figure 5: FrescaII has a large time margin since its operational current density is very low (200 A/mm^2). Conversely, TQ is a particular difficult magnet to protect due to its large current density of 750 A/mm^2, giving only 20 ms of time to quench all magnet before reaching hotspot temperature.

The case of the LARP quadrupoles of 90 mm (TQ), 120 mm (HQ) and 150 mm aperture (MQXF) [9] is particularly interesting since without any change in copper ratio but reducing the current density one has obtained an easier protection, notwithstanding the increasing stored energy.

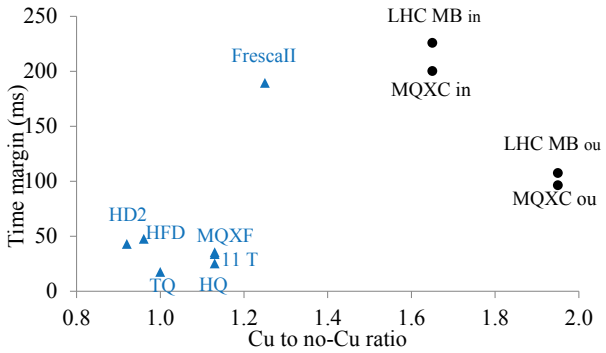

Figure 4: Time margin versus copper-no copper ratio, for Nb-Ti (black circles), and Nb_3Sn (blue triangles) magnets.

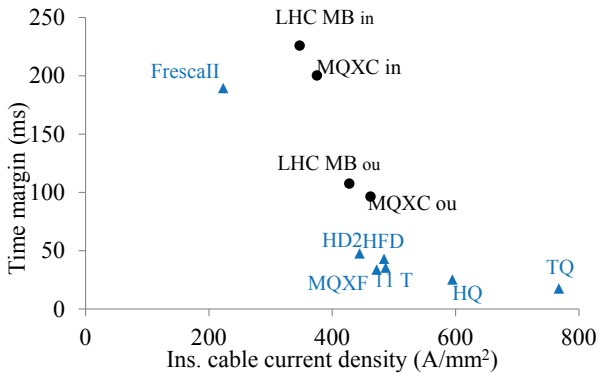

Figure 5: Time margin versus current density for Nb-Ti (black circles), and Nb_3Sn (blue triangles) magnets.

Dependence on local field

At low temperatures, the resistivity of copper strongly depends on the magnetic field. At 1.9 K and 12 T the resistivity is five times lower than at 1.9 K and 0 T. For this reason if the heat does not get averaged over the whole coil, one can have large differences in the time margin between high field and low field zones.

As an example in Fig. 6 we consider the case of the 120 mm aperture quadrupole HQ: the time margin varies between 25 ms at 12 T up to 45 ms at 2 T. Note that since the cable is considered to be the basic cell, and due to the transposition of the cable, there is no strand in the magnet that sees less than 2 T. If there is no heat diffusion we will have a larger budget for the low field zones, which will become useful soon. If the heat diffusion plays an

important role, this difference is smeared, with the effect of increasing the budget for the high field zones.

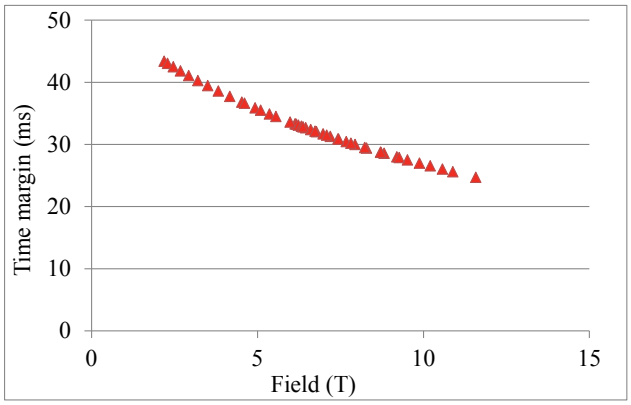

Figure 6: HQ time margin versus local field.

HOW TO SPEND THE TIME MARGIN

General budget

The time budget is the time available to the system to quench the entire magnet. It must be larger than the sum of different contributions:

- Detection time, i.e. the time needed to detect the quench. This is given by the resistance growth along the cable, related to the quench velocity, and to the thresholds used for detection.
- Validation time: once the threshold is reached there is a validation window (typically 5 to 10 ms) to avoid false triggers.
- Switch opening: typically 2 ms.
- Quench heater delay: time needed by the heaters to quench the magnet. It can be separated into:
    - Delay needed to start a quench somewhere in the coil – typically in the high field zone - what is usually measured as quench heater delay.
    - Delay between the start of the quench in the high field zone and the quench of the whole coil, including the low field zone.

In the following we will treat the detection time and the heater delay.

Detection time and quench velocity

A quench is detected through the measurement of a voltage generated by the resistive transition. To compensate for the inductive voltage during the ramp, voltages of two symmetric poles are subtracted. The lower the threshold, the smaller is the detection time: the typical values of thresholds used in the LHC are V_{th}=100 mV, fixed by the accelerator system.

The resistive voltage is proportional to the current and to the growing resistance, in first approximation as

$$V(t) = R(t)I_o = \frac{v_q t \rho}{A_{Cu}} I_o \tag{9}$$

where we define the quench velocity v_q. The resistivity is constant within 10% in the range between 2 and 40 K, so one can write the detection time as

$$t_{\det} = \frac{V_{th}}{v_q \rho} \frac{1}{j_{o,Cu}} \tag{10}$$

Typical values of current density in the copper of 1400 A/mm^2, copper resistivity at 12 T of 0.65 nΩ m, and quench velocity of 20 m/s give a detection time of the order of 5 ms for a quench in a high field zone in a 12 T operational field Nb_3Sn magnet.

For low fields one has two negative effects that tend to increase the detection time:

- The resistivity is considerably lower for lower fields: at 2 T one has a resistivity of 0.22 nΩ m, i.e. a factor three lower.
- The quench velocity is lower for low fields: it is proportional to the square root of the conductivity times resistivity divided by the temperature margin:

$$v_q \propto \sqrt{\frac{\rho\kappa}{T_{cs} - T_o}} \tag{11}$$

The temperature margin at 80% on the loadline, for Nb_3Sn is ~4.5 K in high field and ~12.5 K in low field (2 T), so the ratio is about a factor 3. The product resistivity times conductivity changes from 12 T to 2 T of a factor that can be estimated between 1 and 2, according to the sources. So in the most pessimistic case the quench velocity is 2.5 times smaller.

Putting together all the effects, one has a detection time which is 5 to 7 times larger in low field regions, increasing the detection time from 5 ms to 25 to 35 ms. These additional 20 to 30 ms are barely compensated by the larger budget available in the low field zone (see Figure 5). So quenches in low field zones are a critical issue due to larger detection times.

Heater delay

With a longitudinal speed of 10-20 m/s, a typical propagation from turn to turn of ~10 ms and between layers of ~50 ms, it appears clear that the growth of resistance due to the quench propagation is negligible, and the only way to have a fast dump is to quench most of the magnet rapidly through the quench heaters. So, the core of the protection problem is to model how the heat of the quench heaters propagates to the coil and how long it takes to quench the different zones of the coil.

A simple model is based on the estimate of the energy needed to bring the coil from the operational temperature T_o to the current sharing temperature T_{cs}

$$t_{del} \propto \int_{T_o}^{T_{CS}} c_p^{ave}(T)dT \tag{12}$$

This model has one free parameter and allows to estimate the ratio in the delay between different conditions.

The geometry of the heaters can be rather complex [11, 12]. For long magnets, heaters covering completely the

coil and providing the needed power would lead to too large voltages. Two strategies can be used to cope with this problem:

- heaters of smaller width, with a wavy shape that cover all cables every given longitudinal period (as in HQ);
- heaters with variable width, i.e. having heating stations spaces along the magnet axis (as in LQ). This can be also obtained with copper cladding as in the main LHC dipoles [13].

In both cases the magnet is quenched only in a few positions along the axis, and in between them one relies on quench propagation. For this reason the spacing of the stations or the period of the waves must be of the order of 100 mm, so that propagation over 50 mm at 20 m/s takes a few ms. A code is being recently developed to model the heat transfer from the heaters to the cables, relying on a 2 D thermal network, and allowing to simulate these complex geometries and to optimize them [12].

The delay has a nonlinear dependence on the current, being obviously zero at short sample, is roughly proportional to the thickness of the insulation between the heaters and the coil, and saturates at towards 50 W/cm^2 in case of a 0.025 mm thickness heater strip [14]. With the smallest insulation of 0.025 mm, and optimized heater power one can get, at 80% of the loadline, delays of the order of 5 ms. The delay, which is routinely measured during a test campaign, is obviously related to the quench in the higher field zone.

A second element that cannot be measured directly is the time needed to quench the lower field zones. The simple model based on the integral of the specific heat gives, again for the case of HQ, a factor 2.5 between the time needed to quench low field zone w.r.t. high field (see Figure 6). So in the hypothesis of 5 ms delay, another 10 ms are needed to completely quench the outer layer.

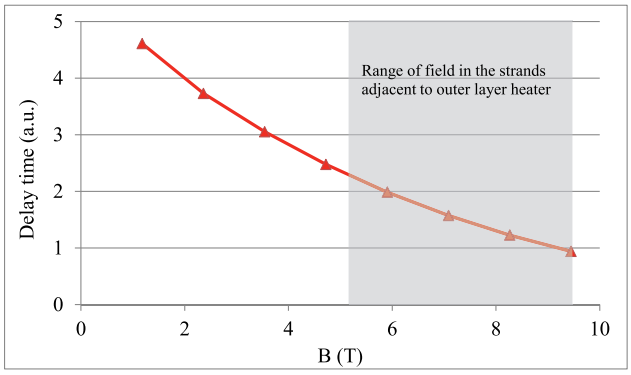

Figure 7: Delay time of quench heaters vs field for HQ.

The last piece of the puzzle is how to quench the inner layer. There are three possible strategies:

- have a quench heater glued on the inner part of the inner layer (as done in HQ). This heater, easy to add during the coil potting, has the disadvantage of not being supported and is prone to detachment that can reduce its efficiency during the magnet lifetime. Moreover, it constituted a barrier to the heat removal, which for this magnet is at 80% from the inner cold bore;
- have a quench heater in the interlayer. This option can be realized through building a heater that can resist to the Nb_3Sn heat treatment, or having a splice between the inner and the outer layer. The first option was tried and then abandoned in the HFD program [13];
- rely on the propagation of the heat from the outer to the inner layer, i.e. having the outer layer acting as a quench heater. This induces a considerable delay, which for the 11 T magnet has been estimated to 50 ms.

For both the MQXF, the inner triplet quadrupole of the LHC upgrade, and the 11 T dipole to make space for collimators, quenching the inner layer is a critical issue that is still to be solved. Putting together all the components, it appears clear that a time margin of 50 ms is at the limit of protection, whereas 20-30 ms are out of reach.

INDUCTIVE VOLTAGES

During the discharge, if the magnet has no external dump resistor and it is individually powered or has a by pass diode, the inductive voltage compensates the resistive voltage, i.e.

$$L\frac{dI(t)}{dt} + R(t)I(t) = 0 \qquad (13)$$

where L and R refer to the induction and to the resistance of the whole magnet. If the magnet is quenched in the segment a to b, and is superconductive in the segment from b to c, with a and c being the ends of the magnet, one has

$$(L_{ab} + L_{bc})\frac{dI(t)}{dt} + R_{ab}(t)I(t) = 0 \qquad (14)$$

and a voltage appears within the magnet

$$V_{ab} = L_{ab}\frac{dI(t)}{dt} + R_{ab}(t)I(t) = -L_{bc}\frac{dI(t)}{dt} \qquad (15)$$

Please note that here L_{ab} denote the inductance of a segment of the magnet, defined as the ratio of the measured inductive voltage during a discharge and the derivative of the current. The maximum acceptable inductive voltage is related to the magnet insulation and is of the order of 1 kV. One can point out the two main scaling related to inductive voltages:

- The <u>inductive voltage is proportional to the magnet length</u>. So for a given cross-section there is a maximum magnet length above which inductive voltages are not acceptable;
- <u>A magnet with larger cable has lower inductive voltages</u>; let us compare as for the hotspot temperature two cases with same field, stored energy, one with a double layer with width w, and the second with a single layer with width $w'=2w$. One has

$$I_o' = 2I_o \qquad L' = \frac{L}{4} \qquad R' = \frac{R}{4} \qquad (16)$$

and the voltage of the one layer case is a factor two smaller than the two layer case

$$V' = \frac{V}{2} \ . \qquad (17)$$

We estimated the inductive voltage in the case of a magnet which has the outer layer totally quenched and the inner layer superconductive. This is what happens at the beginning of the quench for magnets with outer layer quench heaters. We considered an extreme case where the inner layer never quenches. Simulations are shown in Fig. 7 shows for six magnets including the LHC main dipoles.

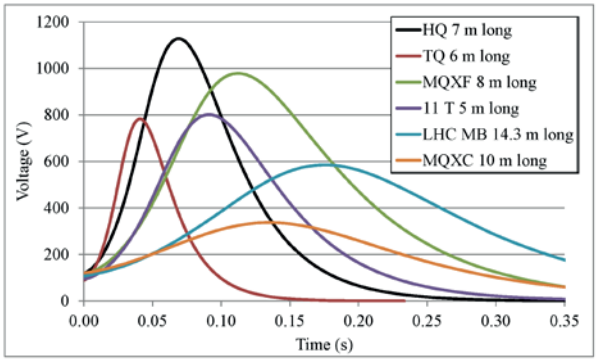

Figure 8: Estimate of inductive voltage in four Nb_3Sn magnets, and in two Nb-Ti magnets, due to unbalance with inner layer not quenched and outer layer totally quenched.

In many cases the resistance of the outer layer is not enough to guarantee a hotspot temperature below 300 K: after a certain time one has to quench also the inner layer, so the significant part is this simulation are only the first 50-100 ms. It turns out that all cases are in the range of 500-1000 V, so close to the threshold. This means that these designs associated with their magnet lengths are just at the limit of the tolerance for this case: magnets with significantly longer length would require a different design of the coil.

CONCLUSIONS

The new generation of Nb_3Sn magnets, with peak fields in the range of 10-15 T, poses novel challenges for protection. Here we reviewed the aspects related to the hot spot temperature. We first considered the case of short magnets individually powered, which can be protected with external dump resistor and which profit of large cables and small inductances. Then we analysed the case of long magnets, or chain of short magnets, where the dump resistor strategy is not effective: large or small cables make no difference, and the magnet itself has to absorb its energy, relying on quench heaters.

We defined a novel concept of time margin, which gives the time allowed to the protection system to react before the magnet reaches too high temperatures, and we presented the relevant scaling law. This time margin allows to compare directly different designs and technologies. It turns out that if the Nb-Ti magnets had a time margin of 200-100 ms, with the new generation of Nb_3Sn magnets the margin is 50 ms, and even 20-30 ms in some cases. The exception is FrescaII, since it relies on a very large coil and small current density.

We then discussed the time of reaction of the system, from the start of the quench to the instant at which all the magnet is quenched by the heaters. We discussed the different contributions, pointing out that a quench in a low field region can be as challenging as a quench in the high field regions, due to a larger margin, longer time to detect and a lower quench velocity. In general, one can state that 50 ms reaction time is challenging but typically achievable, whereas 30 or 20 ms seem impossible to achieve with present experience and technologies.

We finally discussed the main scaling for the inductive voltages that arise during quench. In this case, large cable and small inductances allow reducing the voltages. On the other hand, the voltages scale with the magnet length so they impose an upper limit to the magnet length.

REFERENCES

[1] L. Bottura, these proceedings.
[2] L. Imbasciati, Quench Protection Issues of Nb3Sn Superconducting Magnets for Particle Accelerators, Fermilab thesis, 2003, available at: http://lss.fnal.gov/archive/thesis/2000/fermilab-thesis-2004-14.pdf.
[3] G. Ambrosio, these proceedings.
[4] H. ten Kate, talk given at WAMSDO, https://indico.cern.ch/contributionDisplay.py?contribId=22&confId=199910.
[5] P. Fazilleau, these proceedings.
[6] J. M. Rifflet, M. Segreti, Studies on large aperture Q4 with MQ and MQM cables – I, II and II part, http://www.cern.ch/hilumi/wp3.
[7] A. Stenvall, these proceedings.
[8] E. Todesco, private communication.
[9] P. Ferracin, LARP Nb_3Sn quadrupole magnets for the LHC luminosity upgrade, Adv. Cryo. Eng. 55 (2010) 1291-1300.
[10] L. Rossi, M. Sorbi, INFN/TC-04/13 MATPRO: A Computer Library Of Material Property At Cryogenic Temperature, CARE-Note-05-018-HHH.
[11] H. Felice, these proceedings.
[12] T. Salmi, these proceedings.
[13] B.Szeless et al., LHC Project Report 48, ICEC (1996).
[14] H. Felice, Instrumentation and Quench Protection for LARP Nb_3Sn Magnets, IEEE Trans. Appl. Supercond. 19 (2009), 2458-62.

QUENCH PROTECTION ANALYSIS IN ACCELERATOR MAGNETS, A REVIEW OF THE TOOLS

H. Felice, LBNL, Berkeley, CA 94720, USA
E. Todesco, CERN, Geneva, Switzerland

Abstract

As accelerator magnets see the increase of their magnetic field and stored energy, quench protection becomes a critical part of the magnet design. Due to the complexity of the quench phenomenon interweaving magnetic, electrical and thermal analysis, the use of numerical codes is a key component of the process. In that respect, we propose here a review of several tools commonly used in the magnet design community.

INTRODUCTION

Understanding the way the quench develops in the magnet and designing the appropriate protection scheme are key components of present accelerator magnet design. From the quench initiation and detection to the firing and connection of the protection elements, an ideal code would need to couple magnetic, electrical and thermal analysis. Nevertheless, the complexity of the topic leads to simplification in most of the codes commonly used. The disadvantage of a code containing all the physics is that computational times become long, not allowing parametric analysis. A common technique is to slice the problem, i.e. relying on different codes for different physical phenomena, and interfacing them.

In general, the user should choose the code depending on the most relevant physical phenomena she/he wants to model. Important added values of a code lies in (i) its ability to easily implement the geometry and the parameters of the magnet, (ii) the computational speed, (iii) the transparency of its contents, of the implemented physics and related approximations.

Even if not exhaustive, the review of the codes proposed in this paper is an attempt to provide some insight to the reader. We choose to distinguish two main categories of codes: the first one can be identified as "highly specialized" codes, dedicated to quench analysis, the second ones covers examples of Finite Element (FE) codes applied to quench protection analysis such as ANSYS or Cast3M.

CODES CLASSIFICATION

Physics

The simplest level of modelling is Adiabatic Model, i.e. the implementation of the well-known equation that gives the balance between Joule heating due to the current and temperature increase through specific heats, ignoring the propagation of the heat through the coil. Since the specific heats and the resistivity have a pretty complex dependence on the temperature, the equation needs to be numerically integrated. An input parameter is the fraction of the coil which is in a resistive state; a second input parameter can be the quench velocity, allowing increasing the fraction of resistive coil with time to model quench propagation. QuenchPro are examples of adiabatic codes.

The second level of approximation is to include the Heat Propagation within the coil. According to the complexity of the geometry, this implies having a multidimensional mesh of the coil and insulation (eventually including ends). The code has to incorporate the magnetic field distribution in the coil and to include a model of the critical surface. It can therefore estimate the quench velocity, which becomes an output parameter.

The third level of approximation is to include also the Heat Exchange between the coil and the helium bath. This aspect is very relevant for fusion, where the cable in conduit is designed to have a large heat removal through the helium bath. For the impregnated coils of Nb_3Sn this aspect is absent, whereas for the case of Nb-Ti coils permeated by helium, this aspect can play a more important role. In most cases for accelerator magnets, the heat exchange is ignored, and this approximation is considered to be conservative.

Geometry

The geometry of the coil is pretty complex, and trying a full modelling at the level of the cable plus insulation, or even for strand plus impregnation/voids and insulation may lead to prohibitive computational times. So it is wise to go by successive approximations. The origin of the complexity of the problem is (i) the large range of magnetic field in different parts of the coil, producing large differences in copper resistivity at low temperature, and (ii) the large variation of the specific heats with temperatures in the metal and in the resins.

The hierarchy of geometry modelling can be given as follows, from the simplest to the most complex level.

- Model the coil as a whole, with an average magnetic field and homogenized material properties.
- Model the coil having different layers, each one with its magnetic field.
- Model at the level of cables, each one with its magnetic field. The transposition of cables provokes an averaging over the different strands within the same cable.
- In principle one can think about reaching the level of strands: in this last case the void, insulation, and helium are modelled separately.

As far as we know, the modelling at the level of strands has never been done for accelerator magnets. On the other hand, this is done for cable in conduit used in fusion, where the complexity of the coil is not needed, so the

model is just one cable, and the heat exchange between strands and between strand and helium is relevant.

If the model relies on a finite element module, the geometry is a mesh at the level of coil, layer, cable and (in principle) strand. The model can be an extrusion of the two dimensional cross-section, ignoring ends, or include the geometry of the ends. For the estimate of the hotspot temperature including the ends brings an additional complexity without adding anything relevant.

Magnetic field and inductance

The map of the magnetic field on the components/nodes of the geometrical model can be computed externally, i. e. is an input, or within a magnetic module of the code. This does not make a significant difference, except from the point of view of the computational time, the second option being more user friendly but much heavier.

What can be relevant in the case of very high field magnets with iron close to the coils is the impact of saturation. If the field map is simply scaled with the current the model is linear and the saturation is neglected. Otherwise, if the code has an internal algorithm to estimate the saturation, at each time iteration the field map is estimated (as in ANSYS or in ROXIE).

In case of significant saturation, the most important effect is its impact on inductance, which becomes dependent on the current. At each integration step one has to use the differential inductance to estimate the current decay. This effect can be estimated with a separate code, so that the inductance is a nonlinear known function of the current (as in the latest version of QuenchPro), or internally estimated through the code itself (as in ROXIE).

Circuit

All codes are usually able to simulate a circuit with the coil and a dump resistor. The current decays with instantaneous time constant $L/R(t)$, where L is the differential inductance of the magnet and R is the total resistance of the circuit, i.e. coil plus dump resistor. The resistance strongly depends on time, since the coil is heating. The inductance also depends on time if the saturation is non-negligible, since the current decays with time (see previous subsection).

A few codes are able to simulate a magnet made by several coils independently powered (as for instance QLASA). In this case one has several circuits coupled through the mutual inductances.

Quench heaters

For long and high field accelerator magnets, as the Nb-Ti main LHC magnets or the Nb_3Sn HL-LHC triplet, the development of resistance due to the propagation of the spontaneous quench is negligible for estimating the hotspot temperature. On the other hand, the main mechanism is the development and propagation of the quench induced by the heaters. Several codes (QuenchPro, QLASA, …) are simulating it by initiating secondary quenches. A more complete simulation should include the heat propagation from the quench heaters to the coils. This problem can be treated separately through integration of heat equations, knowing the thermal properties and the critical surface; a network model has shown good results allowing modelling this complex phenomenon without free parameters [1]. Up to day this approach has not been fully integrated in the standard quench codes for superconducting accelerator magnets but the results of the simulation are used as inputs of other codes such as QLASA, QuenchPro or ROXIE.

CODES DEDICATED TO SUPERCONDUCTING MAGNETS

Various codes addressing similar or complementary aspects of quench protections in superconducting magnets for accelerators have been developed in the past years. We propose here a summary of some codes frequently used by the accelerator magnets community.

QuenchPro

The QuenchPro is an adiabatic code where the coil is modelled at the level of layers. Coil ends are ignored. The field and inductance treatment is linear, but a nonlinear inductance has been introduced recently. Up to 16 layers can be modelled, but not with independent powering. The ouput provides two main parts:

- The first one is dedicated to temperature and resistance growth, hotspot temperature estimate and current decay computation.
- The second part focuses on voltages computation.

The magnet is subdivided in 16 sub-coils powered in series. The user has to provide the longitudinal quench propagation velocity for each layer; there is no propagation from turn to turn. Moreover, the user has the possibility to define the protection heater coverage, the value of the dump resistor and various delay times representative of the actual magnet protection scheme such as protection heater delay, quench detection time, validation window, switch time and so on. The material properties are homogenised over the cross-section of the conductor.

In the second part, the coordinates of all the turns in the magnet are defined allowing the computation of a turn-to-turn inductance matrix. This matrix along with the first part results (temperature, resistance and current decay) is then used to compute turn-to-turn and turn to ground voltage.

The program is presently written as a Mathcad spreadsheet. It has been developed at Fermilab by Pierre Bauer [2] and is presently available upon request to users like Giorgio Ambrosio at FNAL (giorgioa@fnal.gov).

QLASA

The QLASA is also an adiabatic code where the coil is modelled at the level of layers. The program has been developed at LASA [3]; programmed in Fortran 77, it was

initially intended for quench analysis in superconducting solenoids and inductively coupled elements.

Despite the fact that the geometry is based on solenoids, it can be adapted to dipoles/quadrupoles with proper care requiring some discussions with the code developer (Massimo Sorbi) [3]. Ends are ignored, and field and inductance are treated linearly. Independent powering of different coils can be modelled.

The analysis is relying on an extensive material properties database MATPRO [4] and the default configuration of the program computes the quench propagation velocity based on these properties and the analytical formula. Nevertheless, the user has the flexibility to choose among several quench propagation velocity models or to input the quench velocity. As in QuenchPro, the program does not include thermal analysis and protection heaters are simulated using their delay as variable.

A strong feature of this code is to address the possibility of powering various layers with different power supplies or even without power supply in persistent mode.

ROXIE Quench Module

The ROXIE Quench Module [5, 6] is an addition to the existing field computation program ROXIE developed at CERN [7], modelling the heat propagation within the coil. The geometry relies on the ROXIE input, at the level of cables. Then the straight section is discretized, ignoring the ends. The field map is estimated internally at each time step, including saturation if needed. The quench module uses a thermal network with a node per cable to solve the heat equation. The insulation between cables is also modelled with one node. From an electrical view point, the model assumes that the magnet is connected to an electrical circuit made of current source, diodes, extraction resistance. The critical surface of the superconductor, as the coil geometry and the magnetic field, is already available from the main ROXIE module.

The strength of this approach comes from the fact that it is integrated with the existing software, making many features and outputs from ROXIE available in the quench module with minimal work from the user. An example is the differential inductance of the magnet which is used in the electrical network. Another example is the use of coupling current losses in the heat equation as a heating factor of the conductor before quenching (called quench-back).

On the other hand, computational times require keeping the discretization to a limited number of nodes, which is not always enough for proper convergence. Therefore in some cases the user has to rescale some physical properties (as thermal conductivity) to match the measured values of the quench velocity.

Details on the numerical approach can be found in [5] and details on material properties are described in [6]. Some outputs of the code include voltage distribution, hot spot temperature and current decay.

Even if the core of the quench module is developed, and distributed as part of the ROXIE package, some developments are still being performed in particular regarding the modelling of the protection heaters which for now relies on a scaling factor tuning the heat transfer from the protection heaters to the conductor [8].

Quench Analysis Program of Vector Field

The Quench Analysis Program is one of the analysis programs of the Opera-3D Analysis Environment from the Cobham Vector Field software [9]. It is a code that accounts for heat exchange in the coil (HE), based on the TEMPO/ Transient Thermal Analysis solver. It is coupled with the analysis of the electrical circuits and to the estimate of the fields in the conductors. The geometry is at the level of the cables (CA) and relies in the Vector Field input file. Homogenized material properties are used and need to be provided as part of the model creation.

In addition to the hot spot temperature and resistance growth computation, an interesting feature of the program is that it can be coupled with the ELEKTRA Time Varying Analysis to model transient electromagnetic fields and external circuits. This can be particularly useful in simulating transient eddy current in external magnet structure in thermal contact with the coils commonly referred as quench-back phenomenon. Despite these nice features, the software does not provide voltage computation. Voltage development being an important concern for long magnets, output post processing by the users is necessary.

Presently, the code is being used to perform the quench analysis of the MICE spectrometer and shows good agreement with test data [10]. Results are still to be published.

Regarding application to accelerator magnets, based on the experience of the authors so far, computation time remains very large which could be a showstopper.

GENERAL CODES

In addition to the specialized codes, the use of commercial finite element codes is another way to model magnets and perform quench protection analysis. In both cases the codes model the heat propagation through the coil. Once the geometry is modelled, the program contains modules which account for the physics of the problem.

Cast3M

Cast3M is a FEM code developed at CEA [11] and available at [12]. It is used at CEA/Saclay to perform eddy currents computation. An example is the case of CMS (Compact Muon Solenoid), where eddy currents were computed in the so-called quench-back cylinder [13, 14].

ANSYS and other commercial codes

ANSYS is a well-known FEM software available commercially. Some past work performed by Yamada et al. [15] and S. Caspi and P. Ferracin [16, 17] shows the advantage of such multi-physics models. In particular, with the increasing hot spot temperature in very demanding system, the capability to couple thermal and mechanical analysis is very interesting.

CONCLUSION

This paper presents some codes commonly used in the community to perform quench protection analysis. The list is not exhaustive and many laboratories have their own "in-house" codes. In addition, considering quench protection codes used in the fusion community would also be highly beneficial. The attempt to collect more information about these various codes is still in progress.

ACKNOWLEDGMENT

The authors would like to thank Giorgio Ambrosio, Berhnard Auchmann, Philippe Fazilleau, Massimo Sorbi, Heng Pan, Lidia Rossi, Tiina Salmi for their help.

REFERENCES

[1] T. Salmi et al., Modeling quench protection heaters in Nb_3Sn accelerator magnets, this proceeding.

[2] P. Bauer et al., Quench Protection Calculations for Fermilab's Nb3Sn High Field Magnets for VLHC – Part 1,nFNAL TD-01-003, February 2001.

[3] L. Rossi, M. Sorbi, QLASA: a computer code for quench simulation in adiabatic multicoil superconducting windings, INFN/TC-04/13, 2004, and V. Marinozzi, Guidelines for the quench analysis of Nb3Sn accelerator magnets using QLASA, FNAL TD report TD-13-008; http://tdserver1.fnal.gov/tdlibry/TD-Notes/2013%20Tech%20Notes/TD-13-008.pdf.

[4] L. Rossi, M. Sorbi, MATPRO: a computer library of material property at cryogenic temperature, CARE-Note-05-018-HHH, 2005.

[5] N. Schwerg et al., Quench Simulation in an Integrated Design Environment for Superconducting Magnets, IEEE Trans. On Magn., Vol. 44, N. 6, June 2008.

[6] N. Schwerg et al., Challenges in the Thermal Modeling of Quenches With ROXIE, IEEE Trans. On Appl. Supercond, Vol. 19, No. 3, June 2009.

[7] S. Russenschuck, ROXIE: Routine for the Optimization of Magnet X-Sections, Inverse Field Calculation and Coil End Design, Ed. Geneva, Switzerland: CERN, Apr. 1999.

[8] B. Auchmann, CERN, private communication.

[9] http://www.cobham.com/about-cobham/aerospace-and-security/about-us/antenna-systems/kidlington.aspx

[10] H. Pan, LBNL, private communication.

[11] P.Verpeaux, T. Charras, and A. Millard, CASTEM 2000 une approche moderne du calcul des structures, in Calcul des structures et intelligence artificielle, Pluralis, 1988, pp. 261–271.

[12] http://www-cast3m.cea.fr/

[13] P. Fazilleau, CEA, private communication.

[14] P. Fazilleau et al. The R3B-GLAD Quench Protection System, IEEE Trans. On Applied Superconductivity, Vol. 20, No. 3, June 2010.

[15] R. Yamada et al. 2D/3D Quench Simulation Using ANSYS for Epoxy impregnated Nb3Sn High Field Magnets, IEEE Trans. On Applied Superconductivity, Vol. 13, No. 2, June 2003.

[16] S. Caspi et al., Calculating Quench Propagation With ANSYS, IEEE Trans. Appl. Supercond, Vol. 13, No. 2, June 2003.

[17] P. Ferracin et al., Thermal, Electrical and Mechanical Response to a Quench in Nb3Sn Superconducting Coils, IEEE Trans. Appl. Supercond, June 2004.

QUENCH IN HIGH TEMPERATURE SUPERCONDUCTOR MAGNETS*

J. Schwartz, Department of Materials Science and Engineering, North Carolina State University, Raleigh, NC 27695, USA

Abstract

High field superconducting magnets using high temperature superconductors are being developed for high energy physics, nuclear magnetic resonance and energy storage applications. Although the conductor technology has progressed to the point where such large magnets can be readily envisioned, quench protection remains a key challenge. It is well-established that quench propagation in HTS magnets is very slow and this brings new challenges that must be addressed. In this paper, these challenges are discussed and potential solutions, driven by new technologies such as optical fiber based sensors and thermally conducting electrical insulators, are reviewed.

INTRODUCTION

High temperature superconductor (HTS) wire technology has matured sufficiently such that there is an increasing effort to use them to generate high magnetic fields for applications including high energy physics, energy storage and nuclear magnetic resonance [1]. Of the superconductors discovered since 1987, two conductor technologies have emerged with the potential to generate magnetic fields well above 25 T, the limit of low temperature superconductor (LTS) technologies. One of these options, Ag/Ag-alloy clad $Bi_2Sr_2CaCu_2O_x$ (Bi2212), is the only HTS round wire (RW) with high critical current density (J_c) in magnetic fields above 20 T [2-6]. The manufacturing of Bi2212 RW has advanced sufficiently for the construction of insert coils that generate magnetic fields above 25 T [6-9]. The primary limitation of Bi2212 RW is a lack of mechanical strength. The other options, $(RE)Ba_2Cu_3O_{7-z}$ (REBCO) coated conductors, are comprised of a thin layer of REBCO superconductor deposited on a complex Ni-alloy substrate with one or more oxide buffer layers and subsequently encased in Cu. REBCO coated conductors have very high J_c in the REBCO layer and very high mechanical strength in axial tension due to the Ni-alloy substrate, but are only available in a wide tape geometry. Although cabling options have been proposed, none clearly satisfies the requirements for cost-effective high field magnets [10, 11].

To safely operate a large, high field superconducting magnet, regardless of conductor type, a thorough understanding of the quench behavior of the conductor and magnet is required. Although the quench behavior of LTS-based magnets is well understood, HTS magnets show distinctly different quantitative behavior [12, 13]. For example, the minimum quench energy (MQE) in HTS magnets is quite high but the corresponding normal zone propagation velocity (NZPV) is a few orders of magnitude slower than in LTS magnets [13-23]. Thus, while the basic physics of quench behavior is unchanged, from a practical perspective the quantitative differences in behavior dominate.

The aim of any quench protection system is to prevent permanent conductor degradation in the event of a fault condition that induces a quench. As illustrated in Fig. 1, quench protection involves three key steps, all of which must be accomplished within a time-budget determined by the rate of growth of the disturbance and the resilience of the conductor. The three key steps are: (1) detection of a disturbance (historically accomplished with voltage measurements), (2) assessment of the disturbance to determine if it is going to induce a quench and to prevent false-positives, and (3) a protective action to prevent degradation if the magnet is quenching. For large magnets with a large stored energy, this is typically accomplished through heaters embedded in the magnet and a dump circuit into which the stored energy is dissipated. Thus, to develop an effective quench protection system, one must understand the stability and quench dynamics of the magnet in order to design a detection system, and one must also know the safe operational limits of the conductor. These two factors determine the time budget for protection. For LTS magnets, the safe operational limits are quantified in terms of a maximum hot-spot temperature; it is unclear if this is a sufficient criterion for HTS magnets.

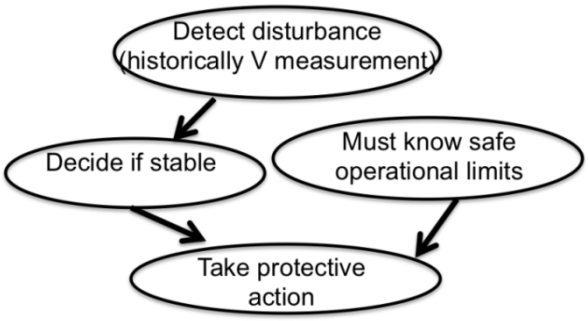

Figure 1: Illustration of quench protection workflow.

In considering the quench behavior of high field HTS magnets, it is important to recognize that such magnets are likely to be LTS/HTS hybrid systems, with LTS outsert coils that generate around 18 T and HTS insert coils that generate the highest magnetic fields [1]. Thus, other than during field ramp-up (in single power supply magnet systems), the HTS conductor will only be exposed to high magnetic fields and the behavior at low field is less important. Although most studies on HTS quench behavior have focused primarily on the behavior at self-field or relatively low magnetic field [24, 25], one recent study focused on the effects of high magnetic fields on quench behavior in Bi2212 RW coils [26]. The primary

question was whether high magnetic field would increase the NZPV due to reduced critical temperature (T_c) and thus reduced current sharing temperature (T_{cs}) and temperature margin, or instead whether the NZPV would decrease due to reduced J_c. Fig. 2 plots the magnetic field dependence of the NZPV, I_c, MQE, T_c and T_{cs} for two Bi2212 coils and strands. While the MQE decreases with increased magnetic field for magnetic fields up to 20 T (the maximum reported), the NZPV is magnetic-field independent for fields greater than about 10 T. Thus, increased magnetic field results in reduced stability margin but not in enhanced propagation.

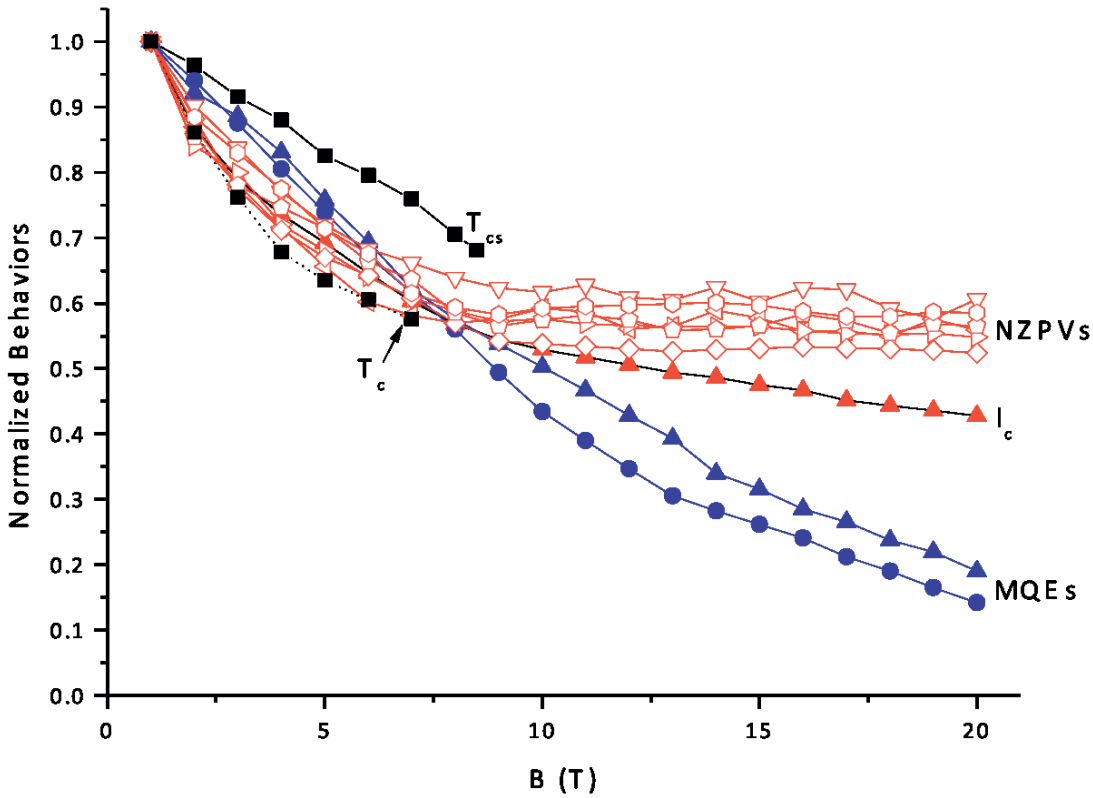

Figure 2: Normalized magnetic field-dependent quench behaviors [26].

DEGRADATION IN HTS CONDUCTORS

The key to quench protection is preventing degradation by limiting localized temperature growth relative to the ability to detect and protect within the time available before degradation occurs. To determine the time budget, one must understand both the quench dynamics and the operational limits of the conductor. The safe operational limits for Bi2212 and REBCO conductors, however, are likely to not only be quite different from the limits on LTS conductors, but also from each other. Bi2212 RWs have defect-dominated microstructures with a significant quantity of interfilamentary bridges, porosity, non-superconducting phases, and $Bi_2Sr_2CuO_z$ intergrowths within the Bi2212 grains. Thus, electrical transport in Bi2212 RWs is not well understood, and identifying microscopic causes of reduced electrical performance is particularly challenging [3, 4]. Unlike Bi2212, REBCO coated conductors have highly engineered microstructures with very few unintended defects. Often non-superconducting, nanoscale defects are intentionally grown within the REBCO phase for enhanced flux pinning, but nonetheless the REBCO remains highly dense and relatively homogeneous [27-30].

Bi2212 RWs

While the mechanisms of Bi2212 degradation are not understood, two studies have investigated the safe operational limits of Bi2212 mulitiflamentary tapes and RWs [24, 31]. These studies have induced quenches in short strands and small test coils and allowed the quench to proceed systematically until the conductor degrades. The temperature-time data was interpreted in terms of the maximum temperature (T_{max}), the maximum temperature gradient ($dT/dx|_{max}$) and the maximum rate of temperature increase ($dT/dt|_{max}$); information about the conductors is seen in Table 1 and results are seen in Table 2. The results indicate that thermal shock ($dT/dt|_{max}$) is not the underlying driver for degradation. Furthermore, it is difficult to differentiate between the effects of T_{max} and $dT/dt|_{max}$, and it is likely that both play a role in Bi2212 degradation.

Table 1: Performance of Bi2212 RWs Used in Quench Study [31]

Sample	I_c (A)	J_c (A/mm^2)	I_t (A)	I_t/I_c	J_{Ag} (A/mm^2)	MQE (J)	NZPV (cm/s)
Wire I, strand	550	2334	450	81.8%	1000	1.61	11.2
Wire I, coil	500	2122	400	80.0%	909	2.38	3.6
Wire II, strand	500	4420	410	82.0%	1284	0.78	17.4
Wire II, coil	360	3183	290	80.2%	924	1.75	6.3

Table 2: Safe Operational Limits in Bi2212 RWs [31]

Sample	T_{max}(K)		$dT/dt\|_{max}$(K/s)		$dT/dx\|_{max}$(K/cm)	
	Highest without degradation	Lowest with degradation	Highest without degradation	Lowest with degradation	Highest without degradation	Lowest with degradation
Wire I, strand	317	350	695	700	95	100
Wire I, coil	330	358	770	802	82	93
Wire II, strand	193	200	592	605	65	66
Wire II, coil	139	167	219	255	43	48

REBCO Coated Conductors

The onset of degradation in a straight REBCO coated conductor was studied using a similar procedure as the Bi2212 study [20]. In this case, it was found that, when T_{max} reached 490 K (±50 K), the conductor I_c was degraded by ~5%. This corresponded to a strain of about 0.31%, which was ~60% of the irreversible strain reported for this conductor. In this experiment, $dT/dt|_{max}$ ~ 1800 K/s; values for $dT/dx|_{max}$ were as high as 27 K/mm, but the limited spatial resolution of the thermocouples implies that this value is probably lower than the actual temperature gradient in the conductor.

The microstructure of a degraded YBCO coated conductor was also studied via an etching technique that exposed the YBCO surface, facilitating microscopy of the surface [32]. In this study, the quenched sample experienced a 6.3% reduction in I_c. To expose the YBCO surface, the Cu stabilizer was first removed by a Cu etchant that contained S. Reactions between S and YBCO, seen after removal of the Ag cap layer, proved to be a signature of Ag/YBCO delamination (i.e., if the Ag/YBCO interface had not been breached during quenching, then the S would not have had access to the YBCO layer during etching of the Cu). This study showed clearly that pre-existing defects in the YBCO are the initiation points of subsequent degradation; two different defect structures were identified. At the edge of the conductor, where slitting occurs during conductor manufacturing, defects in the form of either the absence of Ag or delaminated Ag result in very high local electric field during a quench. This large, local electric field induces dendritic flux avalanches and a very high local temperature rise. The high temperature then causes further Ag delamination and a self-propagating effect which results in dendritic Ag delamination. The dendritic delamination in turn results in very narrow channels which facilitate Cu etchant penetration and a chemical reaction between S and YBCO. As a result, the microstructure shows a dendritic reaction pattern; EDS confirms that the dendrites have a high S content. This is seen in Fig. 3 and Fig. 4.

The other type of defect, labelled Q3 in Fig. 3, is observed within the YBCO layer but away from the conductor edge. This defect results in a reaction zone that shows significant S content. In this case, the Ag is both delaminated from the YBCO layer and breached such that Cu etchant penetrated and reacted with the underlying YBCO. As seen in Fig. 3 and Fig. 5, the degradation zone is nearly a perfect circle, indicative of current streamlines with a sharp boundary. An EDS map (Fig. 5) shows similar reactions as in the edge degradation, but also showed pure Ag particles (Fig. 6), which indicates that the local temperature was sufficient to create a Ag vapor that, upon cooling, results in such fine Ag precipitates.

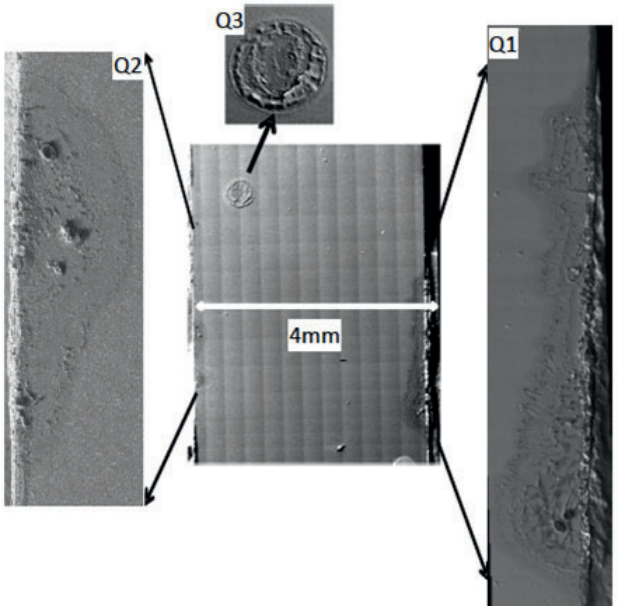

Figure 3: SEM micrographs of etched YBCO coated conductor, illustrating the two types of defects seen [32].

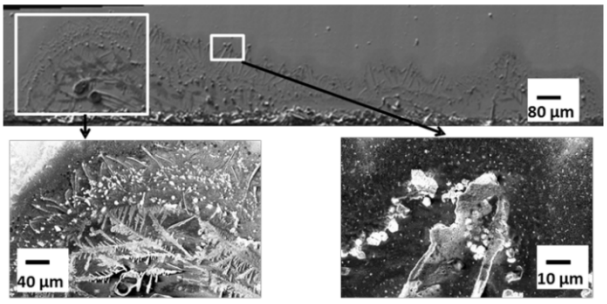

Figure 4: SEM micrographs of etched YBCO coated conductor, illustrating dendritic penetration from the edges [32].

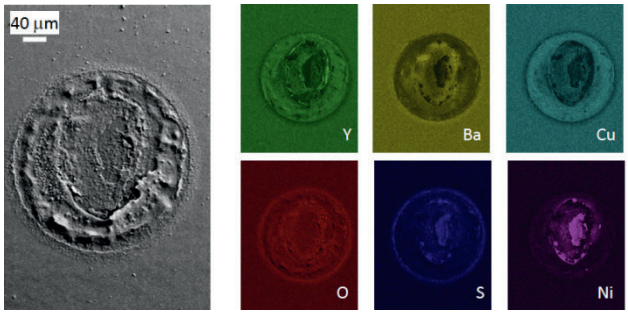

Figure 5: SEM micrographs and EDS maps of etched YBCO coated conductor, illustrating the degradation zone away from the conductor edge [32].

Degradation Discussion

Degradation in Bi2212 and REBCO conductors is quite different and generalized conclusions cannot be made. In fact, as both of these conductors are still under development, it is difficult to make quantitative conclusions that will be applicable to future conductors with improved properties. Nonetheless, some meaningful conclusions can be drawn. For Bi2212, the safe operational limits have large windows of uncertainty, which may be related to the inhomogeneous microstructure as well as differences in the way the wire was supported during the experiments. Bi2212 is mechanically relatively weak and thus improvements to operational limits may require significant improvements in the Bi2212 filament microstructure as well as the overall mechanical behavior of the conductor (e.g., a strengthened sheath [33]). For REBCO, there are also differences between different conductor types. Since the degradation is clearly initiated at manufacturing defects in the conductor, however, as the manufacturing processes improve it is likely that the conductor will become more quench resilient. One concern, however, is that that the susceptibility to degradation is related to the very high J_c in the REBCO layer. Because these conductors have a low fill-factor, high J_c in the REBCO layer is essential to their success.

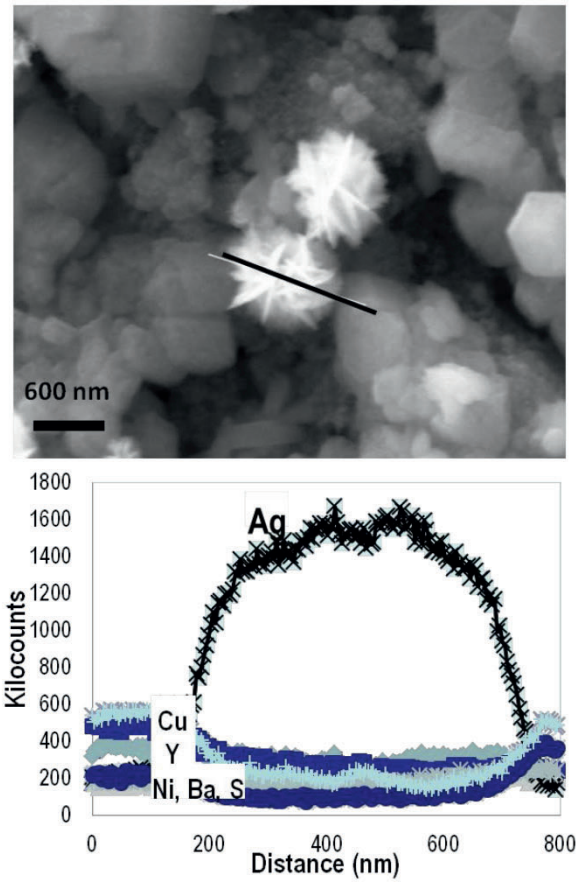

Figure 6: SEM micrograph within one of the rings in the reaction zone of Fig. 5, and an EDS line scan showing that this is a Ag precipitate [32].

QUENCH DETECTION CHALLENGE

From the perspective of quench protection, the challenge of slow NZPV is quench detection; if the normal zone does not propagate quickly then neither does a detectable signal which may result in degradation before a protection system can take action. In principle, slow NZPV may also expand the time-budget, in which case the delayed detection would not be problematic as the two effects could cancel; i.e., relative to LTS magnets, everything would be similar but in “slow motion”. The challenge arises, however, because traditional quench detection is based upon voltage measurements. Voltage, however, is simply the line integral of the electric field between the two voltage taps. The electric field profile is directly correlated with the temperature profile, so a normal zone with a short, highly peaked temperature profile produces the same voltage as a long normal zone with a relatively low peak temperature. The highly peaked temperature profile, however, which is what results from a slow NZPV, is more likely to induce degradation. Thus, either significantly enhanced quench propagation is required, or quench detection requires higher spatial resolution.

Rayleigh scattering

One approach that has been proposed for distributed quench detection is Rayleigh scattering interrogation of an optical fiber that is co-wound with the conductor in the magnet [34]. While a variety of fiber-optic based sensing approaches have been studied for superconducting magnets [35-42], Rayleigh backscattering is the most versatile approach for sensing in HTS magnets because it relies on random fluctuations in the index profile along the optical fiber. Light sent down the fiber encounters these fluctuations, causing Rayleigh scattering. Thus, Rayleigh scattering uses naturally occurring defects present in even the best quality fibers as scattering points. For a given fiber, the scatter amplitude as a function of distance is a random but static property of that fiber and can be modeled as a long, weak Bragg grating with a random period. Thermally induced changes in the local period of the Rayleigh scatter pattern cause changes in the locally reflected spectrum and this spectral shift can be calibrated to form a distributed temperature sensor.

Recent work has confirmed that Rayleigh scattering, with the potential for spatial resolution well below 1 mm, allow fibers to be used as truly distributed sensors in HTS magnets [34]. The high spatial resolution, however, leads to a large amount of data to be analyzed in order to determine the spectral shift from a reference scan, which can lead to insufficient temporal resolution. Additionally, the length of fiber being monitored also increases the data volume, and thus the processing time can consume a large amount of the time quench protection time budget. Thus, an effective quench sensor based on Rayleigh scattering has an essential need for a balance between spatial resolution, temporal resolution, data analysis speed and monitoring length. To balance these needs, it is thus critical to understand the trade-off in spatial and temporal resolution that is required to protect HTS magnets.

Modelling REBCO quench behaviour

To better understand all aspects of the dynamic quench behavior of REBCO conductors and magnets, an experimentally validated, multi-scale, two-dimensional/three-dimensional (2D/3D) model has been developed using the COMSOL platform. This model is able to accurately predict NZPV and MQE of conductors and magnets while also calculating the temperature, voltage and mechanical state of the various layers of materials that comprise the conductor [43-46]. Previously this model has been used to identify conductor variables that can influence quench behaviour [45]. Most recently, it has been used to identify the required spatial and temporal resolutions of a quench detection system for a YBCO coil that had been previously characterized experimentally [46]; this is illustrated in Fig. 7. This plot superimposes the requirements of the magnet for effective quench detection, based upon a minimum propagating zone criterion, with the capabilities of a distributed sensing system (in this example, a Rayleigh scattering system based upon optical backscatter reflectometry is used). Through this approach, the applicability of a sensor technology to a particular magnet can be assessed. Or, alternatively, the protectability of a magnet using a particular quench detection technology can be determined and the magnet redesigned as needed. This approach allows the quench detection system to be a consideration during the design of a magnet system rather than a response to the design.

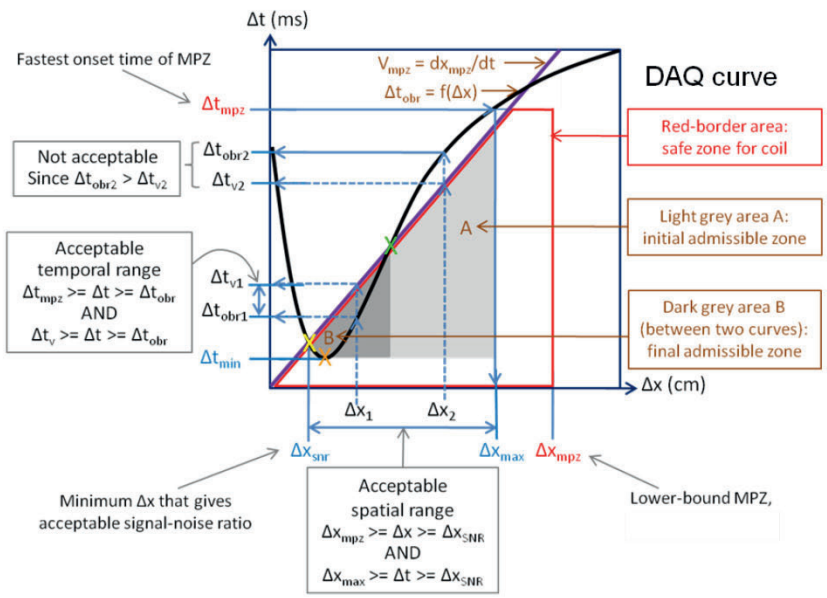

Figure 7: Graphical illustration of the required spatial and temporal resolutions for safe quench detection in a YBCO magnet. Superimposed upon the magnet requirements are the hypothetical capabilities of a Rayleigh-scattering based distributed sensor. The overlap then shows the safe operating range for the magnet with such a detection system. If there is no overlap, then the detection technology would not be applicable to the magnet [34].

THERMALLY-CONDUCTING ELECTRICAL INSULATORS

Traditionally, quench propagation is much faster along the length of the conductor (longitudinal propagation) than from turn-to-turn (transverse propagation) because of the presence of turn-to-turn electrical insulation. An alternative approach to quench protection is to change this paradigm such that transverse propagation contributes significantly to the spreading of the normal zone, increasing the utilization of the available specific heat of the coil and reducing the rate at which the peak temperature increases. Although longitudinal normal zone propagation may be slower, the time budget for detection would be significantly increased.

The effect of thermally-conducting electrical insulator was demonstrated using the 2D/3D model of quench propagation. Fig. 8 shows the temperature versus time and location in YBCO coils insulated with (a) kapton and (b) a thermally conducting electrical insulator. The coil with the thermally conducting electrical insulator has a sixfold increase in MQE, a 50% reduction in peak temperature with a corresponding doubling of the end-to-end coil voltage. Thus, the magnet is more stable due to the accessibility of the specific heat of the entire coil, and a quench is more readily detected due to the higher voltage, while more resilient due to the reduced peak temperature.

While the results shown in Fig. 8 are the result of a computer model, this concept has been recently translated to practice for both Bi2212 and YBCO coils. Using a doped-titania insulation, the NZPV of both Bi2212 and YBCO coils has been increased by 275% [47]. This is illustrated in Fig. 9, which compares the voltage versus time of coils insulated with the doped titania insulation (left) and with traditional insulation (kapton for YBCO, braided mullite for Bi2212). Noting that the horizontal distance between the data represent the time delay for propagation, the effect of the insulation is clear. As this insulation system is improved further, magnets can evolve from linear, one-dimensional normal zones to (ultimately) spherical normal zones that maximize the coils ability to resist degradation.

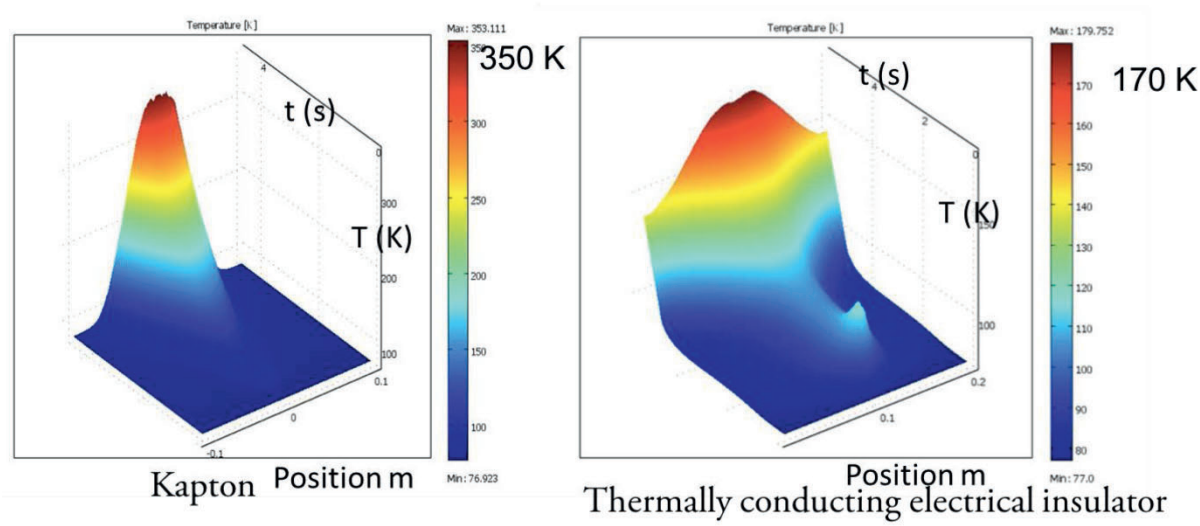

Figure 8: Comparison of the temperature profile of a YBCO magnet with (left) Kapton and (right) a thermally conducting electrical insulator [48].

SUMMARY

The development of high field superconducting magnets using high temperature superconductors has progressed significantly due to advances in Bi2212 and YBCO conductor technologies. Quench propagation in HTS magnets, even at high magnetic fields, is very slow – as much as two orders of magnitude slower than LTS magnets – and thus quench protection remains a key hurdle before such magnets can be safely implemented.

In this paper a number of approaches to improving quench protection in HTS magnets have been summarized. One option is to improve the resilience of the conductors, thereby increasing the time-budget for detection and protection. This is likely to occur through the continuous evolution of Bi2212 conductors, but for REBCO coated conductors, which have very high J_c in the superconducting layer, focusing specifically on the ability of a conductor to withstand a quench may be key.

Another approach is to implement a distributed quench detection sensor, such as an optical fiber monitored using Rayleigh scattering. Such a system has the potential for spatial resolution approaching the wavelength of the interrogating light, but at the expense of rapidly increasing data analysis times and thus a loss of temporal resolution. Understanding the required spatial and temporal resolutions for quench detection thus becomes essential.

Another option is transform quench propagation from being primarily a one-dimensional behavior to being a three-dimensional behavior. This may be achieved through the development of thermally-conducting electrical insulation that greatly reduces the peak temperature of the magnet relative to the coil voltage.

Quench behavior in HTS coils is a complex phenomenon that requires a dynamic understanding of both the conductor at the ~ µm scale and the magnet at the macroscopic scale. To facilitate this, a multi-scale model has been developed in COMSOL that allows complex analysis of REBCO magnets. This model can be effectively implemented to engineer the conductor, the magnet, and to understand the complex quench behavior.

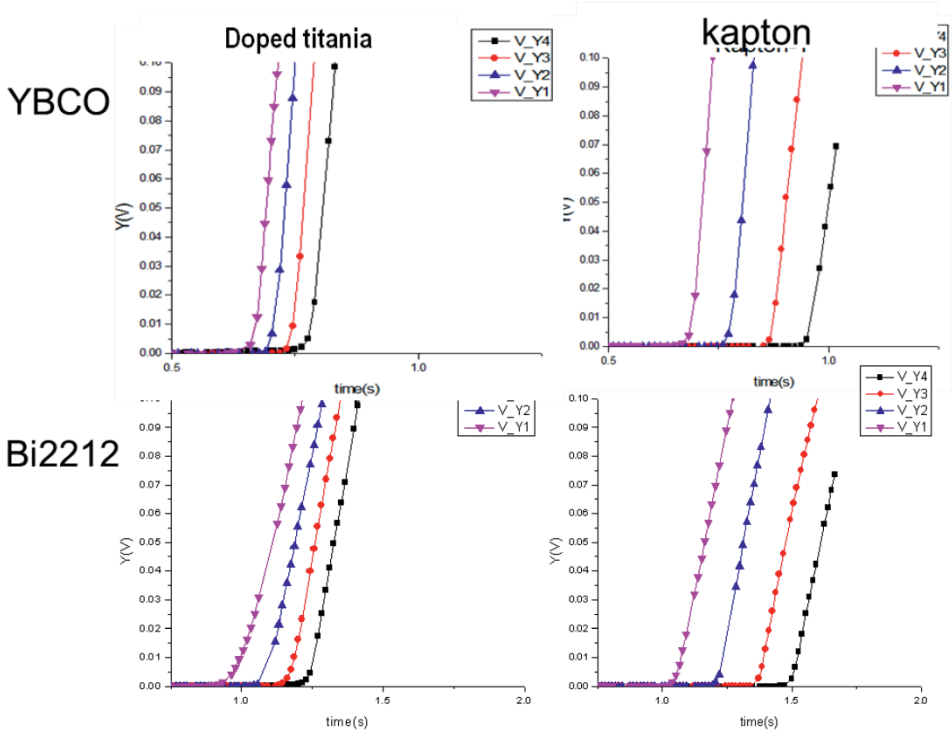

Figure 9: Illustration of the effect of the recently-developed thermally–conducing electrical insulator on quench propagation in YBCO and Bi2212 coils [47].

ACKNOWLEDGMENT

The author is greatly indebted to and appreciative of a number of collaborators and students who have contributed to this work, including Wan Kan Chan, Davide Cruciani, Timothy Effio, Gene Flanagan, Andrew Hunt, Frank Hunte, Sasha Ishmael, Philippe Masson, Makita Phillips, Honghai Song, Ulf Trociewitz, Melanie Turenne, Xiaorong Wang, Marvis White and Liyang Ye.

REFERENCES

[1] J. Schwartz, T. Effio, X. Liu, Q. V. Le, A. L. Mbaruku, H. J. Schneider-Muntau, T. Shen, H. Song, U. P. Trociewitz, X. R. Wang, and H. W. Weijers, High field superconducting solenoids via high temperature superconductors, IEEE Transactions on Applied Superconductivity, vol. 18, pp. 70-81, 2008.

[2] W. T. Nachtrab, C. V. Renaud, T. Wong, X. T. Liu, T. M. Shen, U. P. Trociewitz, and J. Schwartz, Development of high superconductor fraction $Bi_2Sr_2CaCu_2O_x$/Ag wire for MRI, IEEE Transactions on Applied Superconductivity, vol. 18, pp. 1184-1187, 2008.

[3] T. Shen, J. Jiang, A. Yamamoto, U. P. Trociewitz, J. Schwartz, E. E. Hellstrom, and D. C. Larbalestier, Development of high critical current density in multifilamentary round-wire Bi2Sr2CaCu2O8+delta by strong overdoping, Applied Physics Letters, vol. 95, Oct 2009.

[4] T. Shen, J. Jiang, F. Kametani, U. P. Trociewitz, D. C. Larbalestier, J. Schwartz, and E. E. Hellstrom, Filament to filament bridging and its influence on developing high critical current density in multifilamentary Bi2Sr2CaCu2Ox round wires, Superconductor Science & Technology, vol. 23, p. 025009, Feb 2010.

[5] K. R. Marken, H. P. Miao, M. Meinesz, B. Czabaj, and S. Hong, Progress in Bi-2212 wires for high magnetic field applications, IEEE Transactions on

Applied Superconductivity, vol. 16, pp. 992-995, Jun 2006.

[6] H. Miao, K. R. Marken, M. Meinesz, B. Czabaj, and S. Hong, Development of round multifilament Bi-2212/Ag wires for high field magnet applications, IEEE Transactions on Applied Superconductivity, vol. 15, pp. 2554-2557, Jun 2005.

[7] W. T. Nachtrab, X. T. Liu, T. Wong, and J. Schwartz, Effect of Solidification Conditions on Partial Melt Processed Bi2212/Ag Round Wire, IEEE Transactions on Applied Superconductivity, vol. 21, pp. 2795-2799, Jun 2011.

[8] H. W. Weijers, U. P. Trociewitz, K. Marken, M. Meinesz, H. Miao, and J. Schwartz, The generation of 25.05 T using a 5.11 T $Bi_2Sr_2CaCu_2O_x$ superconducting insert magnet, Superconductor Science & Technology, vol. 17, pp. 636-644, Apr 2004.

[9] W. D. Markiewicz, H. W. Weijers, P. D. Noyes, U. P. Trociewitz, K. W. Pickard, W. R. Sheppard, J. J. Jaroszynski, A. Xu, D. C. Larbalestier, and D. W. Hazelton, 33.8 Tesla with a $YBa_2Cu_3O_{7-x}$ superconducting test coil, in Advances in Cryogenic Engineering, Vols 55a and 55b. vol. 1218, J. G. Weisend, J. Barclay, S. Breon, J. Demko, M. DiPirro, J. P. Kelley, P. Kittel, A. Klebaner, J. Marquardt, G. Nellis, T. Peterson, J. Pfotenhauer, S. VanSciver, M. Zagarola, and A. Zeller, Eds., ed, 2010, pp. 225-230.

[10] R. A. Badcock, N. J. Long, M. Mulholland, S. Hellmann, A. Wright, and K. A. Hamilton, Progress in the Manufacture of Long Length YBCO Roebel Cables, IEEE Transactions on Applied Superconductivity, vol. 19, pp. 3244-3247, Jun 2009.

[11] D. C. van der Laan, X. F. Lu, and L. F. Goodrich, Compact $GdBa_2Cu_3O_{7-d}$ coated conductor cables for electric power transmission and magnet applications, Superconductor Science & Technology, vol. 24, Apr 2011.

[12] F. Trillaud, A. Caruso, J. Barrow, B. Trociewitz, U. P. Trociewitz, H. W. Weijers, and J. Schwartz, Normal Zone Generation and Propagation in YBa2Cu3O7-? Coated Conductors Initialized by Localized Pulsed Disturbances, Advances in Cryogenic Engineering Materials, 2004, pp. 852-859.

[13] F. Trillaud, H. Palanki, U. P. Trociewitz, S. H. Thompson, H. W. Weijers, and J. Schwartz, Normal zone propagation experiments on HTS composite conductors, Cryogenics, vol. 43, pp. 271-279, Mar-May 2003.

[14] H. H. Song and J. Schwartz, Stability and Quench Behavior of YBa2Cu3O7-x Coated Conductor at 4.2 K, Self-Field, IEEE Transactions on Applied Superconductivity, vol. 19, pp. 3735-3743, Oct 2009.

[15] C. L. H. Thieme, K. Gagnon, H. Song, and J. Schwartz, Stability of second generation HTS pancake coils at 4.2 K for high heat flux applications, IEEE Transactions on Applied Superconductivity, vol. 19, p. 1626-1632 2009.

[16] H. Song, K. Gagnon, and J. Schwartz, Quench behavior of conduction-cooled $YBa_2Cu_3O_{7-\delta}$ coated-conductor pancake coils stabilized with brass and copper, Superconductor Science & Technology, vol. 23, p. 10, 2010.

[17] X. R. Wang, A. R. Caruso, M. Breschi, G. M. Zhang, U. P. Trociewitz, H. W. Weijers, and J. Schwartz, Normal zone initiation and propagation in Y-Ba-Cu-O coated conductors with Cu stabilizer, IEEE Transactions on Applied Superconductivity, vol. 15, pp. 2586-2589, Jun 2005.

[18] X. Wang, U. P. Trociewitz, and J. Schwartz, Near-adiabatic quench experiments on short $YBa_2Cu_3O_{7-d}$ coated conductors, Journal of Applied Physics, vol. 101, p. 053904, Mar 2007.

[19] X. R. Wang, U. P. Trociewitz, and J. Schwartz, Self-field quench behavior of YBCO coated conductors with different stabilizers, Superconductor Science & Technology, vol. 22, 2009.

[20] X. Wang, U. P. Trociewitz, and J. Schwartz, Critical current degradation of short YBa2Cu3O7-s coated conductor due to an unprotected quench, Superconductor Science & Technology, vol. 24, p. 035006, 2011.

[21] W. S. Kim, F. Trillaud, M. C. Ahn, Y. Iwasa, X. Peng, and M. Tomsic, Normal zone propagation in 2-dimensional YBCO winding pack models, IEEE Transactions on Applied Superconductivity, vol. 18, pp. 1249-1252, June 2008.

[22] L. A. Angurel, E. Martinez, J. Pelegrin, R. Lahoz, G. F. de la Fuente, N. Andres, M. P. Arroyo, Y. Y. Xie, and V. Selvamanickam, Changes in the Thermal Stability of 2G HTS Wires by Local Modification of the Stabilization Layer, IEEE Transactions on Applied Superconductivity, vol. 21, pp. 3017-3020, Jun 2011.

[23] F. Trillaud, M. C. Ahn, J. Bascunan, W. S. Kim, J. P. Voccio, and Y. Iwasa, Quench behavior, quench protection of a YBCO test coil assembly, IEEE Transactions on Applied Superconductivity, vol. 18, pp. 1329-1332, June 2008.

[24] T. Effio, U. P. Trociewitz, X. Wang, and J. Schwartz, Quench induced degradation in $Bi_2Sr_2CaCu_2O_{8+x}$ tape conductors at 4.2 K, Superconductor Science & Technology, vol. 21, Apr 2008.

[25] U. P. Trociewitz, B. Czabaj, S. Hong, Y. Huang, D. C. Knoll, D. C. Larbalestier, W. D. Markiewicz, H. Miao, M. Meinesz, X. Wang, and J. Schwartz, Quench studies on a layer-wound $Bi_2Sr_2CaCu_2Ox$/AgX coil at 4.2 K, Superconductor Science & Technology, vol. 21, Feb 2008.

[26] L. Ye, F. Hunte, and J. Schwartz, Effects of high magnetic field on the low-temperature quench behavior of $Bi_2Sr_2CaCu_2O_x$ coils, Superconductor Science & Technology, vol. 26, p. 055006, 2013.

[27] C. V. Varanasi, J. Burke, H. Wang, J. H. Lee, and P. N. Barnes, Thick $YBa_2Cu_3O_{7-x}$+$BaSnO_3$ films with enhanced critical current density at high magnetic

fields, Applied Physics Letters, vol. 93, p. 3, Sep 2008.

[28] V. Selvamanickam, Y. Chen, X. Xiong, Y. Xie, X. Zhang, A. Rar, M. Martchevskii, R. Schmidt, K. Lenseth, and J. Herrin, Progress in second-generation HTS wire development and manufacturing, Physica C, vol. 468, pp. 1504-1509, 2008.

[29] T. Aytug, M. Paranthaman, K. J. Leonard, K. Kim, A. O. Ijaduola, Y. Zhang, E. Tuncer, J. R. Thompson, and D. K. Christen, Enhanced flux pinning and critical currents in YBa2Cu3O7-delta films by nanoparticle surface decoration: Extension to coated conductor templates, Journal of Applied Physics, vol. 104, p. 6, Aug 2008.

[30] S. H. Wee, A. Goyal, J. Li, Y. L. Zuev, S. Cook, and L. Heatherly, The incorporation of nanoscale columnar defects comprised of self-assembled $BaZrO_3$ nanodots to improve the flux pinning and critical current density of $NdBa_2Cu_3O_{7-d}$ films grown on RABiTS, Superconductor Science & Technology, vol. 20, pp. 789-793, Aug 2007.

[31] L. Ye, D. Cruciani, T. Effio, F. Hunte, and J. Schwartz, On the causes of degradation in $Bi_2Sr_2CaCu_2O_{8+x}$ round wires and coils by quenching at 4.2 K, IEEE Transactions on Applied Superconductivity, submitted 2013.

[32] H. H. Song, F. Hunte, and J. Schwartz, On the role of pre-existing defects and magnetic flux avalanches in the degradation of $YBa_2Cu_3O_{7-x}$ coated conductors by quenching, Acta Materialia, vol. http://dx.doi.org/10.1016/j.actamat.2012.09.003, 2012.

[33] A. Kajbafvala, W. Nachtrab, X. F. Lu, F. Hunte, X. Liu, N. Cheggour, T. Wong, and J. Schwartz, Dispersion-Strengthened Silver Alumina for Sheathing $Bi_2Sr_2CaCu_2O_{8+x}$ Multifilamentary Wire, IEEE Transactions on Applied Superconductivity, vol. 22, pp. 8400210-8400210, 2012.

[34] W. K. Chan, G. Flanagan, and J. Schwartz, Spatial and temporal resolution requirements for quench detection in (RE)Ba2Cu3Ox magnets using Rayleigh-scattering based fiber optics distributed sensing, Superconductor Science & Technology, submitted 2013

[35] F. Hunte, H. Song, J. Schwartz, R. P. Johnson, and M. Turenne, Fiber Bragg Optical Sensors for YBCO Applications, presented at the 2009 Particle Accelerator Conference, Vancouver, Canada, 2009.

[36] M. Turenne, R. P. Johnson, F. Hunte, and J. Schwartz, Multi-Purpose Fiber Optic Sensors for High Temperature Superconductor Magnets, presented at the 2009 Particle Accelerator Conference, Vancouver, Canada, 2009.

[37] S. B. Mahar, Spontaneous Brillouin Scattering Quench Diagnostics for Large Superconducting Magnets, PhD., Department of Nuclear Science & Engineering, Massachusetts Institute of Technology, Cambridge, 2008.

[38] S. Pourrahimi, S. P. Smith, J. H. Schultz, and J. V. Minervini, Performance of the US quench detection systems in the QUELL experiments, IEEE Transactions on Applied Superconductivity, vol. 7, pp. 447-450, 1997.

[39] R. RajiniKumar, K. G. Narayankhedkar, G. Krieg, M. Susser, A. Nyilas, and K. P. Weiss, Fiber Bragg gratings for sensing temperature and stress in superconducting coils, 2006, pp. 1737-1740.

[40] J. H. Schultz, S. Pourrahimi, S. Smith, and P. W. Wang, Principles of advanced quench detection design in cable-in-conduit (CICC) magnets, IEEE Transactions on Applied Superconductivity, vol. 7, pp. 455-460, 1997.

[41] J. M. van Oort and R. M. Scanlan, A fiber-optic strain measurement and quench localization system for use in superconducting accelerator dipole magnets, IEEE Transactions on Applied Superconductivity, vol. 5, pp. 882-885, 1995.

[42] J. M. van Oort and H. H. J. ten Kate, A fiber-optic sensor for strain and stress measurement in superconducting accelerator magnets, IEEE Transactions on Magnetics, vol. 30, pp. 2600-2603, 1994.

[43] W. K. Chan, P. J. Masson, C. Luongo, and J. Schwartz, "Three-dimensional micrometer-scale modeling of quenching in high aspect ratio $YBa_2Cu_3O_{7-\delta}$ coated conductor tapes. Part I: Model development and validation," *IEEE Transactions on Applied Superconductivity,* vol. **20**, pp. 2370-2380, 2010.

[44] W. K. Chan, P. J. Masson, C. A. Luongo, and J. Schwartz, Influence of inter-layer contact resistances on quench propagation in $YBa_2Cu_3O_x$ coated conductors, IEEE Transactions on Applied Superconductivity, vol. 19, p. 2490—2495, 2009.

[45] W. K. Chan and J. Schwartz, Three-Dimensional Micrometer-Scale Modeling of Quenching in High-Aspect-Ratio $YBa_2Cu_3O_{7-d}$ Coated Conductor Tapes-Part II: Influence of Geometric and Material Properties and Implications for Conductor Engineering and Magnet Design, IEEE Transactions on Applied Superconductivity, vol. 21, pp. 3628-3634, Dec 2011.

[46] W. K. Chan and J. Schwartz, A hierarchical, three-dimensional, multiscale electro-magneto-thermal model of quenching in $REBa_2Cu_3O_{7-d}$ coated conductor based coils, IEEE Transactions on Applied Superconductivity, vol. 22, p. 4706010, 2012.

[47] S. Ishmael, H. Lee, M. White, F. Hunte, X. T. Liu, N. Mandazy, J. Muth, G. Naderi, L. Ye, A. Hunt, and J. Schwartz, Enhanced quench propagation in $Bi_2Sr_2CaCu_2O_x$ and $YBa_2Cu_3O_{7-d}$ coils via nanoscale, doped-titania based, thermally-conducting electrical insulator, IEEE Transactions on Applied Superconductivity, 2013 (in press).

[48] P. Masson, 2007.

MODELING HEAT TRANSFER FROM QUENCH PROTECTION HEATERS TO SUPERCONDUCTING CABLES IN NB_3SN MAGNETS

T. Salmi*, D. Arbelaez, S. Caspi, H. Felice, S. Prestemon, LBNL, Berkeley, CA 94720, USA
G. Chlachidze, Fermi National Laboratory, IL, USA
H. H. J. ten Kate, University of Twente, Enschede, the Netherlands

Abstract

We use a recently developed quench protection heater modeling tool for an analysis of heater delays in superconducting high-field Nb_3Sn accelerator magnets. The results suggest that the calculated delays are consistent with experimental data, and show how the heater delay depends on the main heater design parameters.

INTRODUCTION

The quench protection of the present-day high-field Nb_3Sn accelerator magnets is based on resistive protection heaters – typically stainless steel–polyimide laminates on the coil surfaces [1]. They bring large segments of the winding to a resistive state during quench, accelerating the magnet current decay and consequently reducing the hotspot temperature. The goal of the heater design is to provide a short heater delay, i.e. the time delay between heater activation and the heater induced quench, and quench a large fraction of the winding. Physical limitations come from the maximum heater voltage and temperature (typically 400 V and 350 K, respectively). The heater insulation thickness (typically between 0.025 and 0.100 mm) required for electrical integrity has a significant effect on the delay time.

In the magnets under development for the LHC HiLumi upgrade, whose length is of the order of 10 m, the heater delay should be in the order of 10 ms, and the heaters should cover at least 60-100% of the coil surface [2][3]. This has been obtained in shorter and/or lower energy R&D magnets (LARP LQ and HQ) [3], but now the increased coil surface area and also requirements for thicker heater insulation to guarantee electrical integrity (increase from 0.025 mm to 0.050-0.075 mm) bring new challenges. Also, LQ and HQ, which had heaters on both the coils inner and outer surfaces, showed that only the outer surface heaters are mechanically reliable. Therefore, significant optimization of the present technology is needed. An additional complexity comes from the need of heating stations for long magnets, making the geometry of the heater non-uniform along the magnet length and adding an additional degree of freedom to the heater design problem.

This paper summarizes a recently developed numerical modeling tool for simulating heat transfer between the heater and coil. The model accounts for the heater geometry and powering, the cable properties, magnetic field and the various insulation materials allowing the evaluation of the heater delay in different conditions. The model is first applied to the LARP HQ magnet [4]. First, the real heater geometry is simulated and the delays are compared with experimental data from [5]. Second, a parametric analysis is used to examine the impact of main heater design parameters on the quench delay. The model is then applied to simulate the protection heaters in the so-called 11 T dipole prototype, built within a CERN and FNAL joint R&D program [6], and the simulated delays are compared with experimental data. Understanding of the impact of the heater design on the quench delay is important for designing the protection for future magnets.

COMPUTATIONAL MODEL

Thermal model

The heat transfer between the heater and the cable is simulated using a numerical two-dimensional heat conduction model, with joule heat generation in the stainless steel component to simulate heater powering. In this approximation the heat propagation between neighboring turns is neglected. At the present stage of development, current sharing between the strands and quench propagation due to Joule heating in the cable is also not simulated.

The two-dimensional heat equation describing the thermal propagation is

$$\gamma_m c_{p,m} \frac{\partial T}{\partial t} = \frac{\partial}{\partial y}\left(k_m \frac{\partial T}{\partial y}\right) + \frac{\partial}{\partial z}\left(k_m \frac{\partial T}{\partial z}\right) + \mathrm{f_{gen,ss}}\,, \qquad (1)$$

where $T = T(z,y,t)$ is temperature (K), $c_{p,m} = c_{p,m}(T,B)$ is specific heat (J/K/kg), γ_m is mass density (kg/m^3), $k_m = k_m(T,B)$ is thermal conductivity (W/K/m) of the material m at the location (z, y) at time t (s) and $f_{gen,ss} = f_{gen,ss}(t,T)$ is the internal volumetric heat source applied only in stainless steel component. (W/m^3). It is defined using

$$f_{gen,ss}\,(t,T) = \rho_{ss}(T) J_{ss}^2(t), \qquad (2)$$

where $J_{ss}(t)$ is the heater current density (A/m^2) and $\rho_{ss}(T)$ is the stainless steel electrical resistivity (Ωm), or using

$$f_{gen,ss}\,(t) = P_{PH}(0)/d_{ss} e^{-\frac{2t}{\tau}}, \qquad (3)$$

where $P_{PH}(0)$ (W/m^2) is the heater adiabatic peak power defined by dividing the heater power by the heating surface area [1], d_{ss} (m) is the stainless steel thickness, and τ is a time constant of an exponential heater current decay.

*T. Salmi is now with Tampere University of Technology, Tampere, Finland.

A heater on the coil straight section typically has a periodical geometry (see Fig. 1). Due to the symmetry, each turn can be represented by modeling only half of the heater period, when adiabatic boundary conditions are assumed at the center and at the end of the period ($z = 0$, and at $z = PH\ period/2$). Figure 2 shows a case with one heating segment at the center of the heater period. The boundaries at the top and bottom of the system, i.e. at $y = 0$, or at $y = H$, are at fixed temperature, T_{bath}.

Material properties and magnetic field

The various insulation layers as well as the cable and heater dimensions are taken into account using regions of different material properties. The different layers are assumed in perfect thermal contact. The layers dimensions and materials are an input parameter.

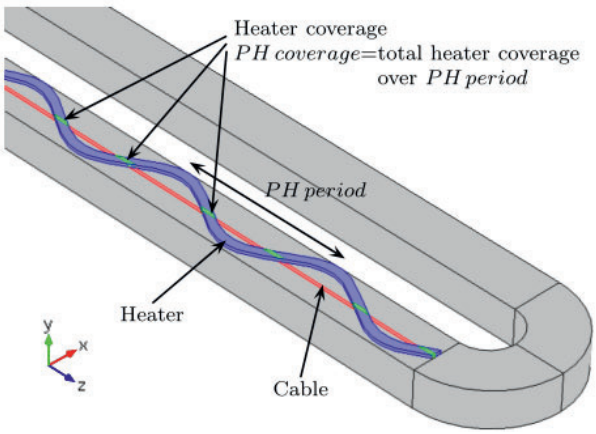

Figure 1: A schematic view showing how generic heater geometry can be expressed in terms of periodical heater coverage at different turns.

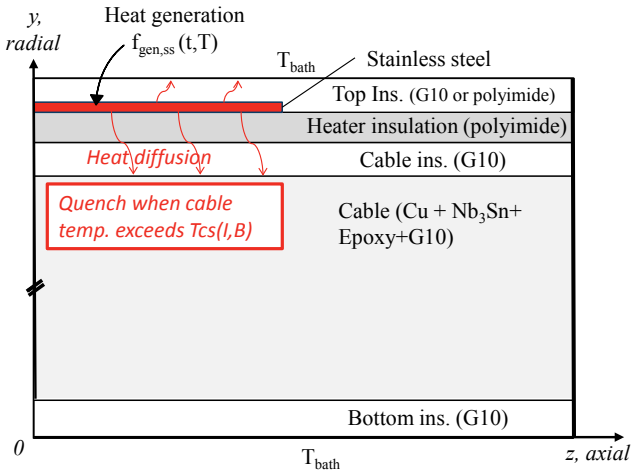

Figure 2: Thermal model for half period of the protection heater geometry, representing the longitudinal and radial (through wide side of the cable) thermal transport in one coil turn.

The material thermal properties are functions of local temperature and magnetic field. The copper properties and epoxy specific heat are from [7] (with linear extrapolation to 0 J/kg/K at 0 K for epoxy specific heat below 4.4 K), Nb_3Sn specific heat is a fit from [8], G10, polyimide (Kapton) and stainless steel properties are from [9] (with extrapolation for Kapton thermal conductivity below 4.3 K [8], and stainless steel specific heat below 5 K [10]). The stainless steel resistivity is based on [11].

The cable is a homogeneous block with properties averaged over its constituents (copper, Nb_3Sn, epoxy and/or G10) volume. Thermal conductivities of Nb_3Sn and epoxy are assumed negligible relative to that of copper. By default, the magnetic field in the cable cross-section is uniform, and it is an input parameter. The model allows also simulating variable field profile across the cable. In that case the current sharing temperature, T_{cs}, varies at different cable location, and the material thermal properties are based on the average field.

Quench delay determination

The simulation begins with the powering of the heaters and the quench delay is defined once the cable temperature exceeds $T_{cs}(B,I)$, i.e. the temperature at which the current in the cable is equal to the (temperature and magnetic field dependent) critical current. The model offers two possibilities for fitting the critical surface, Godeke [12] [13] and Summers [14].

Numerical solution

The numerical solution is based on the thermal network method [15] with explicit finite difference discretization scheme [16] and adaptive time stepping. Several elements in each layer are needed to guarantee numerical stability and accuracy. The segments size is an input parameter.
The correct implementation of the equations was verified by comparison with analytical solution of a case in 1-D heat conduction in an insulated slab with steady surface heat flux and constant and uniform material properties.

SIMULATION OF THE HQ HEATER IN THE HQ01 QUADRUPOLE

As the first study case, the model is applied to the LARP HQ magnet, which is a 1-m-long 120-mm-aperture quadrupole based on cosθ geometry with two layers [4]. The outer layer heater implemented in the coils is modeled, and the simulated heater delays are compared with experimental data from the HQ01e tests [5]. Then, the impact of individual heater design parameters on the quench delay is examined using a parametric analysis. The used coil parameters are shown in Table 1, and the field map in Fig. 3. In the next sections the used parameters for both studies are detailed.

Simulation of the HQ heater geometry

The HQ outer layer heater has a wavy shape, providing partial coverage at several turns. One period of the geometry is shown in Fig. 4. It shows that the heater coverage increases from about 2 cm to 7 cm in approximately 1 cm steps in turns 2nd to 7th (counted from the outer layer (OL) pole).

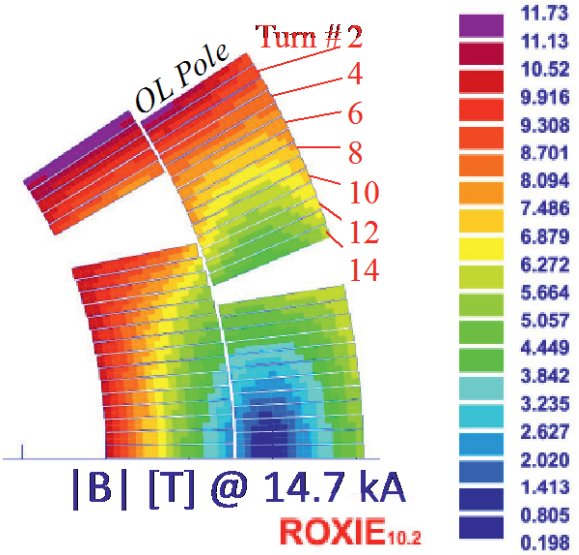

Figure 3: HQ01 field map and notation of the turn count from outer layer pole.

Table 1: Simulation parameters for the LARP HQ simulation

Parameter	HQ01 (Coil 9)
SSL@ 1.9 K (kA)	19.31
SSL @ 4.4 K (kA)	17.52
B_{peak}, at I [18]	$0.00127\times I^{0.9505}$
#strands	35
Copper RRR	190
Strand Cu/SC	1.05
Cable voids	12% epoxy
Cable width (mm)	15.00
Cable ins. (mm)	0.090 (G10)
Bottom ins. (mm)	0.708 (G10)
Top ins. (mm)	0.30 (G10)
Stainless steel (mm)	0.025
PH ins. Kapton (mm)	0.0254
Strip path (mm)	2220.0
Strip width (mm)	11.0

After the 7th turn, the continuous heater coverage is smaller than 7 cm. As the heater coverage increases while moving away from the pole, the magnetic field decreases (Fig. 3). Higher field and longer coverage are assumed to compete in reducing the delay, so the location of the first heater-induced quench is not obvious. In the experiment the first quench can be located between turns 2 and 14 based on voltage tap signals, but it is not known in more detail. Here it is assumed to occur in one of the turns from 2nd to 7th and the heater delay is simulated at each of these turns. The shortest quench delay among the modelled turns is chosen for the comparison with experimental data.

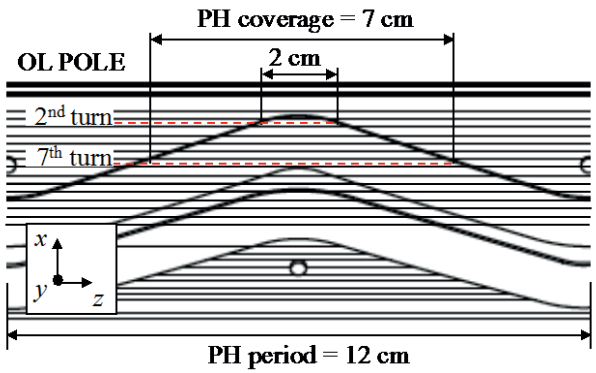

Figure 4: One period of the HQ01 heater on the coil outer surface. The *PH coverage* (the length of the cable continuously covered by the heater at each turn) in one *PH period* (periodical heater geometry) is shown for the 2nd and 7th turn.

The magnetic field strength is calculated at the coil outer surface (using Cobham Vector field Opera-2D [17]), which is the location closest to the protection heater and this value is used for the whole turn. The fields in turns from 2nd to 7th normalized to the magnet peak field at a given current are respectively 0.75, 0.74, 0.72, 0.70, 0.69 and 0.66.

The Nb_3Sn critical surface is calculated using Godeke fit with parameters from HQ coil 9 extracted strand measurements [18]. The calculated T_{cs} varies from 14.2 to 14.4 K at 5 kA and from 9.6 to 10.4 K at 14 kA. The heater power is defined by 230 V over the 2220 mm long strip, giving J_{ss} = 210 A/mm^2, which gives a heater power $P_{PH}(0)$ about 50 W/cm^2 The current decays according to a time constant of 40 ms (defined from the measured current decay profile).

Parametric study

In the parametric study, we modeled the outer layer 2nd turn at 1.9 K, and magnet current 80% of the short sample limit (15400 A). The computed conductor field is 9.1 T, and T_{cs} is 8.9 K.

The varied parameters are the heater power, the Kapton thickness, and the heater coverage. If not otherwise mentioned, in the parametric analysis the heater power P_{PH} is 50 W/cm^2 and constant (step function), the heater covers the whole turn, and the Kapton thickness is 0.025 mm.

HQ01 SIMULATION RESULTS

Comparison with experimental data

The HQ heater simulation at different turns shows that the delays increase from about 5 to 40 ms when decreasing the magnet current from 80% of short sample limit to 20% (see Fig. 5). The case with infinite heater coverage (1D), at magnet peak field (B/B_{peak} = 1.0) is also shown, and as expected, the delays converge to that when increasing heater coverage or field fraction. The variation

between the turns is larger at lower current and the turn that quenches first depends on the current.

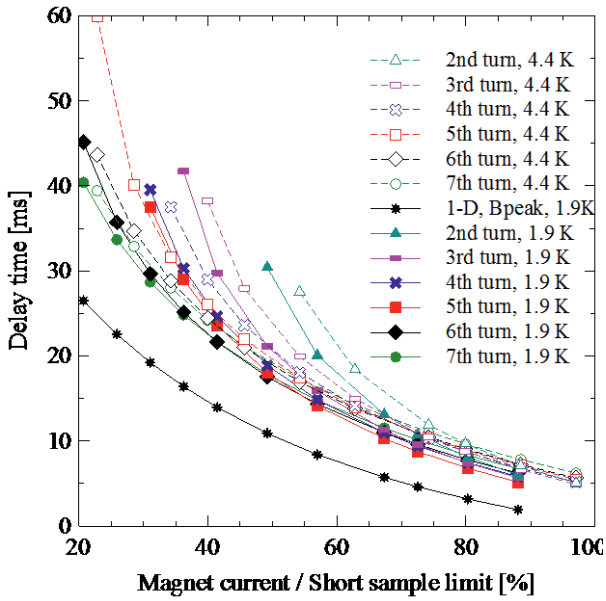

Figure 5: HQ heater delays simulated at several outer layer coil turns. The solid lines represent operation at 1.9 K and dashed lines at 4.4 K.

The simulation agrees with experimental data within 20%, as shown in Fig. 6, where the shortest delays at each current are plotted together with the experimental data. The impact of the operation temperature on the delays is only a few percent in both the simulation and experiment. Excluding the longest simulated delay times (where the heat diffusion away from the hotspot plays a larger role), this difference is approximately proportional to the difference in the energy margins to quench (i.e., integration of the cable heat capacity from T_{bath} to T_{cs}) at each current.

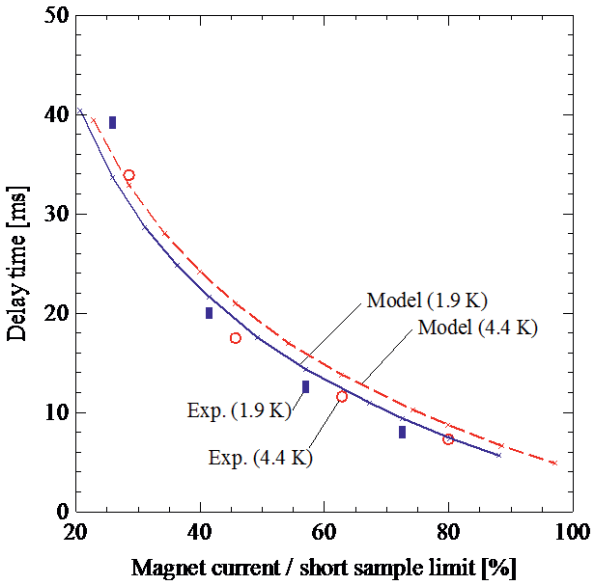

Figure 6: Modeled and experimental (Exp.) HQ heater delays at 1.9 and 4.4 K versus normalized magnet current.

Heater delay vs. heater power

As expected, larger heater power reduces the simulated delays, as shown in Fig. 7. Saturation is visible around 30 W/cm^2. Increasing the power further has only a small effect on the delay. The curve shape is consistent with experiments [1].

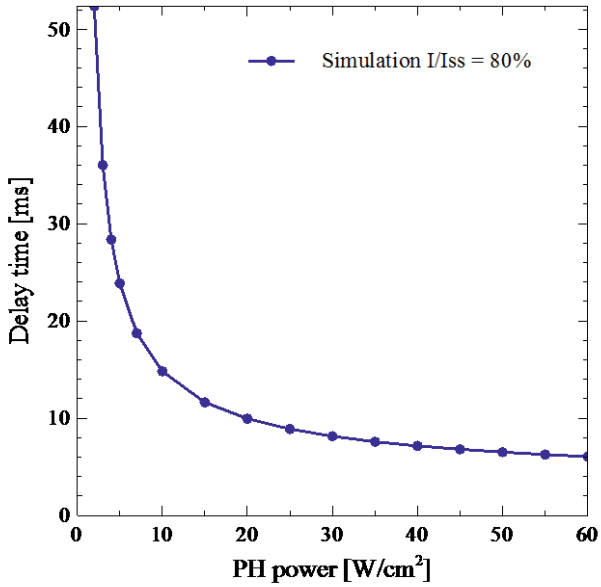

Figure 7: Heater delay time vs. heater peak power. The heater power is a step function in time.

Delay time vs. insulation thickness

The increase in the simulated delay when increasing the polyimide thickness is shown in Fig. 8. The delay approximately doubles when the thickness is increased from 0.025 mm to 0.076 mm. Comparison of experimental data from HQ01e (0.025 mm Kapton), and from HQ coil 15 (0.076 mm Kapton), which was tested in the HQM04 mirror structure, shows an increase in the experimental delay approximately 130%, in agreement with the simulated value.

Delay time vs. heater geometry

The simulation shows that longer heater coverage leads to shorter delays – up to saturation around 20 mm, when the delay approaches 7 ms indicating a local 1-D heat transfer (fully covered cable) (see Fig. 9). At coverage of 5 mm, the delay is more than doubled. Variation of the period between 50 and 180 mm changed the result less than 5% with respect to the reference case with 120 mm long period.

Longer delay for the same short sample fraction was also found in the LARP LQ magnet, which had shorter heater coverage than HQ [3].

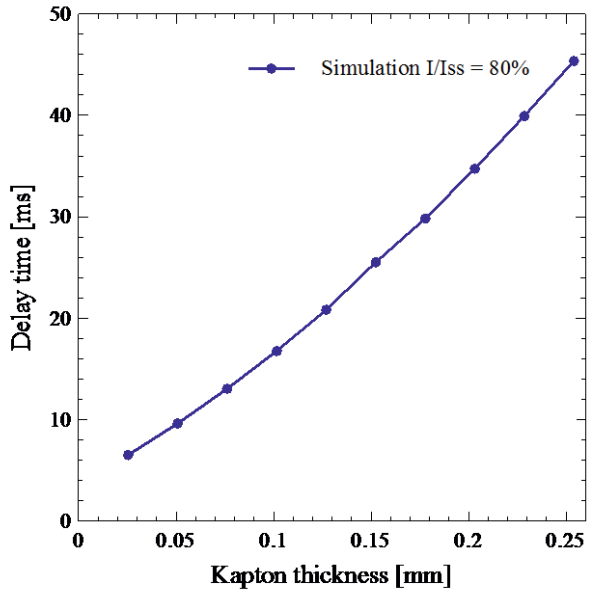

Figure 8: Heater delay vs. Kapton thickness.

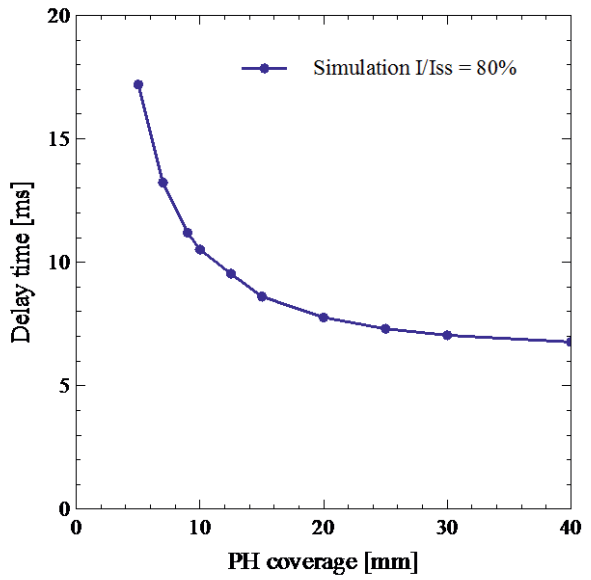

Figure 9: Heater delay time vs. length of the covered cable segment.

SIMULATION OF THE HEATER IN THE 11 T DIPOLE

Contrary to HQ, the heater strips in the 2-m long so-called 11 T dipole model (MBHSP01) are straight strips parallel to the magnet axis. Therefore the problem is essentially in 1-D, when the heat transfer between the coil turns is neglected.

The heaters have been tested with Kapton thickness of 0.076 mm and 0.203 mm, i.e. much larger than HQ. Therefore the simulation of the 11 T dipole heaters allows applying the model to a quite different regime. The adhesive (0.038 mm) that is used to glue the stainless steel heater to the Kapton has been neglected in the simulation. The 11 T dipole magnet development and test are described in [6] and the protection heater experiments in [19].

Heater power

On the outer surface of each coil half, two straight heater strips form a U-shape and are connected in series (see Fig. 10 [19]). The strip closer to the central pole piece (high field region) is 26 mm wide, and the strip closer to the magnetic midplane (low field region) is 21 mm wide. Two U-shapes are connected in parallel and powered by a capacitor discharge in one Heater Firing Unit (HFU). The capacitance is 9.6 mF and the measured cold resistance of the circuit is 2.6 Ω, giving RC-time constant of 25 ms.

The calculated heater current is 77 A for a voltage of 400 V. Using equation (1) and multiplying by the stainless steel thickness we get a peak power of about 17 W/cm^2 in the high field heater and 27 W/cm^2 in the low field heater, using the stainless steel 304 resistivity (490 nΩm @ 4.2 K) . The calculated resistance of both heaters together is 3.4 Ω. However, the measured resistance of the U-shaped heater is 20% larger, 4.2 Ω. Partial explanation is that the heaters in the 11 T dipole are based on stainless steel 316 L, which has about 5% higher electrical resistivity. Assuming that the measurement gives the correct resistivity (and for example the connection in between the strips or irregularities in the heater shape do not impact), the heater power is 20 W/cm^2 in the high field heater, and 31 W/cm^2 in the low field heater. In the simulation we use the average of these: 18.5 W/cm^2 in the high field and 29 W/cm^2 in the low field region.

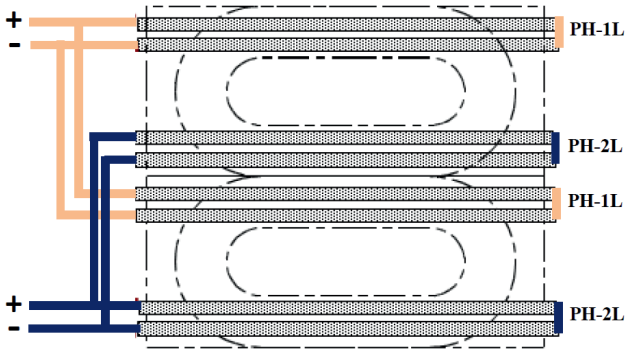

Figure 10: 11 T dipole heater connection scheme. PH-1L and PH-2L refer to heater inslualtion thickness with 1 or 2 layers of Kapton [19].

Magnetic field and cable properties

Under each heater, the first quench is expected to initiate at the coil turn that has the highest magnetic field. The high field and low field heater were considered separately, and the delay was simulated in the turns #2 and #19 from the outer layer pole (see Fig. 11 [20]).

The choice of field value for the turn #2 is not straight forward because the field on the coil outer diameter (OD) is only 78% of the maximum field of that conductor (see Fig. 10). We therefore considered three cases. In Case 1, field was taken at the coil outer surface (65% of the magnet peak field). In Case 2, field was taken as the maximum field in the conductor (82% of the magnet peak field). And, in Case 3, the field profile varies across the conductor (1-D projection of the 2-D field map in the cable cross-section). In the turn #19, the field at the coil surface is the same as the cable maximum field (42% of the magnet peak field), so simulations were done only for this field value.

The HQ simulation corresponds to the Case 2. The field location in the 11 T simulation is more critical for two reasons: First, in HQ the cable outermost field was 87-95% of the maximum field. Second, in 11 T the expected delays are longer due to smaller heater power and thicker insulation between the heater and cable. The longer delays increase the impact of all factors, including the field. One should keep in mind that while tuning the field location may be useful for finding the best expectation for the experimental results, it may give a false sense of accuracy because the anisotropic cable internal structure (strands' paths) is still not modelled.

The critical surface is based on the Summers fit, using B_{c20} = 24.8 T, T_{c0} = 16.5 K, C = 9.08×10^3. Other simulation parameters are summarized in Table 2.

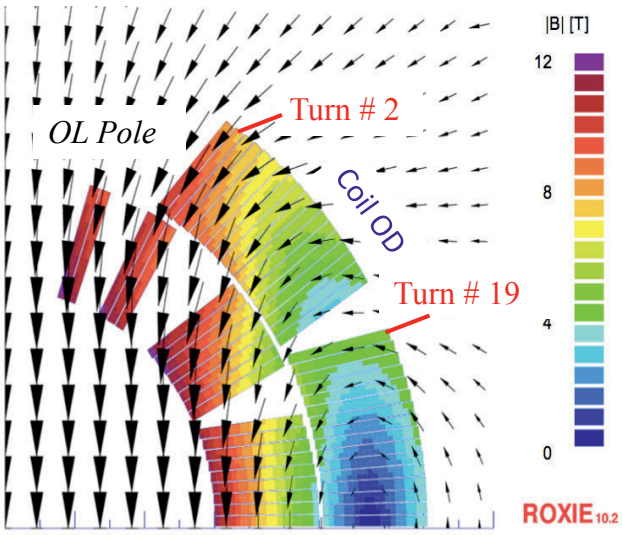

Figure 11: 11 T dipole field map [20].

Table 2. Simulation parameters for CERN-FNAL 11 T dipole simulation

Parameter	11 T
SSL@ 1.9 K (kA)	15.4
SSL @ 4.4 K (kA)	13.8
B_{peak}, at I [18]	$0.0023\times I^{0.9062}$
#strands	40
Copper RRR	100
Strand Cu/SC	1.13
Cable voids	6.5% epoxy, 6.5% G10
Cable width (mm)	14.88
Cable ins. (mm)	0.200* (G10)
Bottom ins. (mm)	0.706 (G10)
Top ins. (mm)	0.64 (Kapton)
Stainless steel (mm)	0.025
PH ins. Kapton (mm)	0.076 / 0.203
Strip path (mm)	2100.0
Strip width (mm)	26.1

* This refers to the insulation between the bare cable and the polyimide of the PH insulation. In the 11 T magnet 0.2 mm includes a 0.1 mm glass sheet that is impregnated on the coil surface.

11 T DIPOLE SIMULATION RESULTS

The heater delays were measured between 40 and 60% of SSL. Simulations in general show a good agreement with results, giving (i) much longer delays for thicker polyimide and (ii) the correct slope of delay increase at lower currents. At 80% of SSL at 1.9 K the heater delay is expected to be about 55 ms with 0.203 mm Kapton, and 25 ms with 0.076 mm Kapton. The 20% predicted increase in the simulated delays from 1.9 to 4.5 K is not seen in the experiment.

The simulated delays at 1.9 K agree the best with the experimental data for the high field heater when the utilized field was the maximum in the cable (Case 2). The agreement is within 20% for both thicknesses when above 50% of SSL at 1.9 K. The delays using the realistic field profile (Case 3) are about 10-30% longer than the delays with the maximum field. When the field is taken at the coil OD (Case 1), the delay is at least 60% longer than with the maximum field. The delays under the low field heater were about 50-150% longer than the shortest delays under the high field heater. Figures 12 and 13 show the results in the Cases 2 (Bmax) and 3 (Bprof) of the high field heater.

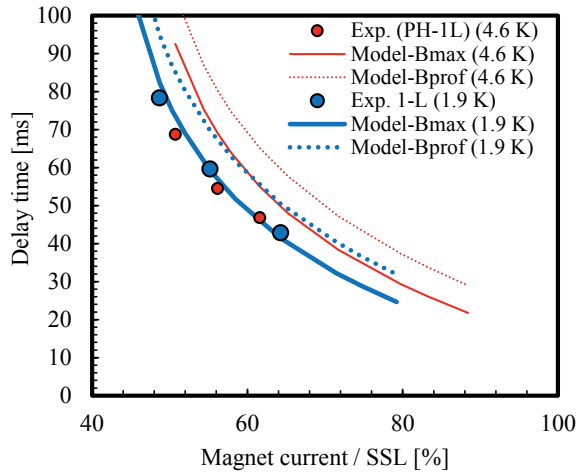

Figure 12: Heater delays in the 11 T dipole, simulated and measured, for the 0.076 mm Kapton thickness.

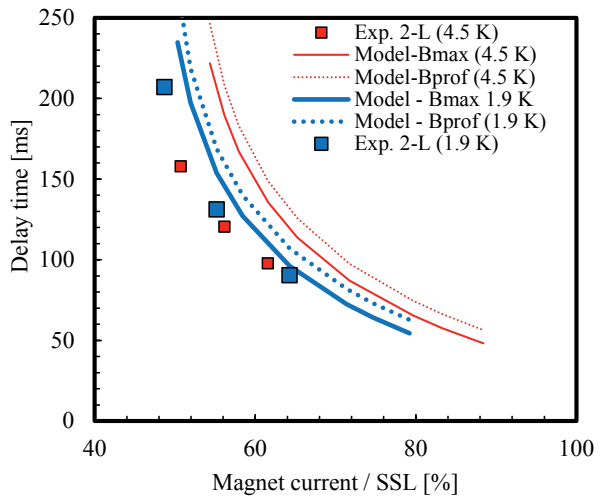

Figure 13: Heater delays in the 11 T dipole, simulated and measured, for the 0.203 mm Kapton thickness.

CONCLUSION

A computational tool based on a two-dimensional heat conduction model is developed to calculate the protection heater delay time to induce a quench as a function of a large amount of parameters, which include cable properties, magnet operation conditions, and heater geometry, powering and insulation scheme.

The modeling tool is applied to simulate heater delays in the LARP Nb_3Sn quadrupole magnet called HQ01e and in the FNAL-CERN Nb_3Sn dipole magnet called 11 T. The agreement between the simulation, which does not use any free parameters, and experimental data is within 20% in most cases. A parametric analysis using the HQ01e data showed the heater delay dependence on heater power, polyimide thickness and heater geometry.

This relatively simple modeling approach can be useful in understanding the effect of various parameters on the quench delay time, which is important for optimizing the heater design for future high-field Nb_3Sn accelerator magnets.

ACKNOWLEDGMENT

This work has been supported by the U. S. Department of Energy, under Contract No. DE-AC02-05CH11231. Finalizing this paper was supported by Stability Analysis of Superconducting Hybrid magnets (Academy of Finland, #250652). The authors wish to thank Hugo Bajas and Jerome Feuvrier (CERN) for the heater delay measurements in HQ01e. We thank Fred Nobrega (FNAL), Bernhard Auchmann (CERN) and Emanuela Barzi (FNAL) for providing information for the 11 T simulation. I also gratefully acknowledge the support and useful advice on the work from Ezio Todesco (CERN) and Antti Stenvall (Tampere University of Technology), who also provided Figure 1. I have also received helpful input from Maxim Marchevsky, and Matthijs Mentink (LBNL). I also thank Ray Hafalia (LBNL) for grammar corrections in an earlier draft of the paper (the new mistakes in the present version are not his fault).

REFERENCES

[1] H. Felice et al., Instrumentation and Quench Protection for LARP Nb_3Sn Magnets, IEEE Trans Appl Supercond vol.19, no.3, pp. 2458-2462, June 2009.

[2] L. Imbasciati, Studies of Quench Protection in Nb_3Sn Superconducting Magnets for Future Particle Accelerators, PhD thesis and Fermilab TD-03-028, 2003.

[3] T. Salmi et al., Quench Protection Challenges in Long Nb_3Sn Accelerator Magnets, Trans. of the Cryogenic Engineering Conference, Vol 57, pp. 656-663, June 2011.

[4] H. Felice et al., Design of HQ - A High Field Large Bore Nb_3Sn Quadrupole Magnet for LARP, IEEE Trans Appl Supercond vol.19, no.3, pp. 1235–1239, 2009.

[5] H. Bajas et al., Test Results of the LARP. HQ01 Nb_3Sn Quadrupole Magnet at 1.9 K, presented at ASC2012.

[6] A. V. Zlobin et al., Development and Test of a Single Aperture 11 T Nb_3Sn Demonstrator Dipole for LHC Upgrades, IEEE Trans Appl Supercond vol. 23, no 3, p 4000904, 2013.

[7] CRYOCOMP(©copyright Eckels Engineering Inc.).

[8] G. Manfreda, Review of ROXIE's Material Database for Quench Simulations, CERN internal note 2011-24, EDMS Nr: 1178007.

[9] E.D. Marquardt et al., Cryogenic Material Properties Database, in Proc. 11th Int. Cryocooler Conf., Keystone, 2000, available at: http://cryogenics.nist.gov/ MPropsMAY/material%20properties.htm.

[10] A. Davies, Material properties data for heat transfer modeling in Nb3Sn magnets. Available at:

http://www.illinoisacceleratorinstitute.org/2011%20Program/student_papers/Andrew_Davies.pdf.
[11] S. Prestemon (LBNL), private communication.
[12] A. Godeke et al., General Scaling Relation for the Critical Current Density in Nb_3Sn, Supercond. Sci. Technol 2006, 19.
[13] D. Arbelaez et al., An Improved Model for the Strain Dependence of the Superconducting Properties of Nb_3Sn, Supercond. Sci. Technol 2009, 22.
[14] L. T. Summers, et al. A model for the prediction of Nb_3Sn critical current as a function of field, temperature, strain and radiation damage, IEEE Trans. Magnetics, 27,1.
[15] Y. Çengel, Heat Transfer A Practical Approach, McGraw-Hill Education, 2003.
[16] T. Blomberg, Heat Conduction in Two and Three Dimensions: Computer Modelling of Building Physics Applications, PhD Thesis, Lund University, Department of Building Physics, Sweden, 1996.
[17] Opera 2D, website: http://www.cobham.com/about-cobham/aerospace-and-security/about-us/antenna-systems/specialist-technical-services-and-software/products-and-services/design-simulation-software/opera/opera-2d/static-electromagnetics.aspx.
[18] A. Godeke et al., A Review of Conductor Performance for the LARP High-Gradient Quadrupole Magnets, to be published in SUST.
[19] G. Chlachidze et al., Quench Protection Study of Single-Aperture Nb3Sn Demonstrator Dipole for LHC Upgrades, IEEE Trans on Appl Supercond vol. 23 no 3, 2013.
[20] B. Auchmann (CERN), private communication.

ACOUSTIC DETECTION IN SUPERCONDUCTING MAGNETS FOR PERFORMANCE CHARACTERIZATION AND DIAGNOSTICS

M. Marchevsky, X. Wang, G. Sabbi and S. Prestemon, LBNL, Berkeley CA, 94720, USA

Abstract

Quench diagnostics in superconducting accelerator magnets is essential for understanding performance limitations and improving magnet design. Applicability of the conventional quench diagnostics methods such as voltage taps or quench antennas is limited for long magnets or complex winding geometries, and alternative approaches are desirable. Here, we discuss acoustic sensing technique for detecting mechanical vibrations in superconducting magnets. Using LARP high-field Nb_3Sn quadrupole HQ01 [1], we show how acoustic data is connected with voltage instabilities measured simultaneously in the magnet windings during provoked extractions and current ramps to quench. Instrumentation and data analysis techniques for acoustic sensing are reviewed.

INTRODUCTION

Acoustic sensing of mechanical events in solids has a long history and has also been used in the past to access quench locations in superconducting magnets [2-9]. The advantages of this method are its non-intrusiveness, absence of sensitivity to magnetic field and use of inexpensive sensors that are easily adaptable to various magnet configurations. Sound propagation velocity of several km/s is typically faster than the quench propagation velocity; it allows for the mechanical detection to be accomplished on a millisecond time scale that is comparable (or faster) to other techniques. Furthermore, using acoustic sensor arrays, sound sources can be localized through triangulation with centimetre accuracy, and selectivity for different kinds of events can be achieved through post-processing and analysis in time and frequency domain.

Interpretation of the acoustic data is nevertheless a challenging problem. This is because sound in magnets can be generated by different mechanisms, most notably:

- sudden mechanical motion of a cable portion or coil part;
- cracking and/or fracture of epoxy;
- flux jump, as current re-distribution in the cable leads to the sudden local variation of the electromagnetic force;
- quench development, as formation of a hot spot leads to the quick thermal expansion and corresponding local stress build-up.

A common feature of all these sound-generating events is that they are usually associated with well-localized sources. Sound waves propagate radially from such source and eventually get reflected by the material boundaries, converted into resonant vibrational modes of the structure and into heat. Structural vibrations are of special importance for interpreting the sound signals, as various transverse (sound), longitudinal (bending) and more complex torsional modes can be excited by a single intrinsic mechanical event or just by the ambient background noise (helium boiling, cryostat vibrations, etc.); those resonances may then "ring" for a significant period of time (100-300 ms) due to relatively high (~100) mechanical quality factor of a typical magnet structure. The most interesting frequency range is the one associated with local vibration of a small component (cable, strand), and it is usually well above the range of structural mechanical resonances. Using high-pass filtering and post-processing one can therefore select the signal portion representative of a particular event and establish its precise origin and timing.

INSTRUMENTATION

We have developed a system for acoustic sensing based on piezoelectric (PZT) transducers, cryogenic amplifiers and synchronous DAQ system. It was first tested using a room temperature arrangement and later used during the test of the LARP HQ01e magnet [1].

Acoustic sensors and data acquisition

Piezoelectric transducers are widely used for acoustic sensing. In superconducting magnets, they are robust and sensitive to small structural vibrations: sensitivity to events as small as 0.2 μJ has been reported in [8]. In our system, we use disks of SM118 type piezoelectric ceramic, polarized across thickness with dimensions 10 mm outer diameter, 5 mm inner diameter, 2 mm thickness, and self-resonance frequency of (154 ± 4) kHz. (Fig. 1, left). Ring shape of the PZTs allowed for an easy installation on the magnet using a single set screw. In order to improve signal-to-noise ratio and eliminate need for using coaxial lines, we have combined our transducers with custom-built cryogenic amplifiers based on GaAs MOSFET and operating in the temperature range of 1.9-300 K; room-temperature gain of the amplifiers is ~ 3-5.

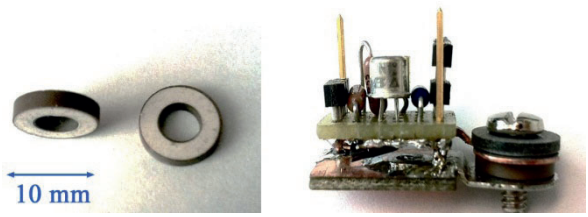

Figure 1: PZT transducers (left) and the cryogenic amplifier - PZT sensor assembly (right).

Each amplifier was interfaced to the room-temperature electronics using a twisted pair of wires and also battery-

powered through that pair. The transducer-amplifier assembly is shown in Fig.1 (right). Fast DAQ (Yokogawa 7000) with simultaneous 1 MHz sampling was used to acquire data. LabView-based software was developed to perform signal frequency analysis and localize the sound source based on acoustic signal timing. Correct operation of the amplified piezo-sensors at 4.2 K was verified using a cryogenic insert to the transport helium dewar.

Room temperature test

Two sensor assemblies were installed on the HQ coil "endshoes", as shown in Fig. 2; distance between the sensors is l_c = 0.96 m. Sounds were excited by slight knocking on the coil using a small metal key. By timing the difference between signal onsets, the sound velocity in the coil was measured as v_s = (4.2 ± 0.1) km/s and the locations x_k of the "knocks" were determined as

$$x_k = 0.5 \cdot \left(l_c + v_s \Delta t_{AB}\right)$$

within ~ 50 mm accuracy.

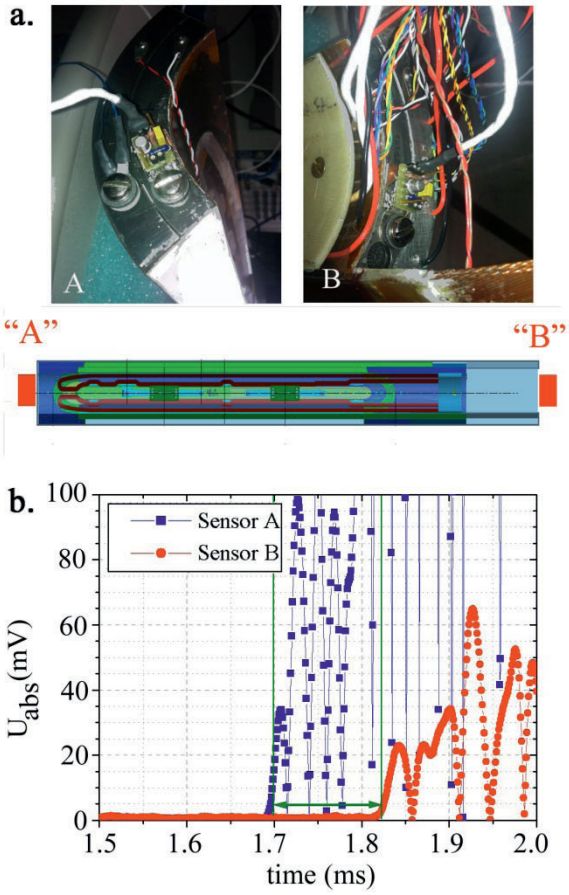

Figure 2: (a) Experimental arrangement for the room temperature test. Two PZT sensors ("A" and "B") were attached to the coil endshoes. (b) Typical signals measured upon slight "knocking" on the coil. Time difference Δt_{AB} = 0.13 ms between the signal onsets (marked with an arrow) corresponds to the sound source location at 27 cm towards the sensor "A" from the center of the coil.

EXPERIMENTAL RESULTS

Installation on the magnet

After the successful test at room temperature, two sensors were installed at the LARP HQ01 quadrupole Nb_3Sn magnet [9] and tested at cryogenic temperature during magnet operation. The locations were chosen at the opposite sides of the magnet; one sensor was bolted to the magnet load plate and another one to the magnet shell; see Fig. 3.

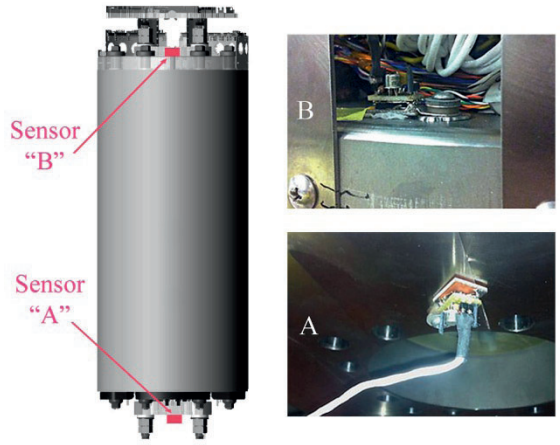

Figure 3: (left) HQ01e3 magnet on the stand with acoustic sensor locations marked with arrows. (right) amplified piezo-sensors bolted to the magnet shells (top) and the loadplate (bottom).

Typical mechanical resonance spectra of the magnet measured on the support stand using same technique as in the coil-on-the-table experiment reveals numerous peaks in the range of 0.3-10 kHz; associated with various compression, bending and torsional self-resonances of the magnet structure. Result for the power spectrum of the shell and load plate sensors are shown in Fig. 4.

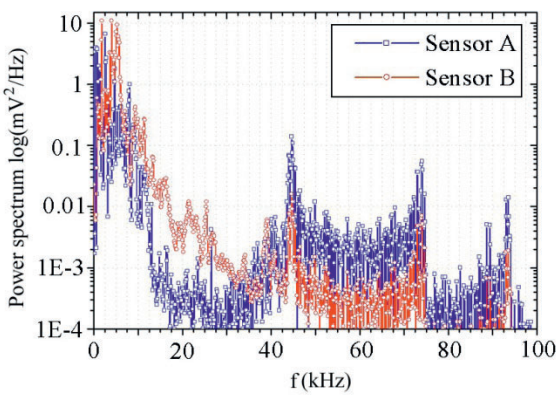

Figure 4: Power spectra of acoustic vibrations in the HQ01e3 magnet, measured in response to the mechanical excitation ("knocking") on the shell. Above ~10 kHz the resonant peaks are strongly suppressed in amplitude compared to those in the low-frequency range.

Note, that the spectra contain no significant peaks above 10 kHz. When the magnet shell was excited, strong signals were measured with both transducers. However,

when the magnet interior (load-plates, rods) were excited, the response of the shell-mounted sensor "B" was much smaller compared to the sensor "A" response. This is indicative of the fact that mechanical vibrations in the coil structure remain fairly uncoupled of the shell excitations, which may be favorable for improved detections of the acoustic signals originating in the coils.

Provoked extractions

Upon cooling down, the magnet current was ramped up to 5.5 kA and a provoked extraction was triggered. Acoustic signals were recorded during the current ramp. First, we observed a significant noise associated with the current extraction. Acoustic waveforms obtained with the 5.5 kA provoked extraction are shown in Fig. 5. Clearly, the magnet is a good mechanical resonator with a quality factor Q~100, as the extraction-triggered "ringing" continues for nearly 1 s; this is ~4 times longer than the time constant of the magnet current transient. The spectral characteristics of the observed acoustic signals are similar to those seen with the room-temperature measurements, indicative of the "global" mechanical excitation of the entire magnet structure with the changing Lorentz force; no significant high-frequency sounds potentially indicative of the vibrating small parts were detected.

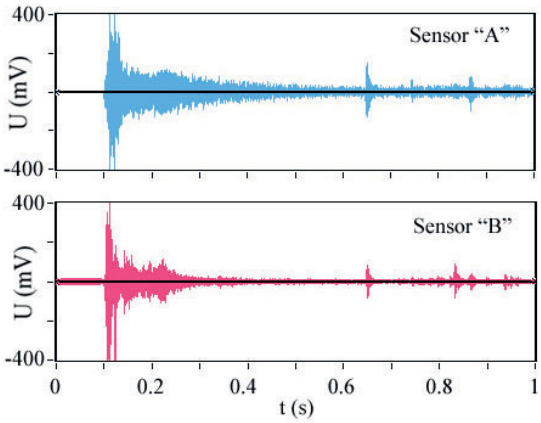

Figure 5: Sound emission waveforms resulting from the provoked extraction of the magnet current at 5.5 kA.

Ramps to quench

In the following, the magnet current was

- ramped up at 75 A/s to 9 kA, current was held steady for 3 min and then ramped back down to zero;
- ramped up at 75 A/s to a spontaneous quench, that occurred at 10.87 kA.

In all these experiments, voltage imbalance (formed by subtracting voltage of two halves of the magnet, usually employed to detect quenches) was recorded simultaneously with the acoustic signals. Data recording rate was 1 MHz and the time window width is 0.2 s. Acquisitions were triggered whenever *either* imbalance or sound was detected to exceed a threshold level; for acoustic signal the threshold was chosen at 5 mV and for the imbalance at 75 mV.

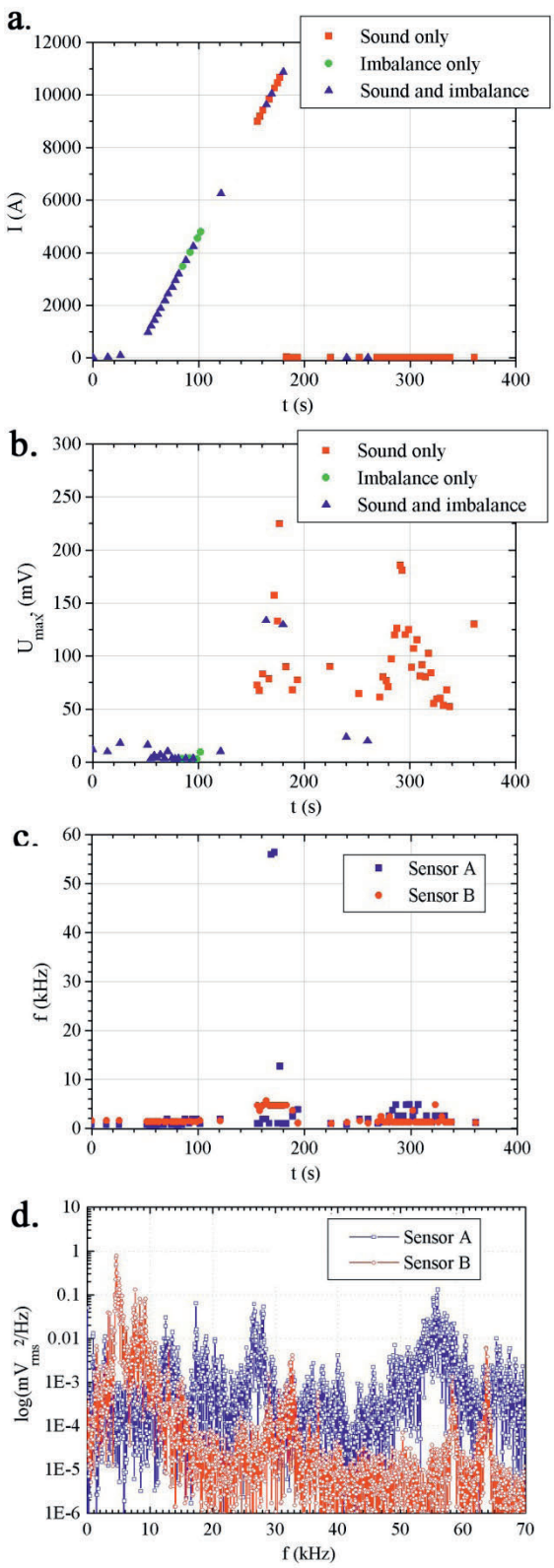

Figure 6: Summary of events triggered by either sound emissions or imbalance variations during the 75 A/s ramp to quench at 10870 A; each point represents a single acquisition cycle of 0.2 s. Time dependence of current (a), maximal sound amplitude (b) and maximal detected sound frequency (c) are shown. (d) Acoustic spectra corresponding to the highest magnet current (~10800 A).

Results of the spontaneous quench ramp are shown in Fig. 6. Four possible types of events were identified:

Below 5 kA:

- Imbalance variation without any associated sound;
- Imbalance variation associated with weak sound signals.

At 8.5 kA and above:

- Stronger sounds with no association with imbalance variations.

Around 10-10.5 kA:

- Stronger sounds associated with imbalance "spikes".

The low-current imbalance variations are known to be caused by flux jumps in the superconducting cable and have been observed in the earlier tests of HQ [1].

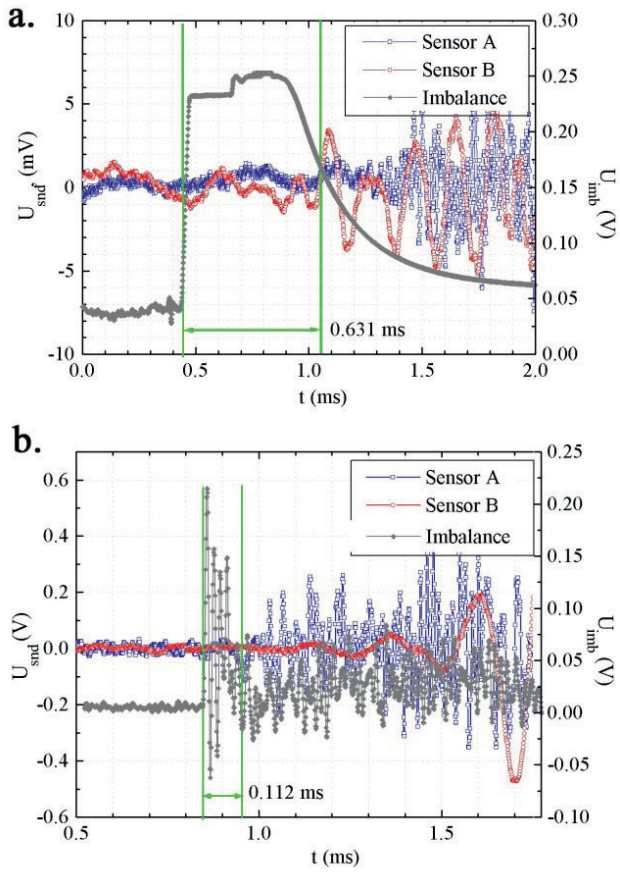

Figure 7: Simultaneously acquired imbalance and acoustic signals at magnet currents of 2440 A (a) and 10036 A (b). In (a) the 0.63 ms delay between the imbalance onset and the sound would place the sound source ~2.6 m away from the "A" transducer, which would be outside of the magnet. In (b) the 0.11 ms delay corresponds to ~0.46 m distance, hence sound is produced within the magnet length.

Our measurements show that the weak acoustic emissions are associated with at least some of these events; this result is consistent with the earlier studies [4, 5].

What is most interesting, however, is that the much stronger sounds are recorded at higher currents where flux jumps are absent. Moreover, these stronger sounds are also associated with much higher frequencies (40-60 kHz) than those observed in provoked extraction experiments. In Fig. 6 (d) the power spectrum of the acoustic signal of sensor "A" (attached to the loadplate) shows an absolute peak at ~56 kHz that becomes prominent only at magnet currents above ~ 9 kA. Same high-frequency sound was detected in other 75 A/s current ramps to 9 kA and back, but without quenching.

To understand origin of the observed acoustic emissions, we have attempted to determine sound source locations for various triggered event, at low and high currents. In Fig. 7 two results of noise source localization are shown for the magnet current of 2440 A (plot a) and 10036 A (plot b) respectively. It turns out, that, based on the signal timing, the sound source in (a) would be located outside the magnet. Such result suggests that in reality, there could be a delay between the flux jump onset (seen as imbalance variation) and the sound generation. On the other hand, in (b) the sound is produced within the magnet length and also the imbalance exhibits multiple fast fluctuations simultaneously with the sound. This observation seems most consistent with the mechanical event [8], such as stick-slip motion of the superconducting cable or supporting structure that is responsible for both sound and the imbalance "spike".

CONCLUSIONS

Amplified piezo-sensors, in combination with fast data acquisition and processing techniques show good potential for real-time characterization of various mechanical events in superconducting magnets during ramping, quench and recovery. We have shown that acoustic signals generated by flux jumps and mechanical motion events in the superconducting accelerator magnet have distinctly different features. HQ magnet exhibits occasional weak acoustic emissions correlated with the flux jumps below 5 kA as well as the larger amplitude high-frequency (>50 kHz) emissions unrelated to flux jumps and only seen above 9 kA. The sounds recorded at high current are occasionally correlated with the short spikes in the magnet electrical imbalance and multiple fast fluctuations most likely caused by stick-slip motion of the conductor.

Further development of the acoustic technique is needed, focusing on improving sensitivity and selectivity to small signals, developing instrumentation and software for precise localization of the sound sources and quantifying energy release in the detected acoustical events. We also plan to access feasibility of the full-scale acoustic quench detection and diagnostic system in the upcoming magnet tests.

ACKNOWLEDGMENT

Technical assistance from P. K. Roy, M. Turqueti, T. Lipton and R. Albright is gratefully acknowledged.

This work is supported by supported by the Director, Office of Science, High Energy Physics, U.S. Department of Energy under contract No. DE-AC02-05CH11231.

REFERENCES

[1] M. Marchevsky, G. Ambrosio, B. Bingham, R. Bossert, S. Caspi, D. W. Cheng, G. Chlachidze, D. Dietderich, J. DiMarco, H. Felice, P. Ferracin, A. Ghosh, A. R. Hafalia, J. Joseph, J. Lizarazo, G. Sabbi, J. Schmalzle, P. Wanderer, X. Wang, A. V. Zlobin, Test of HQ01, a 120 mm Bore LARP Quadrupole for the LHC Upgrade, IEEE Trans. Appl. Supercond. 22, 4702005 (2012), and ref. therein.

[2] P.P. Gillis, Dislocation motion and acoustic emission, ASTM STP 505, 20-29, 1972.

[3] G. Pasztor and C. Schmidt, Dynamic stress effects in technical superconductors and the "training" problem of superconducting magnets, J. Appl. Phys. 49, 886 (1978).

[4] H. Brechna and P. Turowski, Training and degradation phenomena in superconducting magnets, Proc. 6th Intl. Conf. Magnet Tech. (MT6) (ALFA, Bratislava, Czechoslovakia) 597, (1978).

[5] G. Pasztor and C. Schmidt, Acoustic emission from NbTi superconductors during flux jump, Cryogenics 19, 608 (1979).

[6] O. Tsukamoto and Y. Iwasa, Sources of acoustic emission in superconducting magnets**,** J. Appl. Phys. 54, 997 (1983).

[7] M. Pappe, Discussion on acoustic emission of a superconducting solenoid, IEEE Trans. on Magn., 19, 1086 (1983).

[8] O.O. Ige, A.D. Mclnturf and Y. Iwasa, Acoustic emission monitoring results from a Fermi dipole, Cryogenics 26, 131, (1986).

[9] Y. Iwasa, Mechanical disturbances in superconducting magnets-a review, IEEE Trans. on Magn., 28, 113 (1992).

MAXIMUM ALLOWABLE TEMPERATURE DURING QUENCH IN NB_3SN ACCELERATOR MAGNETS

G. Ambrosio, Fermilab, Batavia, IL 60510, USA

Abstract

This note aims at understanding the maximum allowable temperature at the hot spot during a quench in Nb_3Sn accelerator magnets, through the analysis of experimental results previously presented.

INTRODUCTION

Nb_3Sn accelerator magnets under development for possible use in the Large Hadron Collider [1,2] may reach, during a quench, higher hot spot temperatures than presently-used Nb-Ti accelerator magnets. This is due both to the higher critical current density in the non-copper section and to the lower copper-non-copper ratio in Nb_3Sn strands than in Nb-Ti strands, together with their different cooling properties. Therefore, understanding the maximum allowable hot spot temperature in Nb_3Sn accelerator magnets has primary importance in the design of these magnets and their protection systems.

In this report this question is addressed through the analysis of tests previously performed on a quadrupole, on a small racetrack, and on some cable samples made with internal tin Nb_3Sn strands.

HIGH TEMPERATURE TESTS ON A NB_3SN QUADRUPOLE

The quadrupole which was the subject of the test discussed here is TQS01: the first Technological Quadrupole with shell structure assembled by LARP [3]. This 1-m-long, 90-mm-aperture magnet was assembled and cold tested three times. At the end of the last test (TQS01c) [4], performed at Fermilab in 2007, high hot spot temperatures were reached in order to evaluate their impact on the magnet's performance. This experiment was performed at 4.6 K bath temperature and the magnet was operating at about 80% of the short sample limit when the experiment started. TQS01c used a Modified Jelly Roll (MJR) conductor manufactured by Oxford Superconducting Technology (OST) with 47% copper. Since TQS01c had no operating spot heaters at the time of this test, spontaneous quenches were used. All spontaneous quenches during this experiment occurred in the same segment (very likely in the same location) in the pole turn of the inner layer of a single coil.

High hot spot temperatures were reached by increasing the delays of dump resistor and protection heaters before the High Temperature (HT) quenches (diamond and triangular markers in Figs. 1 and 2). Increased hot spot temperatures could be reached by increasing these delays. During the experiment some standard quenches (square markers in Figs. 1 and 2) were performed in order to access magnet performance reproducibility and possible detraining effects.

Figure 1 shows that the test started with current ramps to quench at 250 A/s (diamond markers), after which no degradation was found (first four square markers). Subsequently the ramp rate was decreased to 20 A/s in order to reach higher currents and temperatures. Then after five HT quenches (triangular markers) with negligible effects, the 6th HT quench caused an increase of the quench current by 3.3%. The subsequent HT quench caused a detraining of 7.2% with respect to the quench current previously reached. The detraining was recovered after one standard quench, and the subsequent standard quenches confirmed the gain achieved after the 6th HT quench. The 8th HT quench caused a small detraining after which the magnet reached the highest quench current during the entire experiment (4% higher than the quench current plateau before starting the HT experiment). In the subsequent HT quenches at higher and higher temperatures TQS01c showed more and more degradation. Standard quenches showed some permanent degradation after the 14th and 15th HT quenches. At the end of the experiment the permanent degradation was about 25% with respect to the quench current at the beginning of the experiment.

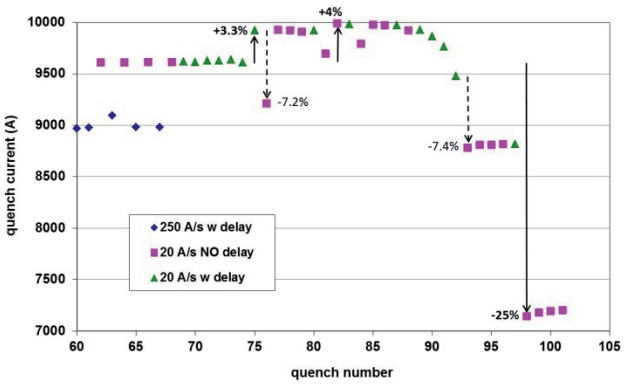

Figure 1: Quench history during high hot spot temperature experiment performed at the end of TQS01c test. Triangular markers show high temperature quenches with long protection delays. Square markers show standard quenches.

The hot spot temperature could not be measured because of the lack of dedicated instrumentation. Therefore the temperature was computed from the measured values of the quench integral (integral of current squared vs. time from the quench start). The code QuenchPro [5] was used to do this computation under the following assumptions:

- Adiabatic approximation.
- The following components were taken into account in the computation of the peak temperature from the

quench integral: the metals in the Rutherford cable, the epoxy within the cable, and the cable insulation (0.1 mm thick assuming some compression after heat treatment). The resulting material fractions are: Nb_3Sn = 23.7%; Cu = 31.5%; bronze = 11.7%; G10 = 33.2%.

- In QuenchPro the copper properties depend on the temperature and on the Residual Resistivity Ratio (RRR), whereas the field is assumed to be constant. In this analysis the cable peak field was used.
- The RRR was measured during magnet test, but the RRR of the quenching segment was not available. Therefore the analysis was performed for the max and min RRR values (170-130) of the quenching coil. The impact of this uncertainty is +/- 6 K with respect to the values shown in Fig. 2.

The results of the hot spot temperature computation are shown in Fig. 2. This is the same quench history plot shown in Fig. 1 with the hot spot temperature reached in most HT quenches. The temperatures (in K) shown on the plot were computed using the average RRR of the quenching coil.

Figure 2 shows that: i) quenches with temperature in the hot spot (T_{HS}) around 340 K caused very small quench current changes; ii) quenches with 370 K < T_{HS} < 400 K caused reversible current changes of a few per cent; iii) quenches with T_{HS} > 460 K caused irreversible degradation.

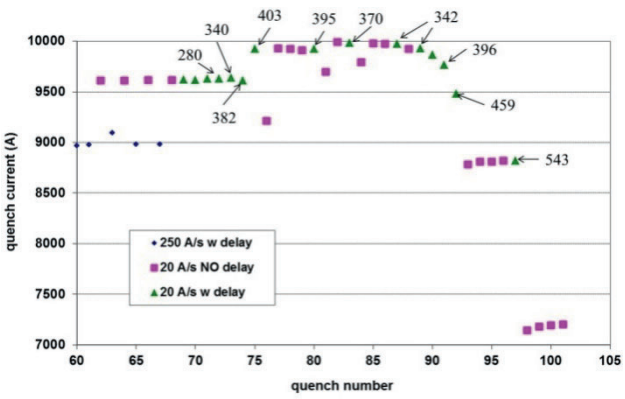

Figure 2: Quench history during high hot spot temperature experiment performed at the end of TQS01c test. The numbers show the peak temperature (in K) reached at the hot spot in some HT quenches.

TESTS PERFORMED ON A NB_3SN SMALL RACETRACK AND CABLE SAMPLES

A useful set of test results and analysis is presented in [6]. High temperature quenches were performed on cables at the NHMFL and on a small racetrack magnet at LBNL. The cables were made of 0.7 mm-diameter ITER-type strands manufactured by IGC Advanced Superconductors with 59% copper fraction. Two samples (Cable 2-a and 2-b) had bending strain induced after reaction; the other sample (Cable 1) did not have any bending strain. The small racetrack (SM05) was made of two coils. The coil used for the high-temperature quenches was instrumented with a spot heater and voltage taps close to the spot heater. This coil was made of MJR strands manufactured by OST with 0.67 mm diameter and 60% copper fraction.

The test results are presented in Fig. 3 (from Ref. [6]). The horizontal axis shows the peak temperature reached in each HT quench. The vertical axis shows the reduced current (quench current divided by maximum current) reached in the standard ramp to quench following each HT quench. Therefore each point shows the degradation vs. hot spot temperature. All cables and the racetrack magnet were instrumented with spot heaters for initiating the quench and with voltage taps around the hot spot area. The resistance growth measured by these voltage taps was used to compute the peak temperature, providing a precise although indirect measurement. A comparison between these measurements and computations using the quench integral is presented in the following section.

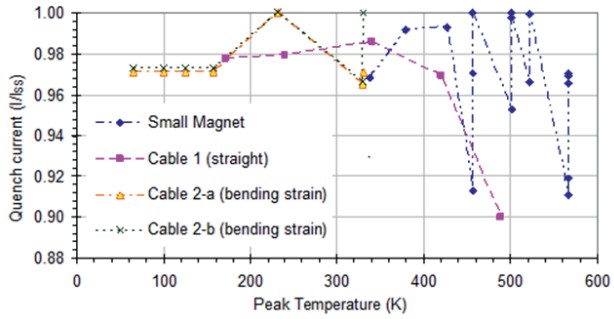

Figure 3: Summary of quench experiments: reduced current vs. peak temperature reached during the preceding HT quench test. The lines represent the temporary sequence of the high temperature events (from Ref [6]).

The plot in Fig. 3 shows negligible degradation up to 420 K. At higher temperatures the small racetrack started detraining and retraining between 90% and 100% of the short sample limit and reached about 570 K with a degradation of only 3%. The cable sample 1, after a HT quench at ~480 K, showed a degradation of 8% together with an insulation failure that irreversibly damaged the sample. This failure demonstrates that the maximum allowable temperature does not depend only on critical current degradation, but also on insulation integrity.

Ref. [6] also presents an interesting comparison between simulations and experimental data collected during a series of cable quench tests. Figure 4 shows different computations of the Quench Integral (QI): (i) using only the metals in the Rutherford cable; (ii) adding the epoxy included in the cable envelope; and (iii) adding also the cable insulation (0.1 mm thick fiberglass tape cured with ceramic binder [7] - resulting in 0.15 mm thickness - and impregnated with epoxy) that was simulated using G10 material properties. Figure 4 also

shows the experimental values of the quench integral (square markers with internal cross) in different quenches. The experimental temperature was measured by the resistance growth of the short segment under the spot heater.

It can be seen that when the peak temperature was about 140 K, the QI computed using metal and epoxy was in good agreement with the experimental value. At higher peak temperatures the experimental values approached the QI computed using also the cable insulation. In the 300-400 K range the QI computed including the cable insulation provided the best agreement with the experimental values. Nonetheless it should be noted that including the cable insulation did not provide a conservative estimate in this temperature range.

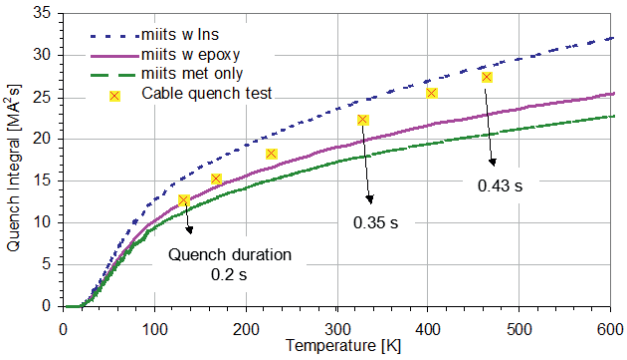

Figure 4: Quench integral of a cable sample vs. temperature: experimental results (square markers) and values computed with different assumptions (dashed line: metals only; continuous line: metals and epoxy inside the cable envelope; dotted line: metals, epoxy and cable insulation). Plot from Ref [6].

ANALYSIS AND CONCLUSIONS

The set of experimental results presented above suggests some preliminary conclusions, which should be confirmed by further tests.

When the hot spot of a Nb_3Sn accelerator magnet exceeds room temperature, there are two threshold temperatures above which magnet performance may change. We start this analysis by naming these thresholds T_1 and T_2 and describing the possible effects when the hot spot temperature (T_{HS}) exceeds them.

If $T_{HS} > T_1$, then the magnet enters an "active territory" with the following features:

- The magnet may experience further training: i.e. a magnet whose training was completed by reaching a current plateau may actually exceed that current plateau in quenches following a high-temperature quench.
- The magnet may experience detraining: i.e. a reduction of the quench current after a high-temperature quench, which can be recovered with a few training quenches.

If $T_{HS} > T_2$, then the magnet enters a "degradation territory" with the following features:

- The magnet may experience irreversible degradation.
- The magnet may experience insulation degradation with possible failure under stress conditions, for instance during subsequent quenches even at lower hot spot temperatures.

Based on this characterization, the "active territory" appears to be associated with small changes of strain in the conductor (within the reversible region) and small changes of stress in the epoxy, which may cause further training or detraining. The "degradation territory" appears to be associated with larger change of strain in the conductor (above the irreversibility limit) and with large deformations of the epoxy, which may also cause cracks or other degradations of the insulation.

The experimental results presented in Fig. 3 suggest that T_1 is around 400 K (disregarding the results of the samples with bending strain, which may have been affected by the special strain condition). The results presented in Fig. 2 (TQS01c) suggest that T_1 is between 340 and 370 K, but this estimate may have a large error because the Fig. 2 temperatures were computed whereas the temperatures in Fig. 3 were measured. Estimating the error of the temperatures in Fig. 2 requires a significant effort because it should address both the error due to the material properties used in the computation as well as the error due to each assumption. Figure 4 suggests a different approach. The computed values (dotted line) and the measured values (square markers with a cross) can be used to evaluate the error when the temperature is estimated by taking into account the cable insulation in the quench integral. This comparison shows that the hot spot temperature (T_{HS}) would have been underestimated by about 30 K when close to 400 K. The cable insulation used in TQS01c was made of the same materials (fiberglass with ceramic binder impregnated with CTD-101K epoxy) used for the insulation of the cable with test results presented in Fig. 4. The same material properties were used to compute the quench integral used in Fig. 4 (dotted line) and to compute the temperatures in Fig. 2. Therefore we may assume that a similar error should affect both of them. If we apply this correction to the estimate of T_1 based on Fig. 2 we obtain: 370 K < T_1 < 400 K (with an error that should be no larger than the correction applied, i.e. +/- 30 K).

The quadrupole magnet (TQS01) and the cables with test results presented in Figures 1 to 4 were impregnated using CTD-101K epoxy made by Composite Technology Development (CTD). The small racetrack magnet was impregnated with CTD-101A epoxy made by the same vendor. The glass transition temperature (T_g) of CTD-101K is 386 K (113 °C) [8-9]. CTD-101A has thermal and structural properties very similar to those of CTD-101K (for instance its T_g is 388 K) [10]. Above the glass transition temperature the epoxy is in a rubber-like state, which may explain the features previously described when T_{HS} is higher than T_1 (active territory). During the high-temperature quenches the hot spot reached temperatures significantly higher than the rest of the coil

or cables. The thermal expansion of the hot spot area was larger than the expansion in the rest of the coil or cables, causing significant thermo-mechanical stresses. When the hot spot exceeded T_g, the epoxy became soft and susceptible to deformation under the thermo-mechanical stresses. When the temperature decreased below T_g, the epoxy returned to its hard state in the new dimensional configuration. For instance, if the hot spot in TQS01c was on the thin edge of a cable in the inner layer, some epoxy could be "extruded" toward the aperture. Signs of this behaviour can be seen in the cross section of the TQS01c quenching coil at the position where all high-temperature quenches initiated [3]. The analysis of TQS01c strain gauges [3] showed a reduction of azimuthal preload in the quenching coil during the high-temperature quenches, confirming that the high-temperature quenches caused epoxy softening and redistribution.

The features associated with the "active territory" can be explained by the redistribution of the epoxy around the hot spot, which may cause a change of strain in the conductor and a change of stress in the epoxy. If T_{HS} slightly exceeds T_g, then the epoxy above T_g is limited to a small volume and the possible change of conductor strain remains very likely within the reversible region. If T_{HS} exceeds T_g by a large amount, than the epoxy volume above T_g can be large causing significant changes of conductor strain and possibly irreversible degradation. This analysis suggests that T_2, the threshold for the "degradation territory", should be higher than T_1. Nonetheless, if the magnet insulation scheme is not sufficiently robust, the thermo-mechanical stresses during a quench (even at moderate hot spot temperatures) could degrade the insulation and lead to electrical failures. Therefore, the insulation scheme of any Nb_3Sn accelerator magnet should be designed to withstand the thermo-mechanical stresses (both within coils and coil-to-structure) well above the glass transition temperature of the epoxy (or other material) used for coil impregnation. By doing so the magnet designers assure that T_2 is higher than T_1. Since we have demonstrated that $T_1 = T_g$, the glass transition temperature of the epoxy can be used to set the maximum allowable temperature (T_{max}) at the magnet hot spot. In order to have some margin T_{max} should be lower than T_g. Since we have seen that in a well-designed magnet T_g is not the edge of a cliff, then a 20% margin is sufficient. The margin can be as low as 10% when conservative approximations are used for computing the hot spot temperature, and the error is smaller than the margin.

Therefore, for the design of Nb_3Sn accelerator magnets using CTD-101K epoxy (with T_g = 386 K), we suggest setting the maximum allowable temperature in the hot spot at 350 K or lower. This temperature appears to be consistent with the test results presented in this note and with many tests performed on Nb_3Sn R&D magnets around the world [11].

Finally, it should be noted that none of the magnets and cable samples discussed in this note had a cored cable. The possible impact of a metallic core inside the cable on the maximum allowable temperature during quench should be addressed by a series of dedicated experiments.

ACKNOWLEDGMENT

Several people contributed to the work presented in this note. Special thanks to Linda Imbasciati, Shlomo Caspi, Guram Chlachidize, Dan Dietderich, Helene Felice and Ezio Todesco.

REFERENCES

[1] L. Bottura, et al., Advanced Accelerator Magnets for Upgrading the LHC, IEEE Trans. on Applied Superc., vol. 22, no.3, June 2012.

[2] E. Todesco, et al., Design Studies for the Low-Beta Quedrupoles for the LHC Luminosity Upgrade, to be published in IEEE Trans. on Applied Supercond., vol. 23, no. 3.

[3] S. Caspi, et al., Test and Analysis of Technology Quadrupole Shell (TQS) Magnet Models for LARP, IEEE Trans. on Applied Superc., vol. 18, no. 2, pp. 179-183, June 2008.

[4] G. Ambrosio, et al., LARP TQS01c Test Summary, Fermilab TD Note: TD-07-007; available at: http://tdserver1.fnal.gov/tdlibry/TD-Notes/2007%20Tech%20Notes/TD-07-007.pdf.

[5] P. Bauer, et alt., Concept for a QUENCH-CALCULATION PROGRAM for the Analysis of Quench Protection Systems for Superconducting High Field Magnets, Fermilab TD Note: TD-00-027, available at: http://tdserver1.fnal.gov/tdlibry/TD-Notes/2000%20Tech%20Notes/TD-00-027.doc.

[6] L. Imbasciati, Quench Protection Issues of Nb3Sn Superconducting Magnets for Particle Accelerators, Fermilab thesis, 2003, available at: http://lss.fnal.gov/archive/thesis/2000/fermilab-thesis-2004-14.pdf.

[7] D.R. Chichili, T.T. Arkan, J.P. Ozelis and I. Terechkine, Investigation of cable insulation and thermo-mechanical properties of epoxy impregnated Nb3Sn composite, IEEE Trans. on Applied Superc., vol. 10, no. 1, pp. 1317-1320, 2000.

[8] P. E. Fabian, N. A. Munshi, and R. J. Denis, Highly radiation-resistant vacuum impregnation resin systems for fusion magnet insulation, AIP Conf. Proc. 614, pp. 295-304.

[9] Composite Technology Development, Inc., CTD-101K Epoxy Resin System Datasheet, available online at http://www.ctd-materials.com/papers.

[10] M. Hooker, private communication.

[11] M. Bajko, G. Chlachidze, M. Marchevsky, J. Muratore, private communication.

EXPERIMENTAL RESULTS AND ANALYSIS FROM THE 11 T NB_3SN DS DIPOLE*

G. Chlachidze, I. Novitski, A.V. Zlobin, Fermilab, IL 60510, USA
B. Auchmann, M. Karppinen, CERN, Geneva, Switzerland

Abstract

FNAL and CERN are developing a 5.5-m-long twin-aperture Nb_3Sn dipole suitable for installation in the LHC. A 2-m-long single-aperture demonstrator dipole with 60 mm bore, a nominal field of 11 T at the LHC nominal current of 11.85 kA and 20% margin has been developed and tested. This paper presents the results of quench protection analysis and protection heater study for the Nb_3Sn demonstrator dipole. Extrapolations of the results for long magnet and operation in LHC are also presented.

INTRODUCTION

The expected upgrade of the LHC collimation system foresees installation of additional collimators in the dispersion suppressor (DS) regions around points 2, 3, 7 and high-luminosity IRs in points 1 and 5 [1]. The space needed for the collimators could be provided by replacing 15-m-long 8.33 T Nb-Ti LHC main dipoles with shorter 11 T Nb_3Sn dipoles compatible with the LHC lattice and main systems [2]. CERN and FNAL have started a joint R&D program with the goal of building a 5.5-m-long twin-aperture Nb_3Sn dipole suitable for installation in the LHC [3]. The program started with the design [4], construction and test [5] of a 2-m-long 60 mm bore single-aperture demonstrator magnet.

Due to large stored energy (a factor of 1.5 larger than in the Nb-Ti LHC main dipoles) the protection of the 11 T Nb_3Sn dipoles in case of a quench is a challenging problem. As in all accelerator magnets including LHC main dipoles, it will be provided with dedicated protection heaters installed in the coil to spread the stored electromagnetic energy over larger coil volume and thus reduce its maximum temperature and electrical voltage to ground.

Heater position plays an important role in magnet protection. The traditional position of protection heaters in accelerator magnets is the outer surface of the coil outer layer (OL), used practically in all present accelerator magnets including the LHC main dipoles [6]. It provides excellent mechanical contact between the heaters and the coil, and allows adequate coil electrical insulation from ground. However, coil volume directly heated by the protection heaters is limited to ~50% of the total coil volume in this design.

To increase the coil volume affected by the protection heaters, they could be placed both on the inner and outer surfaces of the two-layer coil or inside the coil between the inner and outer layers. Installation of the protection heaters in the high field areas should also increase their efficiency. The inner-layer heaters were used in D20 [7] and in LARP LQS and HQ models [8, 9]. The inter-layer protection heaters were used in the first Nb-Ti MQXB short models (HGQ) [10] and in the first FNAL Nb_3Sn model (HFDA01) [11]. However, both these approaches have some difficulties. The inner-layer heaters add an additional thermal barrier between the coil and liquid helium in the annular channel, reducing the coil cooling conditions. Moreover, the mechanical contact between the heaters and the coil in this case is weak and could easily be destroyed during the magnet assembly, cooling down, or operation. Partial heater separation was observed in LARP quadrupoles after testing in superfluid helium at 1.9 K [8]. The inter-layer heaters have good mechanical contact with both coils but they require significant electrical reinforcement of the coil inter-layer insulation to withstand the high voltages which may lead to significant reduction of their efficiency. They could also be easily damaged during the Nb_3Sn coil reaction, magnet assembly, and operation. Due to the above-mentioned difficulties both these approaches have not been used yet in magnets operating at accelerators. That is why the quench protection development for 11 T Nb_3Sn dipoles has started with the traditional outer-layer protection heaters.

This paper describes the design and parameters of the protection heaters used in the 2-m-long demonstrator dipole, and presents the first experimental data and results of analysis of quench protection studies. Results are extrapolated to a 5.5-m-long magnet and operation in the LHC.

MAGNET AND PROTECTION HEATER DESIGNS

Details of the 11 T demonstrator dipole design are reported in [4, 5]. The two-layer coils consist of 56 turns - 22 in the inner layer and 34 in the outer layer. Each coil is wound using 40 strand Rutherford cable [12] insulated with two layers of 0.075 mm thick E-glass tape. The cable is made of 0.7 mm diameter Nb_3Sn RRP-108/127 strand with a nominal J_c(12 T,4.2 K) of 2750 A/mm^2 (without self-field correction), a copper fraction of 0.53, and RRR above 60 [13].

The coils are surrounded by multilayer ground insulation made of Kapton, stainless steel protection shells, and laminated stainless steel collars. The collared coil is installed inside a two-piece iron yoke clamped with two aluminum clamps and stainless steel shells. In the longitudinal direction the magnet is constrained with two thick stainless steel end plates.

* Work supported by Fermi Research Alliance, LLC, under contract No. DE-AC02-07CH11359 with the U.S. Department of Energy and European Commission under FP7 project HiLumi LHC, GA no. 284404.

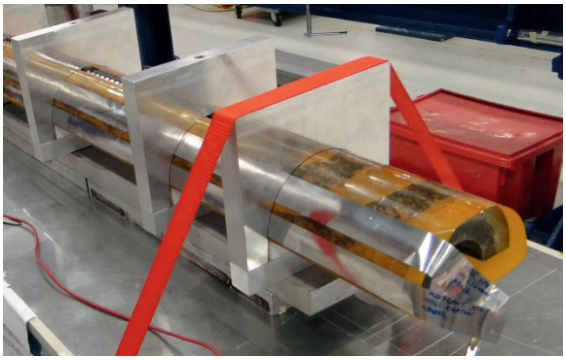

Figure 1: Two heater strips on one side of the coil.

Quench heaters are placed between the ground insulation layers of Kapton. The first Kapton layer, bonded to the coil outer surface, is 0.114 mm thick including the thin adhesive layer. All the remaining layers without an adhesive layer are 0.127 mm thick. The magnet quench protection heaters are composed of 0.025 mm thick and 2.108 m long stainless steel strips, 21 mm wide at the mid-plane low-field (LF) blocks and 26 mm wide at the high-field (HF) pole blocks. Two heater strips on one side of the coil are shown in Fig.1. The resistance at 300 K of HF and LF strips is 0.87 Ω/m and 1.06 Ω/m, respectively.

Two strips connected in series are inserted between the ground insulation layers on the outer surface of the coil blocks. The ground insulation design and protection heater position are shown in Fig. 2. Thickness of the insulation between the protection heaters and the coil is an important parameter for the heater efficiency and its electrical insulation from coil and ground. To find the optimal value for heater insulation satisfying the contradictory requirements two protection heaters were tested in the same coil. Each coil has two protection heaters marked as PH-1L and PH-2L. PH-1L is installed between the 1st and 2nd Kapton layers on one side of the coil and PH-2L - between the 2nd and 3rd Kapton layers on the opposite side.

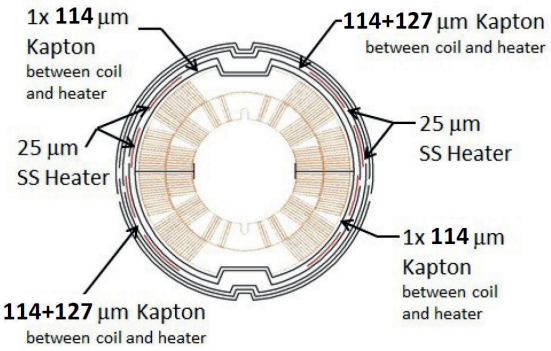

Figure 2: Ground insulation and protection heater position.

The corresponding protection heaters on each coil are connected in parallel forming two parallel heater circuits. The connection scheme of protection heaters in the 11 T dipole demonstrator is shown in Fig. 3. Each pair of protection heaters covers 31 turns (15 in the mid-plane and 16 in the pole block) per quadrant or ~56% of the total outer coil surface, or 28% of the total coil volume. The resistance of each protection heater measured at room temperature is ~5.9 Ω and ~4.2 Ω at 4.5 K.

Due to difference in width of heater strips (Fig. 1) the peak power density dissipated in the LF (mid-plane block) and HF (pole block) areas are also different. The peak power density in the low field area is more than in the high field area by about 50%.

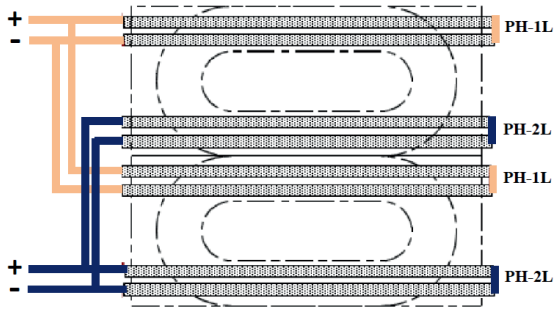

Figure 3: Heater connection scheme.

QUENCH PROTECTION PARAMETERS

The quench protection parameters of the single-aperture 11 T Nb_3Sn dipole at the LHC nominal current of 11.85 kA are summarized in Table 1. Table 2 shows the strand and cable parameters used in quench protection analysis.

QUENCH PROTECTION ANALYSIS

Coil Maximum Temperature and Quench Integral Limit

The maximum coil temperature T_{max} after a quench in adiabatic conditions is determined by the equation:

$$\int_0^{\infty} I^2(t)dt = \lambda \cdot S^2 \cdot \int_{Tq}^{Tmax} \frac{C(T)}{\rho(B,T)} dT \qquad (1)$$

where $I(t)$ is the current decay after a quench (A); T_q is the conductor quench temperature (K); S is the cross-section of the insulated cable (m^2); λ is fraction of Cu in the insulated cable cross-section; $C(T)$ is the average volumetric specific heat of the insulated cable ($J\ K^{-1}\ m^{-3}$); $\rho(B,T)$ is the cable resistivity (Ω m).

Table 1: Demonstrator dipole quench protection parameters

Parameter	Value
Effective magnet length (m)	1.7
Number of turns per coil (N_{turn}/coil)	56
Nominal current (kA)	11.85
Current density in Cu stabilizer (kA/mm^2)	1.362
Inductance at I_{nom} (mH/m)	6.04
Stored energy at I_{nom} (kJ/m)	424
Energy density W/V_{coil} (MJ/m^3)	85.9
Maximum quench field (T)	13.4
Critical quench current (kA)	15.0
Maximum stored energy (kJ/m)	680

Table 2: Strand and cable parameters

Parameter	Value
Cable width (mm)	14.85
Cable mid thickness (mm)	1.307
Strand diameter (mm)	0.7
Number of strands	40
Cu/SC ratio	1.11
Insulation thickness (mm)	0.1
Total cable area (mm^2)	22.7
Total strand area (mm^2)	15.4
Cu area (mm^2)	8.08
Non-Cu area (mm^2)	7.31
Insulation area (mm^2)	3.27
Void area filled with epoxy (mm^2)	4.01
Cu RRR	100

The dependence of T_{max} on the value of quench integral (*QI*) calculated for the demonstrator dipole cable insulated with E-glass tape and impregnated with epoxy for two values of the external magnetic field corresponding to the maximum and minimum fields in the coil is shown in Fig. 4. The thermal properties of the cable insulation (epoxy impregnated E-glass) were represented by G-10. Calculations were performed independently at FNAL and CERN using different databases for material properties. A good agreement of the results was obtained. Large effect of the magnetic field on the coil temperature is seen in Fig. 4. However, due to the current and field decay during a quench its effect on turn heating in the coil is smaller as shown in Fig. 5 where the magnetic field decay from B_{max} to 0 is taken into account.

To keep the cable temperature during a quench below 400 K, the quench integral has to be less than 19-21 MIITs (10^6 A^2·s). This criterion for a maximum cable temperature (still under discussion) is currently considered as an acceptable limit for Nb_3Sn accelerator magnets [14].

Protection delay budget

The maximum value of the quench integral in the turn where the quench originated is determined by the equation:

$$\int_0^{\infty} I^2(t)dt = I_0^2\tau_D + \int_{\tau_D}^{\infty} I^2(t)\,dt, \qquad (2)$$

where I_o is the magnet current when the quench started; τ_D is the total delay time including the quench detection, protection switch operation, and heater delay time; and *I(t)* is the current decay in the magnet after the protection heaters were fired.

Protection heater parameters such as heater delay time (the time between the heater ignition and the start of quench development in the coil) and coil volume under the protection heaters as well as quench propagation velocity in the coil provide significant impact on τ_D and *I(t)* in equation (2) and thus on the value of the maximum temperature in the quench origin area.

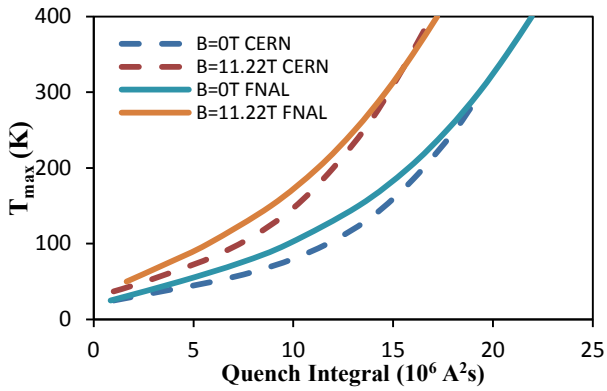

Figure 4: Cable maximum temperature T_{max} vs. Quench Integral *QI* for the insulated and epoxy-impregnated cable (strand RRR=100).

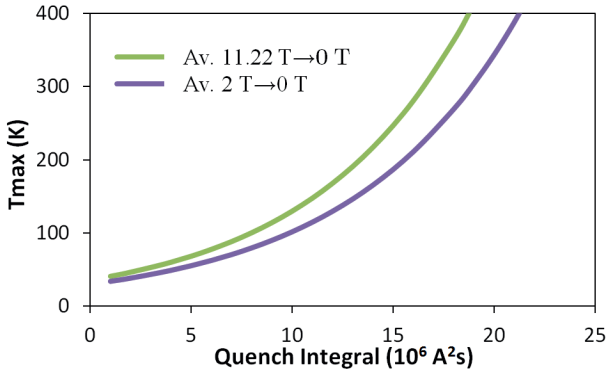

Figure 5: Cable maximum temperature T_{max} vs. quench integral *QI* for the insulated and epoxy-impregnated cable (strand RRR=100) corrected on the magnetic field decay in the IL pole turns (B_{max}=11.22 T) and the OL mid-plane turns (B_{max}=2 T).

The time budget τ_{budget} for τ_D (including the heater delay) is defined by the formula

$$\tau_{budget} = \frac{QI_{max} - QI_{decay}}{I_0^2}, \qquad (3)$$

where the maximum quench integral QI_{max} is calculated using (1) for the maximum allowed coil temperature of 400 K; QI_{decay} is the quench integral accumulated during the current decay; and I_0 is the magnet quench current.

The QI_{decay} could be estimated using formula (1) if the coil average maximum temperature under quench heaters T^{PH}_{max} is known. This temperature was calculated assuming that all the turns under the protection heaters quench simultaneously and the magnet stored energy is dissipated only in these turns

$$\frac{W(Io)}{l} \cong N_{qt} f S \int_{Tq}^{T^{PH}_{max}} C(T)\,dT, \qquad (4)$$

where $W(I_0)/l$ is the stored energy per magnet unit length (J/m); N_{qt} is the number of turns quenched by quench heaters; f is the number of quench heaters used in each coil (1 or 2).

The average maximum coil temperature under the heaters vs. magnet current is shown in Fig. 6. The longitudinal and transverse quench propagation is not

considered in these calculations. As it follows from the plot, at the nominal operation current 11.85 kA the coil maximum temperature under the heaters is less than 250 K, even with one operation heater circuit. T^{PH}_{max} is an important parameter which defines also the coil stress due to coil expansion inside the cold structure.

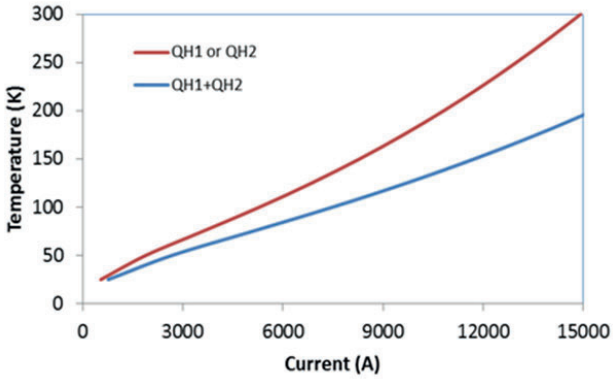

Figure 6: The average maximum coil temperature under the heater vs. magnet current for one and two protection heater circuits.

The calculated delay budget τ_{budget} for the inner-layer turns of the 11 T Nb_3Sn dipole vs. magnet current normalized to its short sample limit (SSL) is shown in Fig. 7 for protection with one and two heater circuits. The delay budget reduces with the magnet current reaching its minimum at the nominal operation current. For operation with two protection heaters the delay budget at I_{nom} (80% of SSL) is 50 ms and for one heater only 25 ms. Delay budgets in the case of quench development in the coil outer layer are larger due to the lower magnetic field: 30-50 ms for one PH and more than 200 ms for two PHs respectively.

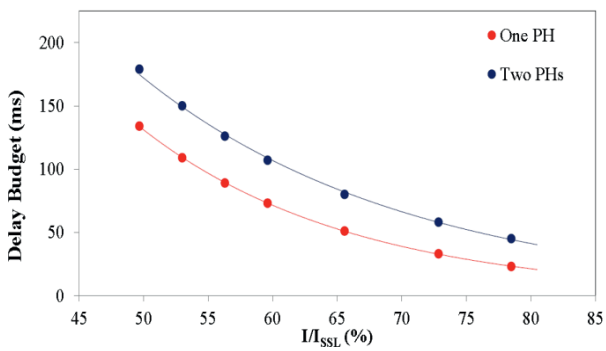

Figure 7: Calculated delay budget for the 11 T dipole vs. normalized magnet current.

Quench and heat propagation

The analysis described above does not consider the longitudinal and transverse quench propagation in coil nor the heat transfer inside the coil and between the coil and the magnet support structure. These effects increase the effective coil volume involved in the energy dissipation as well as dissipate some fraction of the stored energy outside the coil reducing the maximum temperature in the quench origin area and under the quench heaters. Consequently, the delay budget will also increase.

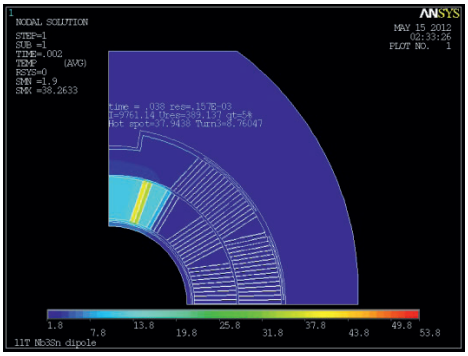

Figure 8: Temperature profile in the demonstrator magnet after 38 ms from the inner-layer pole turn quench.

The effect of the transverse heat propagation was analyzed using a 2D quench simulation code based on ANSYS [15]. Figure 8 shows the temperature profile in the demonstrator magnet after 38 ms from a quench at the nominal current of 11.85 kA in the inner-layer pole turn. It can be seen that the coil pole blocks and wedges are involved in the quench process absorbing a part of the dissipated heat and thus reducing the maximum temperature of quenched turn. Based on simulations the turn-to-turn propagation time is very short, less than 10 ms [16].

Figure 9 shows the temperature profile in the cross-section of the demonstrator dipole after 48, 96 and 552 ms from the heater induced quench at the coil initial current of 11.85 kA.

After ~50 ms from the protection heater discharge the quench starts in the outer-layer HF pole block. Then, in less than 100 ms, the quench propagates to the inner layer through the interlayer insulation. The outer-layer coil reaches its temperature of 150-213 K (compare with the average value of 150 K for QH1+QH2 in Fig. 6) after 550 ms from the heater ignition. As in the previous case, efficient heat transfer from the heater to the coil outer layer, from the outer-layer to inner-layer turns and other coil components helps to spread and absorb the magnet stored energy [16].

The results of the described quench analysis were further studied and experimentally verified during the quench protection studies in the 11 T demonstrator dipole [17].

EXPERIMENTAL STUDIES

The 11 T demonstrator dipole was tested at FNAL Vertical Magnet Test Facility [18] in June 2012.

Coil instrumentation

The coils were instrumented with voltage taps for the quench detection and localization. The voltage tap scheme for one of the coils is shown in Fig. 10. Voltage taps in pole turn allow measuring quench propagation velocity in the case of spontaneous quenches in this area. Voltage taps on each current block provide the quench propagation time between these blocks. In the next coils, spot heaters and more voltage taps will be added in coil

mid-plane and pole areas to measure the quench propagation speed and turn heating after quench.

A series of tests was performed to evaluate the efficiency of the heaters with different insulation (PH-1L and PH-2L) and the ability to quench the coil with a reasonably short delay time. Heater delay time was defined as the time between the heater ignition and the start of quench development in the coil. For each test, a pair of heaters with a specific insulation was fired while another pair of heaters were used for the magnet protection along with the stored energy extraction system. Due to limited quench performance of the magnet [5], heater tests were performed only at currents up to 65% of the estimated short sample limit (SSL). The energy extraction circuit delay was 1 ms for all heater tests except for the radial quench propagation study, during which the extraction dump was delayed for 120 ms.

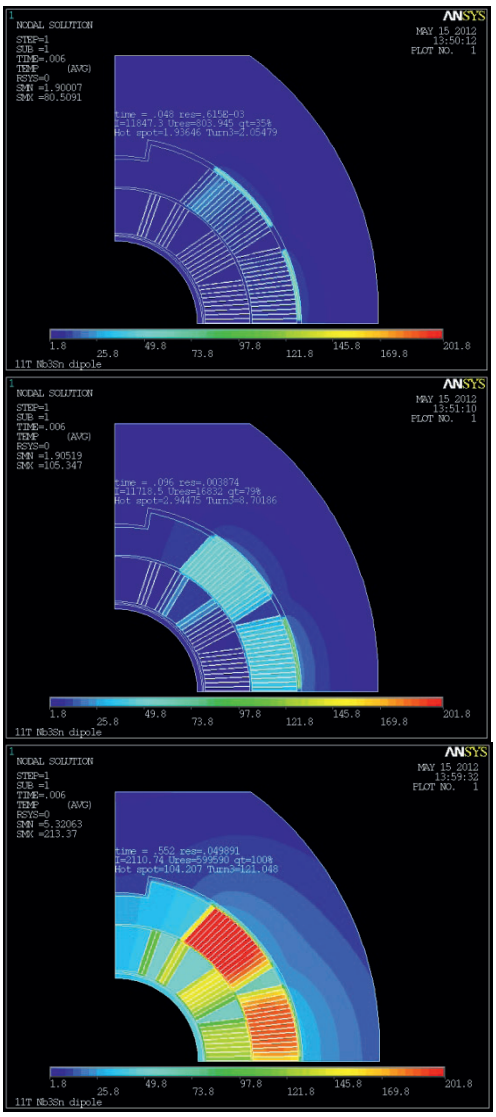

Figure 9: Temperature profile in the demonstrator magnet after 48 (top), 96 (middle) and 552 (bottom) ms from the heater induced quench.

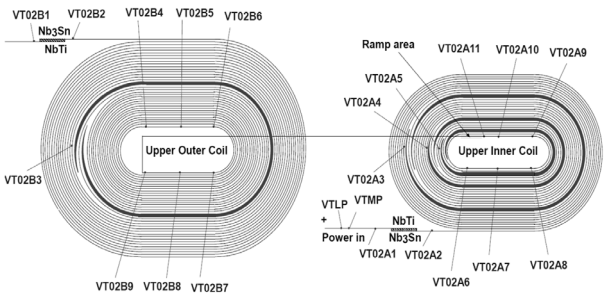

Figure 10: Voltage tap scheme in the 11 T demonstrator dipole coil.

Protection heater delay

Heater delay at a different SSL ratio (I/I_{SSL}) measured both at 4.5 K and 1.9 K is shown in Fig. 11 for the average heater power of 25 W/cm^2. Measured heater delay time is compared in Fig. 11 with the estimated delay budget presented in Fig. 7. Extrapolation of the measurement data to the nominal operation current (80% of the SSL) gives ~25 ms and ~40 ms heater delay time for PH-1L and PH-2L respectively. The corresponding extrapolated values at the injection current (5% of SSL) are ~420 ms and ~2000 ms.

The data in Fig. 11 show that the heater delay time is practically same at 4.5 K and 1.9 K temperatures, but it strongly depends on the heater insulation thickness. The dependence of the heater delay time on Kapton insulation thickness between the heater and the coil for the 11 T demonstrator dipole and some other Nb_3Sn coils used in LARP TQ and HQ models [8] are summarized in Fig. 12.

The measured heater delay time for PH-2L heaters with double Kapton layers of insulation itself is longer than the total available delay budget at all curents. The PH-1L heaters in the regular case, when both heaters are used for coil protection, provide ~25 ms margin with respect to the total delay budget which allows for necessary delays in the quench detection and circuit operation. However, in the case of only one heater operation (redundant case) this margin disappears. More time margin could be achieved by reducing the insulation thickness between the coil and heater, or increasing the peak dissipated power density.

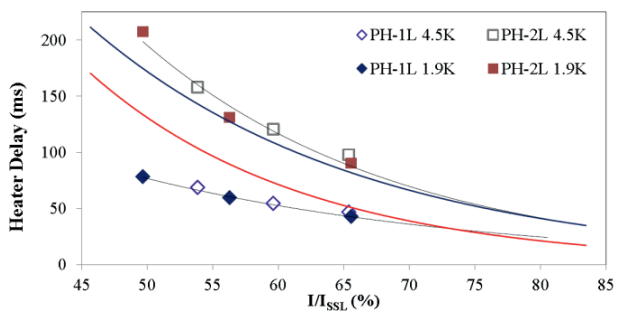

Figure 11: Estimated heater delay budget for operation with one (red line) or two (black line) heaters in each coil and measured heater delay at a different SSL ratio.

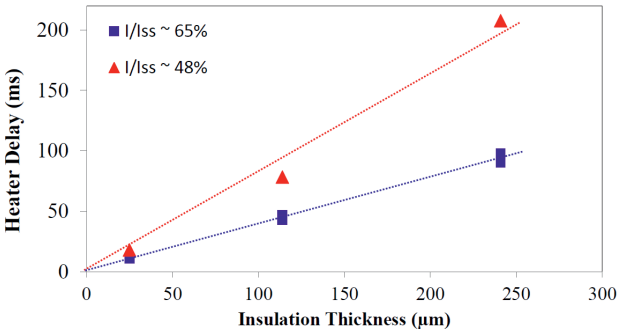

Figure 12: Heater delay time vs. insulation thickness.

Effect of heater power and energy

To study the additional possibilities to reduce the heater delay time and, thus, to increase the margin with respect to the total delay budget, the effects of the heater power and energy were measured. Heater delay time as a function of the peak heater power dissipated in the magnet at 4.5 K is shown in Fig. 13. The average peak heater power per heater area is defined as $I^2_{PH}\ R_{PH}/A$, where I_{PH} is the maximum heater current (A), R_{PH} and A are the heater resistance (Ω) and area (cm^2) respectively. The data are shown at the magnet currents corresponding to 60% and 65% of its SSL at 4.5 K. Changing the heater power by almost a factor of two proportionally reduces the heater delay time for both heaters. The highest heater power density of 25 W/cm^2 was achieved during the test with the existed heater firing units.

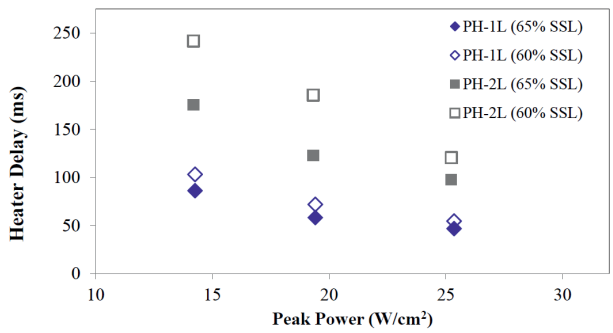

Figure 13: Heater delay as a function of peak dissipated power at 4.5 K.

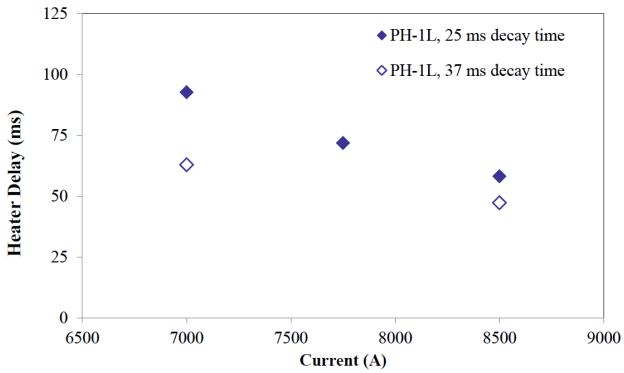

Figure 14: Heater delay as a function of magnet current for the peak heater power of ~ 20 W/cm^2 and different decay time constant of the heater circuit.

Heater delays could be further reduced by increasing the decay time constant (total energy deposited in heaters) of the heater circuit at the same peak heater power (Fig. 14).

Quench development in low field and high field blocks

Quench development and protection heater performance were studied for the Low Field (LF) and High Field (HF) outer-layer blocks since both these areas are covered by heaters. The heater strip width is not the same and as a consequence the peak power density is different in the LF and HF blocks.

The peak power density presented in the previous sub-section was averaged for both strips of the heater. The peak power density in the LF and HF areas can be presented as:

$$P_{LF} = 1.24 \cdot P_{av}, \qquad P_{HF} = P_{av}/1.24, \qquad (5)$$

where $P_{av}=I^2(R_{LF}+R_{HF})/(A_{LF}+A_{HF})$.

PH-1L and PH-2L heater delays in the LF and HF areas at 65% of SSL are shown in Fig. 15. The energy extraction circuit (dump) delay was 1 ms in these tests limiting possibilities of quench detection both in the HF and LF blocks. PH-1L heater delay in the low field area in most cases exceeded the quench detection time and thus the quench development in this area was not captured. That is why only once quench development was observed in the LF block for PH-1L with a delay time of ~20 ms with respect to the HF block.

Fig. 15 shows that all PH-2L induced quenches first developed in the low field area and only later in the high field area. The cause of this phenomenon is being investigated.

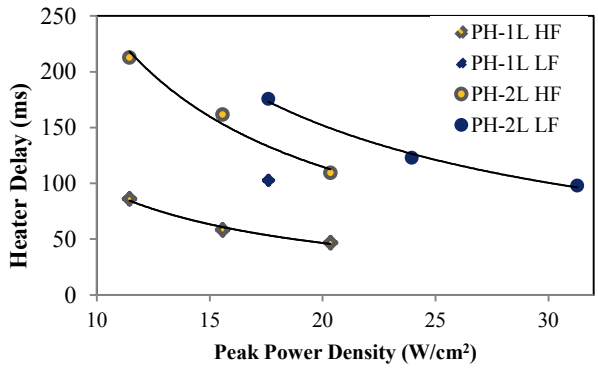

Figure 15: PH-1L and PH-2L heater delay in low and high field blocks as a function of peak dissipated power at 4.5 K.

However, this experiment shows that the delay between the HF and LF block quenches could be minimized or even completely avoided by optimizing the heater power in the HF and LF protection heaters.

Studies of LF and HF heater delay time will continue in next models. The protection heaters in the next 11 T dipole models will have only a single layer of Kapton insulation. The dump delay will be increased in order to

investigate the quench development both in the low and high field blocks.

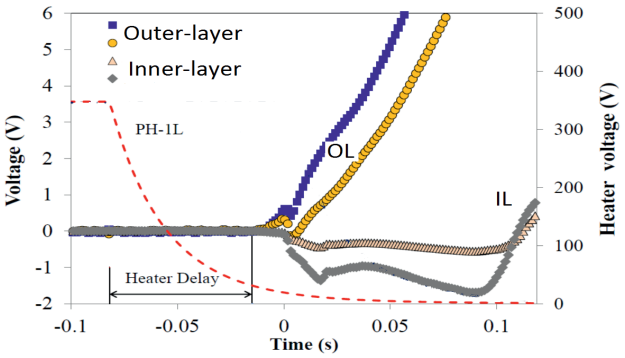

Figure 16: PH-1L heater-induced quench with a dump delay of 120 ms. Quench developed in 65 ms after heater ignition (PH-1L heater delay).

Radial quench propagation

To observe the quench propagation from the coil outer to the inner layer in heater-induced quenches at 4.5 K, the extraction dump was delayed by 120 ms. A quench at a magnet current of 8 kA (~62% of SSL) was provoked by igniting PH-1L while PH-2L was delayed and used for the magnet protection.

Figure 16 shows the development of the resistive voltage signal in the outer and inner coil layers. The heater voltage discharge in PH-1L is also shown in Fig. 16 (PH-2L ignition starts after the quench detection in the outer layer). After ~65 ms of the PH-1L ignition, a quench was initiated in the pole block of the outer coil layer. After an additional ~85 ms (still before the extraction dump was fired), clear resistive signals appeared in the inner coil layer segments. This experiment clearly confirms the rapid quench propagation from outer to inner layers in Nb_3Sn accelerator magnets predicted by simulations in [16].

Longitudinal Quench Propagation

Most of the training quenches started in the mid-plane area of the outer coil layer and only a few quenches occurred in the inner-layer pole-turn segments with highest magnetic field [4]. The longitudinal quench propagation velocity was measured in one of the quenches in the inner-layer pole turn at 4.5 K using the time-of-flight method as ~27 m/s. Quench current in this ramp was 9440 A, which corresponds to 73% of SSL at 4.5 K.

The measured value of the longitudinal quench propagation velocity is comparable to, or higher than results obtained for other Nb_3Sn magnets [19, 20]. Measurements of quench propagation velocity will continue on the next models with improved quench performance and coil instrumentation (spot heaters and additional voltage taps).

EXTRAPOLATION TO LONG PROTOTYPE AND LHC CONDITIONS

To predict the efficiency of protection scheme with outer-layer heaters used in the 11 T dipole demonstrator under "LHC conditions", ROXIE quench protection module [21] and the LHC MB quench protection system parameters were used [22].

ROXIE model calibration

The ROXIE quench module uses a thermal network with one temperature node per half-turn in the cross-section. For heater simulations a 2D model was used. The heat propagates from turn to turn and from layer to layer through the insulation. Heaters are modeled as one temperature node per strip, with the associated heat capacity of a stainless steel strip. The electrical power is discharged into the heat capacity. The protection heater heats the coil turns under the heater, and, through the ground insulation, supplies heat to the helium bath at constant temperature.

In the model, the thermal conductivity between the heater and the coil, and between the heater and the helium bath, are determined from user-supplied thicknesses and insulation materials. The 0.125 mm glass-epoxy wrap around the coil is also taken into account. The model includes the quench-back effect with rather low inter-strand contact resistance in cable R_c=30 μΩ and R_a=0.3 μΩ. However, analysis shows that the corresponding quench-back effect reduces the coil maximum temperature only by 5% [22]. The model, however, does not include the thermal contact resistances between heater and Kapton, individual Kapton layers, and Kapton and coil or collars. To take into account these additional thermal resistances, scaling factors were used to tune the model using the experimental data. Another model shortcoming is that the heater is connected to an isothermal bath, rather than to the outer structure. As a consequence, in the case of low heater power and/or low currents, i.e., whenever heater delays are long, the heater cooling is too strong.

Model tuning was done to fit the heater delays measured at 1.9 K for PH-1L with a single layer of Kapton between heaters and coils. The results are shown in Fig. 17. The scaling factor for the thermal conductivity through the Kapton insulation used for tuning purposes for the single-layer case was set to 0.42. For completeness, the two-layer case was also modeled with a scaling factor of 0.33.

Using the updated ROXIE quench protection module the radial heat propagation time was also estimated. During the heater test [17] at 8000 A, with 350 V on a 9.6 mF capacitance of the heater power supply, the measured time delay between a first quench in the outer layer and a propagated quench in the inner layer was 85 ms (see Fig. 16). In a simulation with tuned ROXIE model, this delay was 110 ms which is also consistent with ANSYS model prediction calculated at 11.85 kA

current (see Fig. 9). The results for some additional cases are presented in [22].

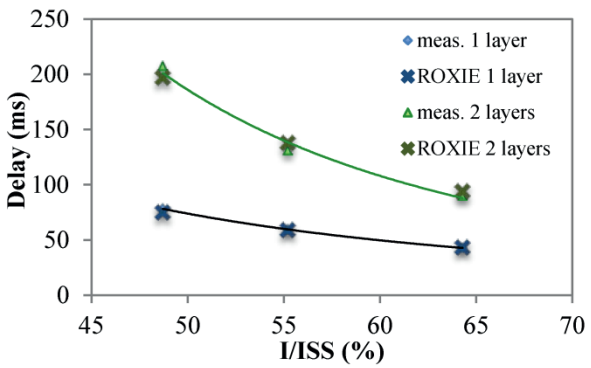

Figure 17: ROXIE model tuned to fit the measured heater delays.

LHC Conditions

Additional factors important for the 11 T dipole quench protection analysis in the LHC include the initial spread of the normal zone up to the detection threshold, validation time delays of the detection electronics, heater firing delays, the propagation of the normal zone into the inner layer, quench-back, and the number of turns under heaters to accelerate the current decay. Some of these parameters used for the LHC MBs are shown in Table 3.

Table 3: LHC MB quench-protection parameters

Parameter	Value
Nominal detection threshold (V)	0.1
Nominal validation delay (ms)	10
Minimum heater-firing delay (ms)	5
Actual heater delay in RB circuits (ms)	<50

To estimate the time delay from the start of an initial 3 cm long resistive zone until the threshold voltage of 0.1 V is reached, the 3D thermal network model was implemented in ROXIE. Simulations yield 3 ms if the quench starts in the peak-field conductor (inner-layer) at nominal current, and 34 ms if the quench starts on the outer-layer midplane conductor at the nominal current. The simulated turn-to-turn delays in the respective locations were 3 ms and 22 ms. Longitudinal propagation velocities of ~29 m/s if the quench starts in the peak-field conductor and ~6 m/s if the quench starts on the outer-layer mid-plane which is consistent with the measured value of ~27 m/s in the demonstrator dipole (see Subsection "*Longitudinal quench propagation*"). These low values indicate that a finer discretization in the third dimension might be needed.

Using the calibrated ROXIE quench protection module and the above quench protection parameters, the efficiency of the outer-layer heaters used in the 2-m-long demonstrator dipole was estimated for realistic LHC conditions. Simulations were carried out using a 5.5-m-long single-aperture dipole magnet for two cases:

- Two protection heaters (LF and HF strips on both sides of each coil), 70 W/cm^2 maximum heater power and a time constant of 74 ms.
- Only one protection heater (one HF strip and one LF strip on the opposite side of the coil), the same maximum heater power and time constant.

The results of simulation for the two cases are summarized in Table 4. The analysis shows that the outer-layer protection heaters can keep the coil maximum temperature below 400 K with two operational heaters per coil. In the case with only one heater the calculated coil maximum temperature is reaching ~450 K.

Table 4: Quench simulations for the 11 T dipole under LHC conditions

Parameter	2 heaters	1 heater
HF heater delay (ms)	15	15
LF heater delay (ms)	28	28
IL delay (ms)	52	69
QI total (MA^{2}s)	16.5	18.6
QI during current decay (MA^{2}s)	11.5	13.6
QI due to heater delay (MA^{2}s)	2.1	2.1
Peak coil temperature (K)	378	456
Peak heater temperature (K)	292	292

Note that the above numerical model is a mix of optimistic and pessimistic assumptions. On the pessimistic side, the low quench propagation velocity increases the quench detection time and coil cooling in the model is underestimated (heat transfer to the helium bath, to the coil components such as wedges and poles, and to the mechanical structure). The ANSYS analysis shows that these effects play an important role in reducing the coil maximum temperature. On the optimistic side, the detection threshold is only 0.1 V with 10 ms validation delay, which will only work if the voltage spikes are short and few; also the heater-firing delay is set to that of the fastest systems in the current main dipole circuits. The model improvement and analysis of 11 T dipole protection under LHC conditions will continue.

CONCLUSION

The high stored energy and low Cu/SC ratio in the cable, combined with the substantially larger temperature margins make the protection of the 11 T Nb_3Sn dipole a non-trivial problem.

Quench protection scheme based on the outer-layer protection heaters and two protection heater designs with 0.114 mm and 0.241 mm Kapton insulation thickness were analysed and experimentally evaluated for the 11 T Nb_3Sn dipole. The results of the study show acceptable heater efficiency and delay times for the heater with a single 0.114 mm thick Kapton film. This heater design will be used in the next 11 T dipole models. Fast quench propagation between the outer and inner coil layers was experimentally observed for the heater-induced quench. Longitudinal quench propagation velocity in a pole turn at ~73% of SSL was also measured. Due to limited magnet

performance, heater tests were performed only at magnet currents up to 65% of SSL. Quench protection studies will continue with improved 11 T dipole models and coils with additional instrumentation.

The efficiency of the outer-layer protection heaters with 0.125 mm Kapton insulation to protect the 11 T dipole in LHC was also estimated using the improved ROXIE quench protection module, for both the regular case with two heaters and for only one heater per coil. The analysis shows that the outer-layer protection heaters can provide magnet protection (keep the coil maximum temperature below the limit of 400 K) in the nominal case with two operational heaters per coil. The calculated coil maximum temperature in the case with only one heater is 10% higher than the limit, reaching ~450 K. This case needs more study, both theoretical and experimental. However, the experimental data, obtained during the heater studies in 11 T dipole demonstrator, suggest that improvement of PH performance (reduction of the heater delay time) could be achieved by reducing the heater Kapton insulation thickness to 0.1 mm (~15%), and thermal contact resistances between Heater-Kapton-coil by gluing the heaters to the coil surface during coil impregnation. Some additional increase of the average peak heater power would also help.

Some general questions related to the quench protection of Nb_3Sn accelerator magnets need to be further studied and addressed:

- What is the safe coil maximum temperature and average coil temperature under the heater for Nb_3Sn magnets? Is T_{max}=400 K a safe limit? Is this limit universal or it depends on the magnet type and design?
- What is the role of longitudinal and transverse quench propagation, quench-back, coil cooling in protection of accelerator magnets?
- How will the radiation-hard insulation affect the magnet protection?
- Are the inner-layer and inter-layer protection heaters reliable? Can they be used for protection of Nb_3Sn accelerator magnets? Are they compatible with the Nb_3Sn magnet fabrication process and operation in superfluid helium?
- What is the effect of mechanical stress and mechanical shock during quench on the long-term magnet performance?

ACKNOWLEDGMENT

Authors thank S.I. Bermudez and D. Tsirigkas (CERN) for their help with the ROXIE quench simulations.

REFERENCES

[1] L. Bottura et al., Advanced Accelerator Magnets for Upgrading the LHC, IEEE Trans. on Appl. Supercond., vol. 22, Issue 3, 2012, p. 4002008.

[2] G. de Rijk, A. Milanese, E. Todesco, 11 Tesla Nb_3Sn dipoles for phase II collimation in the Large Hadron Collider", sLHC Project Note 0019, 2010.

[3] M. Karppinen et al., Design of 11 T Twin-Aperture Nb_3Sn Dipole Demonstrator Magnet for LHC Upgrades, IEEE Transactions on Applied Superconductivity, Vol. 22, Issue 3, June 2012, p. 4901504.

[4] A.V. Zlobin et al., Development of Nb_3Sn 11 T Single Aperture Demonstrator Dipole for LHC Upgrades, Proc. of PAC'2011, NYC, 2011, p. 1460.

[5] A.V. Zlobin et al., Development and test of a single-aperture 11T Nb_3Sn demonstrator dipole for LHC upgrades, IEEE Trans. on Appl. Supercond., Vol. 23, Issue 3, June 2013, p. 4000904.

[6] LHC Design Report, vol.1, CERN-2004-003, 4 June 2004.

[7] R. Benjegerdes et al., Operational Characteristics, Parameters, and Hystory of a (13T) Nb_3Sn Dipole, Proc. of PAC'1999, NY, 1999, p. 3233.

[8] G. Ambrosio et al., Test results of the first 3.7 m long Nb_3Sn quadrupole by LARP and future plans, IEEE Trans. on Appl. Supercond., Vol. 21, Issue 3, June 2011 Page(s): 1858-1862.

[9] M. Marchevsky et al., Test results of HQ01, a 120 mm Bore LARP Quadrupole Magnet for the LHC Upgrade, IEEE Trans. on Appl. Supercond., Vol. 22, Issue 3, June 2012, p. 470200.

[10] S. Feher et al., Study of Low-β Quadrupole Magnet with Inter-Layer Quench Protection Heaters, Proc. of the 15th International Magnet Technology Conference (MT-15), Beijing, China, October 20-24, 1997.

[11] N. Andreev et al., Nb3Sn cos(θ) Dipole Magnet, HFDA01, Production report, TD-00-069, September 29, 2000.

[12] E. Barzi et al., Development and Fabrication of Nb_3Sn Rutherford Cable for the 11 T DS Dipole Demonstration Model, IEEE Trans. on Appl. Supercond., vol. 22, Issue 3, 2012, p. 6000805.

[13] M. B. Field et al., Internal tin conductors for particle accelerator and fusion applications, Adv. Cryo. Engr., vol. 54, pp. 237–243, 2008.

[14] G. Ambrosio et al., LARP Long Nb_3Sn Quadrupole Design, IEEE Trans. on Appl. Supercond., vol. 18, Issue 2, 2008, p. 268.

[15] R. Yamada et al., 2D/3D Quench Simulation Using ANSYS for Epoxy Impregnated High Field Magnets, IEEE Trans. on Appl. Supercond., Vol. 3, Issue 3, 2003, pp.1696-1699.

[16] A.V. Zlobin, I. Novitski, R. Yamada, Quench Protection Analysis of a Single-Aperture 11T Nb_3Sn Demonstrator Dipole for LHC Upgrades, Proc. of IPAC2012, New Orleans, 2012, pp. 3599-3601.

[17] G. Chlachidze et al., Quench Protection Study of a Single-Aperture 11T Nb_3Sn Demonstrator Dipole for LHC Upgrades, IEEE Trans. on Appl. Supercond., vol. 23, Issue 3, June 2013, p. 4001205.

[18] M.J. Lamm et al., A New Facility to Test Superconducting Accelerator Magnets, Proc. of PAC1997, Vancouver, 1997, pp. 3395-3397.

[19] S. Feher et al., HFDM4 Test Summary, Fermilab Technical Notes, TD-05-030, April 2005.

[20] M. Marchevsky et al., Quench Performance of HQ01, a 120 mm Bore LARP Quadrupole for the LHC Upgrade, IEEE Trans. on Appl. Supercond., Vol. 22, Issue 3, 2012, p. 4702005.

[21] ROXIE, http://cern.ch/roxie.

[22] B. Auchmann, 11-T protection study at CERN, CERN technical note, 06/11/2012.

MODELS AND EXPERIMENTAL RESULTS FROM THE WIDE APERTURE NB-TI MAGNETS FOR THE LHC UPGRADE

G. Kirby, B. Auchmann, M. Bajko, M.Charrondiere, N. Bourcey, V.I. Datskov, P. Fessia, J. Feuvrier, P. Galbraith, A. Garcia Tabares, J. Garcia-Perez, P. Granieri, P. Hagen, C. Lorin, J. C. Perez, S. Russenschuck, T. Sahner, M. Segreti, E. Todesco, G. Willering, CERN, Geneva, Switzerland

Abstract

MQXC is a Nb-Ti quadrupole designed to meet the accelerator quality requirements needed for the phase-1 LHC upgrade, now superseded by the high luminosity upgrade foreseen in 2021. The 2-m-long model magnet was tested at room temperature and 1.9 K. The technology developed for this magnet is relevant for other magnets currently under development for the high-luminosity upgrade, namely D1 (at KEK) and the large aperture twin quadrupole Q4 (at CEA). In this paper we present MQXC test results, some of the specialized heat extraction features, spot heaters, temperature sensor mounting and voltage tap development for the special open cable insulation. We look at some problem solving with noisy signals, give an overview of electrical testing, look at how we calculate the coil resistance during at quench and show that the heaters are not working We describe the quench signals and its timing, the development of the quench heaters and give an explanation of an Excel quench calculation and its comparison including the good agreement with the MQXC test results. We propose an improvement to the magnet circuit design to reduce voltage to ground values by factor 2. The program is then used to predict quench Hot-Spot and Voltages values for the D1 dipole and the Q4 quadrupole.

INTRODUCTION

For the phase-1 luminosity upgrade of the Large Hadron Collider at CERN, a development program was started in 2007 in collaboration with CEA-Saclay to develop a Nb-Ti 120 mm aperture quadrupole MQXC with an operational gradient of 120 T/m and the ability to extract heat loads of the order of 10 W/m. This quadrupole [1-4] had the innovative feature of an insulation scheme allowing a direct path from the helium bath to the superconducting strands [5].

After the decision of having only one upgrade, based on Nb_3Sn technology for the inner triplet, the MQXC program is the backup plan for the upgrade. Moreover, it allows testing the novel insulation scheme that may be used in the upgrade for the separation dipoles D1 and D2, for the two-in-one quadrupole Q4, and for the orbit correctors [6, 7].

In this paper we describe the final assembly of the first 2-m-long model magnet, that was assembled at CERN; we also describe the test setup, as well as results for the training, quench performance, and quench location, magnet protection and in particular quench heaters efficiency. Special tests were carried out to study heat extraction, with encouraging results.

NB-TI QUADRUPOLE FOR THE TRIPLET

Magnet assembly

As for the LHC main dipole, the coil layers, made up of two different cables, are wound and cured to size individually [4]. Inner and outer layers are then assembled together with the quench heaters between the two coil layers. The coils are measured and the ends are shimmed so that the coil pressure gradually reduces (at room temperature) from the 80 MPa in the straight section to 30 MPa at the coil extremity. The four poles are sorted to optimize the coil mid-plane position. During the assembly, coils are placed vertically around a spring-loaded, collapsible mandrel and held in place with straps (see Fig. 1).

Figure 1: Vertical assembly of the coils around the collapsible mandrel, and open ground insulation around the coils.

The cooling sheets are mounted on the coils and pass through the ground insulation providing an open path to extract heat from the coil to the superfluid helium bath. Full-length heaters are placed between poles in order to simulate the beam-induced heat load. The full-length collaring shoes are then placed on top of the ground insulation to protect it from being damaged by the collars.

To further improve the magnet cooling, the collaring shoes are also perforated with openings of about 30% of the surface area (see Fig. 2). The 3-mm-thick Nippon stainless steel collars (with a ±0.01 mm tolerance) are stacked around the aperture and spaced to give a 3.3% open gap between the collars to extract heat. Eight holes in the collars, placed at 30° w.r.t. the mid-plane, can be filled with magnetic shims to optimize field quality. The aperture is locked with eight full-length keys using a collaring press. After this operation, the mandrel is removed. After welding the end flanges on to the collared aperture, the joints are soldered in the joint-box.

Figure 2: Assembly of the collared coil: view of collars before compression, and collaring shoes with openings.

The collared aperture is then placed vertically in the yoking tooling. The yoke laminations are stacked with an identical system as used for the LHC main quadrupole assembly. The obtained yoke packing factor has been 99.6%, i.e. larger than the expected 98%. The magnet is completed with the placement of the yoke end flange and mounting the four 80 mm diameter tie rods to provide longitudinal load.

During collaring, one of the magnet cables that exit a coil had three strands accidentally cut. Since this damage is in a low field region it was expected to only marginally affect the performance, hence it has been decided to continue without repairing the cable, which would have required a complete disassembly.

Heat extraction features

Principal features that contribute to the heat extraction are:

- The cable insulation;
- The open ground insulation;
- Perforated collaring shoes;
- The spacing between collars providing a 0.2 mm gap for helium at 1.9 K;
- Helium slots in quench heater to allow steady state heat extraction.

The open ground insulation is based on the idea of having a direct helium path through the insulating sheets to the strands, yet maintaining the voltage integrity by virtue of the voltage break down path length of ~ 20 mm. A plastic sheet 0.5-mm-thick with machined slots on both sides is used. This is placed on top of the coils on all surfaces that are in contact with the magnet structure, providing 30% film of helium over the full coil to extract heat. Then the layers of Kapton ground insulation start to be applied. A second 0.5-mm-thick sheet with the same machined slots is engineered to be in contact with the layer touching the coil and pass through the ground insulting sheets until it lies on top of the insulation yet under the perforated collaring shoes, see Fig 2. The machined sheets can just be seen under the perforated collaring shoes. The final collaring is done with a horizontal press (see Fig. 3).

Figure 3: A view of the final stage of collaring.

The quench heaters are placed between the inner and the outer layer to act simultaneously on both layers; to improve the heat extraction during operation, quench heaters have slots to allow helium to flow from inner to outer layer, see Fig. 4. Moreover, during a quench heater firing, the helium in the slots would convert to gas and add to the acceleration of the quench over the uncovered coil surface. The quench heater was designed and tested to be hotter and faster than the LHC design. During test, we observed that the helium channels reduce the effect of the quench heaters, making them less efficient, so this design feature should be reviewed.

For the second model MQXC2 we have added two spot heaters, an array of voltage taps (see Fig. 5) and fast CCS temperature sensors to be able to measure the hot spot temperature in the coils (see Figs. 5, 6 and 7). We have evidence that using adiabatic assumption we significantly over estimate the hot spot temperature, due to the very efficient cooling through the cable, ground insulation, and open magnet structure.

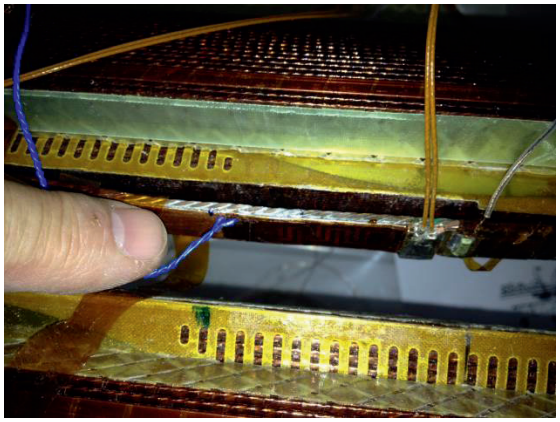

Figure 4: A view of the quench heaters with their cooling slots mounted between layers. We also see the spot heater and adjacent voltage taps.

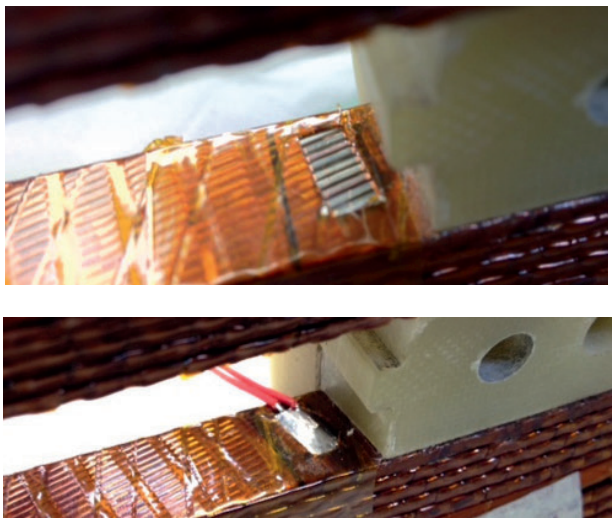

Figure 5: Window cut in cable insulation (upper part) to be able to mount temperature sensor or voltage taps on the cable (lower part).

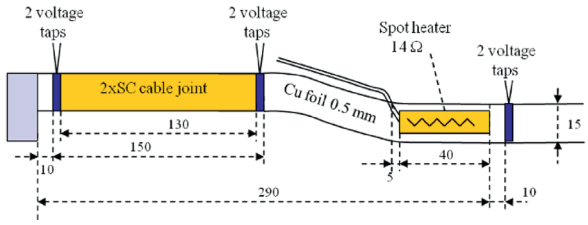

Figure 6: Schematic of spot heater position and voltage taps near the joint between inner and outer layer.

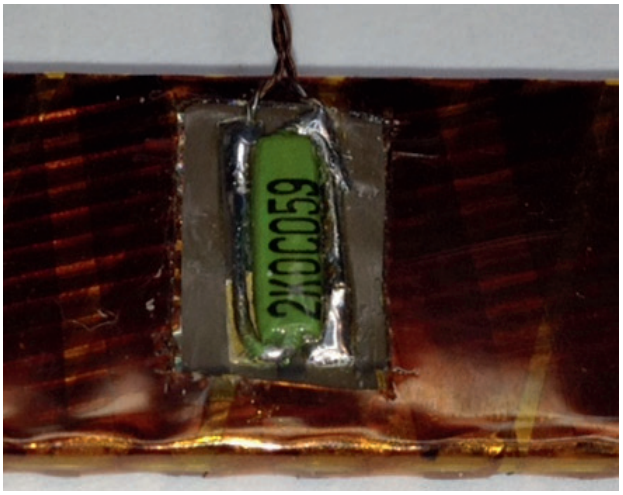

Figure 7: CCS temperature sensor mounted directly on cable. The sensor has a 0.025mm thick kapton film insulating it from the coil yet maintaining a rapid thermal response to temperature change during measurement.

The magnet joint resistance was measured during the powering tests and we found that there was a strong inductive element to the signal. After looking at photographs of how the voltage taps were routed out of the magnet we found a set of inductive loops, see Fig. 8. A correction will be implemented in the second model (see Fig. 9).

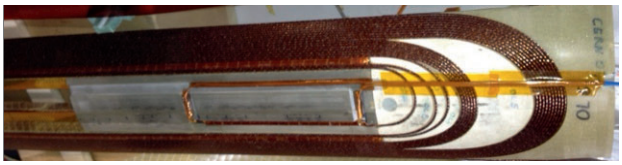

Figure 8: Inductive loop formed by the voltage taps coming from the interlayer joint in MQXC1.

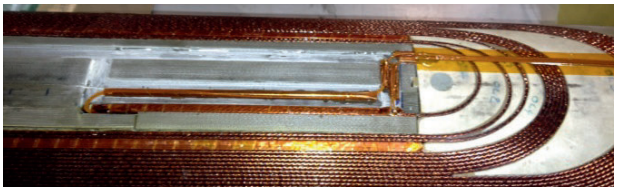

Figure 9: Correction to the loop adopted in MQXC2.

Electrical tests

The MQXC1 magnet also allowed to develop a comprehensive set of standard electrical test that will be applied to future magnets. The test starts with the coil after curing, still in the mould. The tests are repeated after each step of the magnet's assembly: coil winding, collaring, yoking, transport to test station, mounting on cold test support, and after insertion into the cryostat. A 1 kV pulse test looks for turn-to-turn shorts in the coil, using a resonating RCL circuit: a capacitor is charged to 1 kV and discharged into the coil. The four coils should have similar signals. If the exponential decay in a coil is slower than the others, the inductance is smaller and

therefore one has lost turns due to an internal short. After collaring, the ground insulation is tested with 5 kV between the coils and ground. The main coil parameters are measured, i.e., resistance and inductance at a few different frequencies. The quench heaters are fired at room temperature with their full voltage.

Each voltage tap wire is connected in series with a 10 kΩ resistor. This resistor protects the wiring in the event of an electrical short. All the instrumentation wiring from the magnet exits through the lambda plate feed-thoughts and out of the cryostat. The analog signals travel approximately 20 m from the cryostat to the analog-to-digital cards, where the quench trigger thresholds are set.

Magnet circuit

The magnet and the circuit during test are shown in Fig. 10. The 20 kA power converter is grounded on the negative side of the converter. Later we will discuss an improved position for the grounding point. The converter only has positive voltage so the negative ramps are driven by the decay through the room temperature current lead resistance.

The protection switch and dump resistor are large components. The dump can be configured to give combinations of the 4 × 20 mΩ resistors connected in series or parallel or combinations.

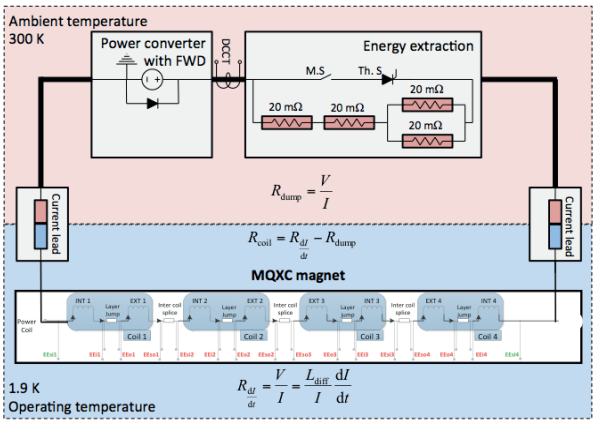

Figure 10: The magnet circuit in test stand.

Differential inductance measurements

The inductance measurement is performed by ramping up and down from 80 A to 12800 A at the nominal ramp-rate of 11 A/s. The inductance was deduced for the inner and outer layers of coil 1 to 3 separately, for the inner and outer layer of coil 4 combined and for the full magnet, see results in Fig. 11 and 12.

We see a significant hysteresis between 80 A and 2 kA due to the magnetization of the filaments. Estimates through a ROXIE [10] model are in good agreement with the measurements for the full magnet and show that the coil inductance is constant up to about 5 kA. Above 5 kA the inductance decreases due to saturation in the magnetic yoke.

When summing the inductance of the separate parts, the values do not add up to the full magnet inductance, because the voltage taps were wrongly installed forming a pickup coil and hence reducing the measured inductance. Additionally, inductances of 0.07 to 0.17 mH were measured with the voltage taps across inter-layer joints and inter-coil joints, which also indicate that voltages were picked up. In a next measurement the voltage taps will be changed such that the pick-up voltage is minimised.

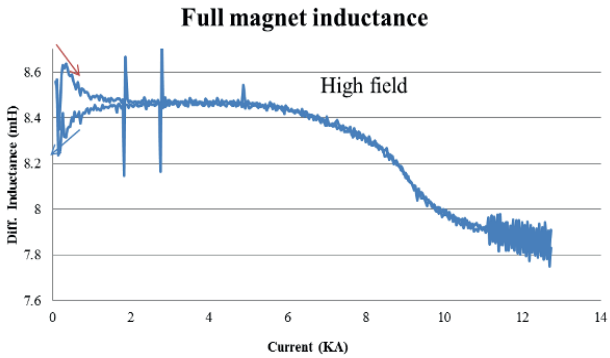

Figure 11: Differential inductance measured at 11 A/s.

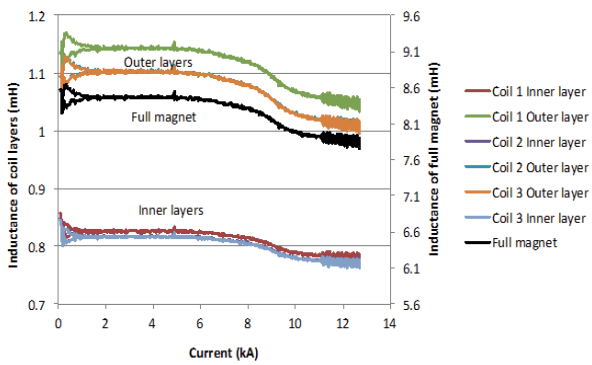

Figure 12: Differential inductance measured in each coil (left scale), and in the full magnet (right scale).

Quench-back test

A special test to study the quench-back has been done: the idea is ramping to nominal, open the switch and disconnecting the power supply, dumping the current into the external resistor. Then the instantaneous resistance of the coil $R_c(t)$ is estimated from the derivative of the current w.r.t. time

$$\frac{dI(t)}{dt} = -\frac{I(t)}{\tau(t)} \qquad \tau(t) = \frac{L(t)}{R_c(t) + R_d}$$

Where the nonlinearity of the inductance is taken into account, i.e. at each instant t we use the inductance $L(I(t))$. In a similar test, the Nb_3Sn quadrupole HQ developed a significant resistance (i.e. it quenched) due to the fast initial ramp rate [9]. In our case we see a very limited development of resistance of about 10 mΩ, see Fig. 13.

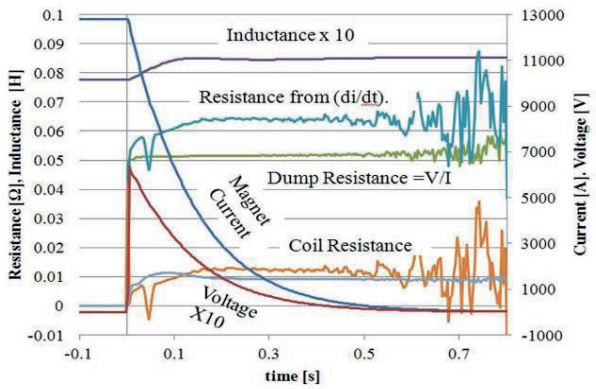

Figure 13: Resistance versus time during the dump of the current on external resistor at nominal current.

Quench heater performance

In Fig. 14 we estimated the resistance needed to protect the magnet as a function of the magnet current. We assumed a (fast) detection time of 12 ms. The light-green plot gives the circuit resistance needed to limit the hot spot to 100 K, a very conservative value where the coil thermal expansion is extremely low and will not induce any mechanical movement. At the operational value of 12.8 kA, 50 mΩ are needed. The purple plot is the circuit resistance needed to limit the hot spot temperature to 300 K. This is the limit we assume to avoid degradation: 20 mΩ are needed at operational current.

In the same figure, the red line is the measured coil resistance developed during test quenches. The detail of these measurements is shown in Fig. 15: the magnet quenchback does not provide significant resistance. The magnet was tested with the 50 mΩ dump resistance so it was not harmed. However if the dump was not activated, at nominal current 12800 A the adiabatic hot spot temperature is predicted to be 1200 K. So the conclusion is that the internal coil resistance is insufficient to protect the magnet.

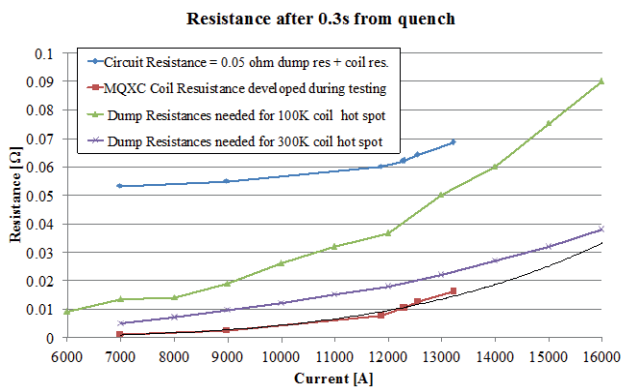

Figure 14: Circuit resistance needed to protect the MQXC model magnets as a function of magnet current.

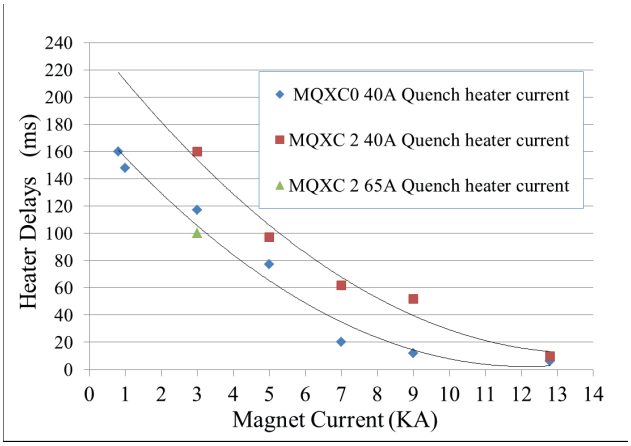

Figure 15: Quench heater delays with 40 A and 80 A in the heaters (markers) and parabolic fit.

In Fig. 15 we show the delay of the quench induced by heaters as a function of the current during a quench triggered by the heaters. At nominal current one has values of the order of 10 ms or less.

We checked not to overcome a temperature of 200 K in the quench heaters. We used a 200 Hz infrared camera to read the temperature after discharge at room temperature (see Fig. 16). Thermocouples mounted on the heater (see Fig. 17) allowed to measure the temperature in operational conditions, and to distinguish between copper plated and stainless steel zones (see Fig. 18).

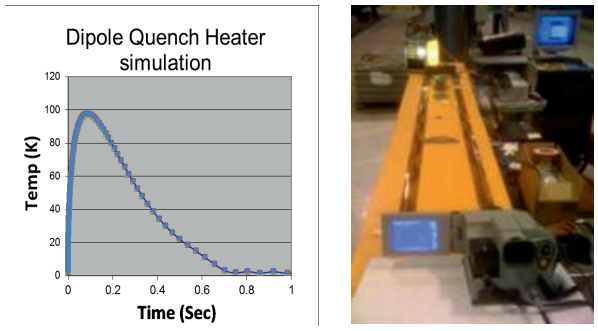

Figure 16: Calculated heater response and view of infrared camera measurement at room temperature.

Figure 17: Thermocouple mounted directly on stainless steel heater element, with the Kapton insulation cut away.

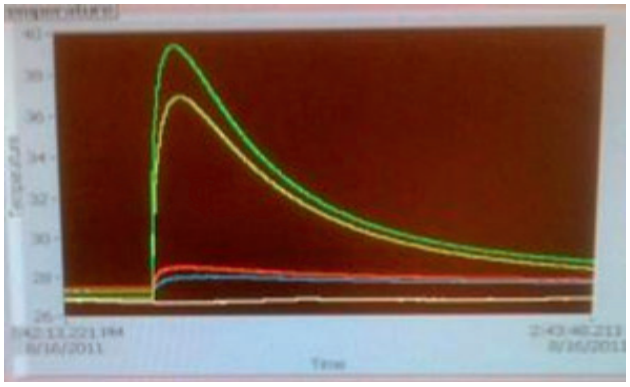

Figure 18: Thermocouple reading on stainless steel (green and yellow) and copper plated zones (red and blue). Reference thermocouple is in white.

Finite difference model

The quench calculation for assessing the magnet performance used a finite difference approach, implemented in an excel spread sheet, including the temperature dependence of the specific heat of the cable and the copper resistivity. The modelled circuit includes differential inductance for the magnet, quench heater delays for different parts of the coil, energy extraction to the resistive dump and resistance of the room temperature current leads. Althow we see good agreement with the calculated currents and voltages, we have no verification with a measurment of the hot spot temperature. An example of test results and the model results are given in Fig. 19 and 20.

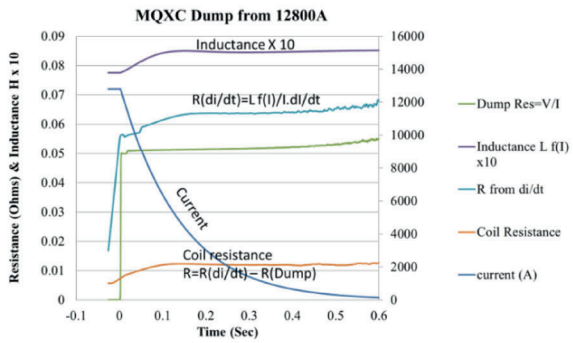

Figure 19: Test results for a quench at 12.8 kA.

Full length MQXC protection circuit

As the quench heaters still need development, one simple effective solution and safe alternative is to power the four insertion triplet magnets individually. The quench simulation for the 9.5-m-long magnet was performed. With an external energy extraction, a dump resistor of 130 mΩ, and 0.016 s delay this gives a hot spot of just over 250 K and the main bulk of the magnet is about 100 K. This uses the idea of placing the earth at the centre of the dump resistor, allowing to double the dump resistor value without increasing the voltage. Turn-to-turn and layer-to-layer voltages are unchanged between the earth configuration positions.

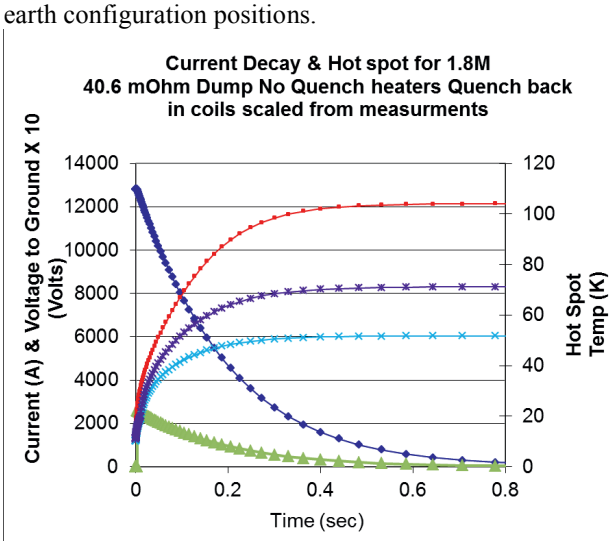

Figure 20: Model results for quench at 12.8 kA. Red is hot spot, light blue is outer layer, and purple is inner layer average coil block layer temperatures, Green is voltage across dump times 10, dark blue box is the current decay.

SEPARATION DIPOLE

For the separation dipole D1, single aperture, with an operational field of ~5 T and a total length of ~7 m, KEK colleagues are considering to using the LHC main dipole outer cable, and possibly the insulation used on MQXC, to take advantage of the high heat extraction that may be needed for this magnet.

The first quench study looked to see if the magnet could be protected with quench heaters as is standard in LHC large magnets. The 7-m-long magnet has a large bore, so the inductance to resistive coil ratio is high. The study showed that without dump we would need to quench 100% of the coil in 0.016 sec, reaching 260 K (see Fig. 21). On the other hand, with a 100 mΩ dump resistor and the same delay the hotspot temperature is below 200 K (see Fig. 22).

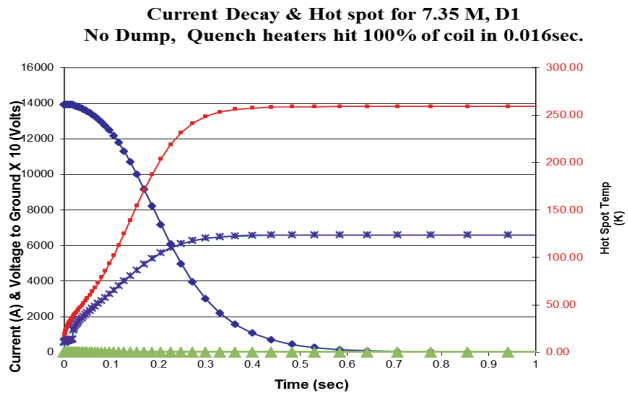

Figure 21: D1 quench simulation without dump resistor and with unrealistically fast heaters and quench coverage. Red curve is the hot spot, blue square is the current decay, purple is the average coil temperature, and green is the dump voltage.

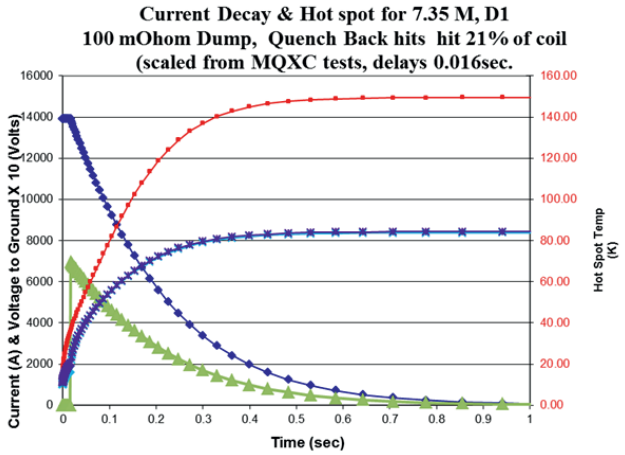

Figure 22: Proposed protection scheme with 100 mΩ dump resistor and quench heaters. Red curve is the hot spot temperature, purple square is the current decay, blue marker is the average coil temperature, and green is the dump voltage times 10.

LARGE APERTURE TWO-IN-ONE QUADRUPOLE

The Q4 under design at CEA (see Fig. 23) has a large aperture and could also possibly use the LHC dipole cable with the enhanced cable insulation as developed for MQXC. The heat load for this magnet can be high, so also in this case the cooling will be important. All the data for this magnet and others can be found at: www.cern.ch/hilumi/wp3. As for D1, energy extraction dump resistors over each aperture of the 4.5-m-long magnet limit the maximum hot spot temperature and maximum voltage to ground to an estimated 250 K and 800 V, respectively (see Fig. 24). The average temperature of the coil is at ~115 K. for this configuration.

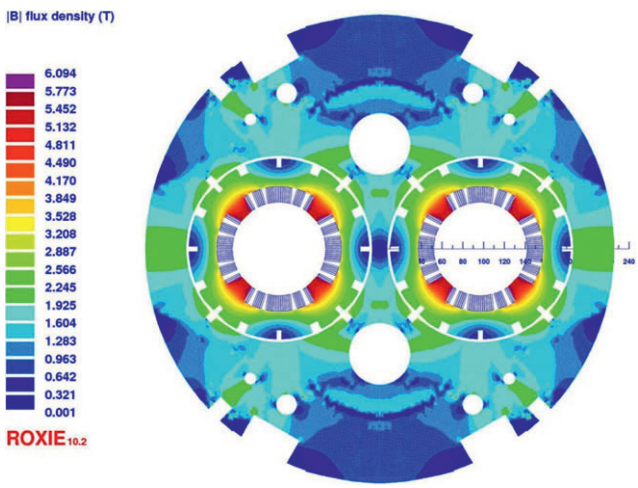

Figure 23: Q4 cross section

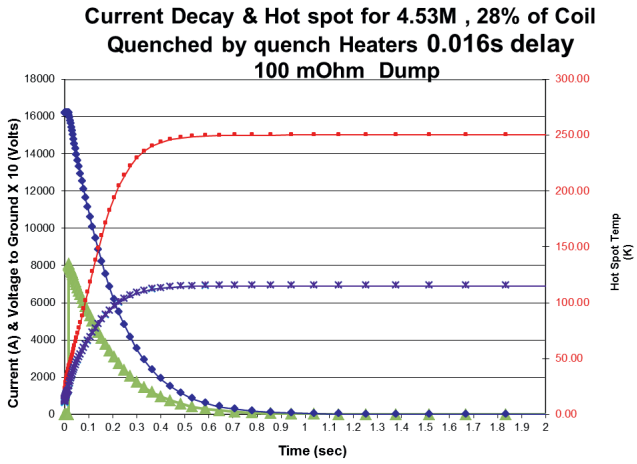

Figure 24: Proposed protection scheme with 100 mΩ dump resistor and quench heaters. Red curve is the hot spot, purple square is the current decay, purmpe X in the average coil temperature, green in dump voltage x10.

CONCLUSIONS

MQXC is the Nb-Ti option for the High-Luminosity LHC upgrade. It has been designed to maximize the cooling leaving open paths for HeII to the strands. Test results have shown some conflict between the need of a large heat extraction and the needs of quench protection. With a dump resistor the magnets proves to be protectable. Instrumentation has been installed for the next round of magnet tests to better understand hot spot and quench properties. Quench studies for both D1 and Q4 magnets, foreseen for the HL-LHC, indicate that a dump resistor can guarantee a safe protection scheme.

REFERENCES

[1] J. P. Kouthchouk, L. Rossi, E. Todesco, LHC project Report 1000 (2006).

[2] R. Ostojic, et al., Conceptual design of the LHC interaction upgrade, LHC Project Report, 1163 (2008).

[3] S. Russenschuck et al., Design challenges for a wide aperture superconducting quadrupole, IEEE Transactions on Applied Superconductivity, 21 (2011), 1674-7.

[4] G.A.Kirby, et al. Engineering Design and Manufacturing Challenges for a Wide-Aperture, Superconducting Quadrupole Magnet, IEEE Transactions on Applied Superconductivity, 22 (2012).

[5] M. La China, D. Tommasini, Cable insulation scheme to improve heat transfer to superfluid helium in Nb-Ti accelerator magnets, IEEE Transactions on Applied Superconductivity, 18 (2008), 1285.

[6] L. Rossi, these proceedings.

[7] Q. Xu, these proceedings.

[8] J. García Pérez, J. Billan, M. Buzio, P. Galbraith, D. Giloteaux, V. Remondino, Performance of the Room Temperature Systems for Magnetic Field

Measurements of the LHC Superconducting Magnets, presented at the 19th International Conference on Magnet Technology (MT19), 18-23 September 2005, Genova, Italy.
[9] H. Bajas, et al., these proceedings.
[10] S. Russenschuck, Field Computation for Accelerator Magnets, Wiley-VCH, 2010.
[11] F. Cerutti, B. Dehning, A. Ferrari, H. C., M. Mauri, A. Mereghetti, M. Sapinski, and E. Wildner, Estimation of threshold for the signals of the BLMs around the LHC final focus triplet magnets, ATS-Note-2012-014, CERN, Geneva, Switzerland, 2012.
[12] P. P. Granieri, Heat transfer through cable insulation of Nb–Ti superconducting magnets operating in He II, Cryogenics, in press.
[13] P. P. Granieri, Heat transfer between the superconducting cables of the LHC accelerator magnets and the superfluid helium bath, Ph.D. dissertation, Swiss Federal Institute of Lausanne (EPFL) and CERN, 2012.
[14] N. Mokhov, H. Rakhno, LHC Project Report 633 (2003).
[15] M. La China, D. Tommasini, Comparative study of heat transfer from Nb-Ti and Nb3Sn coil to HeII, Phys. Rev .STAB 11 (2008) 082401.

PROTECTION OF THE 13 T NB_3SN FRESCA II DIPOLE

Ph. Fazilleau, M. Devaux, M. Durante, T. Lecrevisse, J.-M. Rey, CEA DSM-IRFU-SACM, Gif-sur-Yvette, France

Abstract

The EuCARD project aims on construction of a 19 T hybrid dipole; it will be made of a 6 T HTS dipole associated to a 13 T outsert Nb_3Sn dipole [1]. This paper reviews the quench analysis and protection of the 13 T Nb_3Sn dipole.

INTRODUCTION

To study the protection of the dipole, first computations have been made with the QTRANSIT fortran code, which is a 3D simulation of the quench thermal transient in the magnet, based on the quench propagation velocities and the resistance growth with time. Even if it is a very reliable code, used and compared with test results on several magnets, it has been mainly applied to large magnets, indirectly cooled. Moreover, the usual propagation velocities formulas depend strongly on the magnetic field (magneto-resistance, current sharing temperature) and they are obviously not uniform within the winding. So we decided to further study the protection with the Finite Element Model (FEM) Cast3M [2], with modified procedures to take into account the decrease of the current with time, directly related to the joule losses dissipated within the winding.

The ignition and expansion of the quench has been studied with 3D models in the low field zone as well as in the high field zone: longitudinal propagation velocities have been computed and the internal resistive voltage gives the time needed to exceed the detection threshold. Once the detection is done and validated, the main contactor opens, with a discharge of the magnet into the dump resistor; heaters are activated and the FEM problem is reduced to 2D computations as the heaters are located all along the dipole.

The dipole is made of four double-pancakes: the coils of Fresca II are wound with a Rutherford cable composed of 40 strands with a diameter of 1 mm, with *Cu/Sc* = 1:3. Its length is 1.5 m and its total energy is 5.4 MJ. With a cold mass of 236 kg, its energy density is 18.4 J/g, comparable to the other magnets of same type [3].

PROTECTION PRINCIPLE

To start with the protection of a magnet, we can calculate analytically simple figures: if we consider all the energy dissipated uniformly in the dipole, the mean temperature is 126 K. If it is only in one pole, the mean temperature is 182 K. In a quarter of the magnet, the mean temperature jumps to 276 K. These figures, easily calculable, leads to two obvious conclusions: we need heaters in order to spread the quench within the largest volume of the dipole and the detection must be as fast as possible.

Consequently, the protection principle is the extraction of the energy into a dump resistor as well as the growth of the internal resistance due to heaters. Figure 1 is a sketch of the electrical circuit; the value of the external resistor is 95 mΩ, set so that the voltage at the terminals of the magnet never exceeds 1 kV, ±500 V to ground by means of the grounding circuit. The resistance volume has also been set so that the voltage at its terminals remains maximal as long as possible. This leads to a total volume of 2.63 liters.

Heaters are located on the sides of the double pancakes: two or four could be used by pole and computations will guide us to the correct choice. We set their power is 50 W/cm^2 and they will cover 50% of the total allowable surface.

The Fresca II dipole will operate with a YBCO insert magnet of 6 T; the latter is not taken into account in the protection study as its energy and self-inductance are low compared to those of the dipole. Consequently the discharge of the current is driven by the main Nb_3Sn magnet [4].

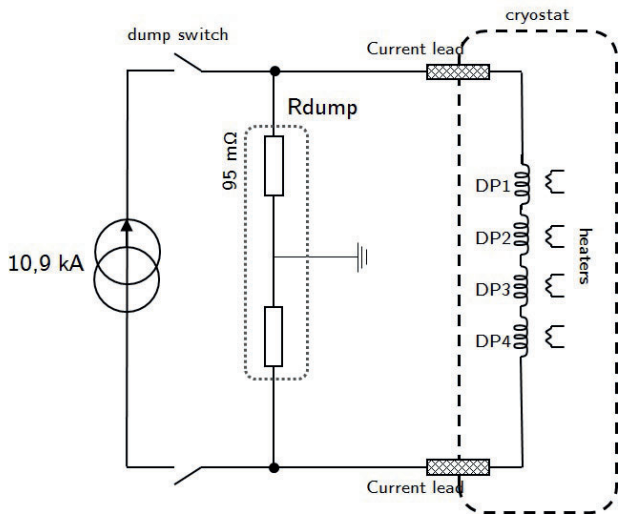

Figure 1: Protection circuit.

AFTER THE DETECTION: 2D COMPUTATIONS

As detailed supra, once the quench has been detected, the heaters are activated and the FEM problem is reduced to 2D computations. We are able to compute the temperature of the hot spot within the dipole as well as the current decrease evolution.

$$\int_{T_0}^{T_{max}} \frac{C_p(T)}{\rho(T)} dT = \int_0^{\infty} j^2(t)dt = \int_0^{t_{det}} J_0{}^2(t)dt + \int_{t_{det}}^{\infty} j^2(t)dt \quad (1)$$

This evolution is of primary importance as we can simply calculate the maximal temperature by applying the

adiabatic hot spot criteria (2) taking into account the nominal current during a time t_{det} followed by a fast discharge as shown in Fig. 2.

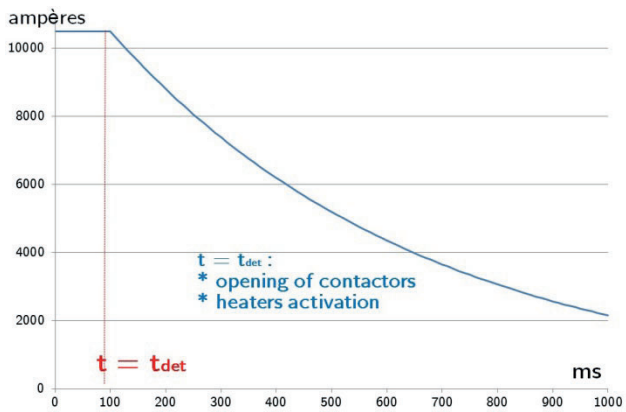

Figure 2: Current evolution.

Results of computations

Figure 3 shows the evolution of the volume of the resistive zone: it takes 20 ms after the activation of the heaters for quenching the first conductor, located in the highest field zone, where the margins are reduced. This delay is due to the thermal barrier made of kapton and insulation, located between heaters and conductors. The dipole is totally resistive after 430 ms.

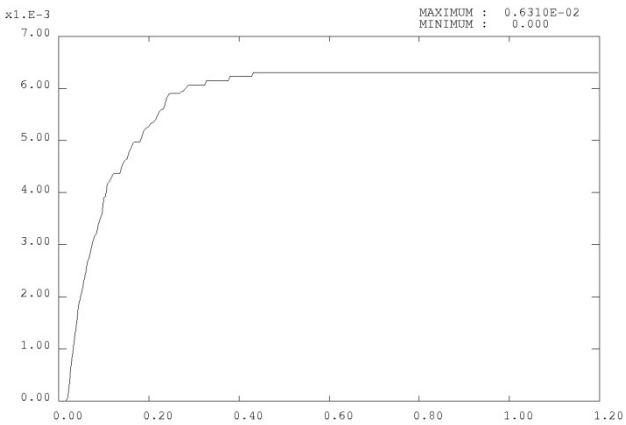

Figure 3: Evolution of the resistive zone volume.

The current decrease evolution is shown in Fig. 4. The time constant (*I/e*) is 0.57 s and it takes approximately 1.4 s to totally discharge the magnet. This evolution is used to calculate the hot spot temperature.

The dump resistor value increases by 30% during the discharge. Its temperature increases and reaches 638 K at the end of the discharge, which is an acceptable value. The voltage at its terminals, represented in Figure 5, remains maximal at the beginning of the discharge (nul slope) as we used for computations the volume mentioned *supra*; 65% of the total magnetic energy stored is dissipated in the dump resistor. The temperature field within the magnet at the end of the discharge is given in Fig. 6.

Adiabatic hot spot criteria

We have to check that the current evolution has been correctly computed before using it to calculate the adiabatic hot spot criteria taking into account the detection time t_{det}. So we compare the maximal temperature evolution from the 2D computation results with the hot spot temperature calculated with the current evolution. The evolutions are remarkably close to each other as shown in Fig. 7.

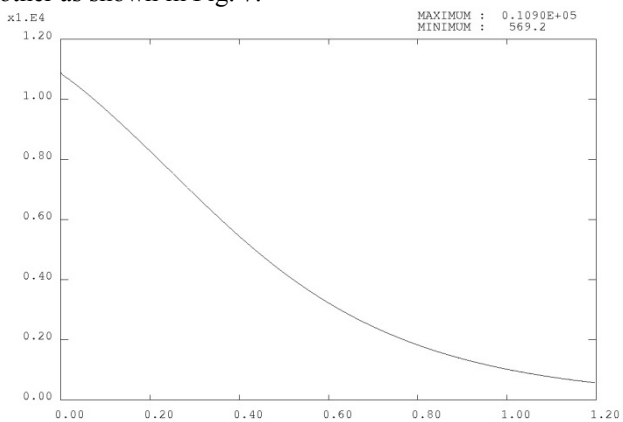

Figure 4: Evolution of the current.

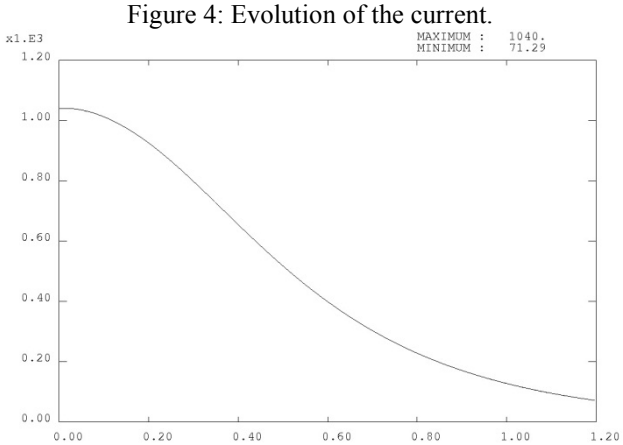

Figure 5: Evolution of the resistive voltage.

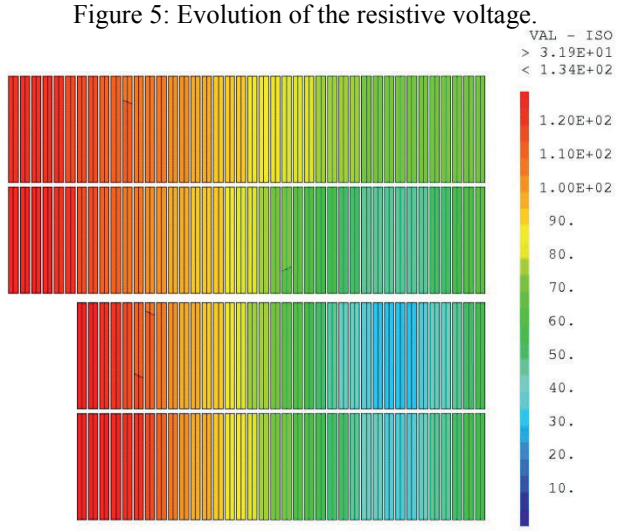

Figure 6: Temperature field at the end of the discharge.

We can now calculate confidently the hot spot temperature taking into account the detection time t_{det} and the results are shown in Fig. 8. The detection must be

lower than 25 ms if we want a maximal temperature below 150 K (four heaters case). With a detection time of 100 ms, the maximal temperature is 220 K for four heaters. The maximal temperature difference is around 30 K between two and four heaters.

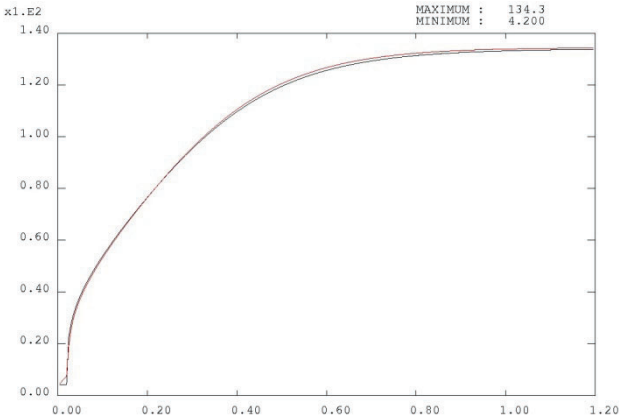

Figure 7: Comparison of the hotspot temperature evolution between adiabatic calculation and FEM computations.

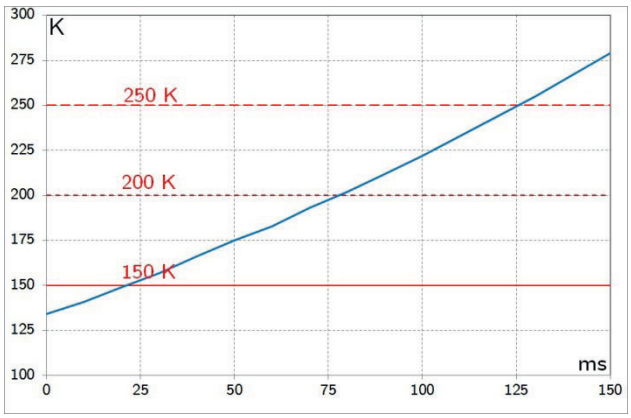

Figure 8: Hot spot temperature vs detection time.

The 2D study demonstrates that the magnet is not endangered: the use of four heaters decreases the maximal temperature - with value around 150 K to 250 K depending on the detection time - in the dipole and helps to distribute more uniformly the temperature (lower temperatures gradients).

BEFORE THE DETECTION: 3D COMPUTATIONS

After the 2D computations, we could have definitively concluded that the requested detection times are usually in the range 10 to 100 ms; nevertheless, we have been studying the propagation of the quench in the dipole with a 3D model. This is of great interest especially in the low field region as the quench propagates very slowly. The propagation is mainly longitudinal but the transverse one is also taken into account - especially in the high field region where the quench velocity is higher.

MPZ: benchmark of Cast3M

Before studying in details the propagation in the whole magnet, we have studied the minimum propagating zone in a single conductor to benchmark the FEM Cast3M code.

The heat equation for the 1D static case without helium cooling leads to the minimum propagating zone (MPZ) formula stated in equation (3).

$$l_{MPZ} = \pi \sqrt{\frac{\lambda(T_c - T_{cs})}{\rho j^2}} \qquad (2)$$

In the low field region, $l_{MPZ} = 26.5$ mm.

In the high field region, $l_{MPZ} = 5$ mm.

We inject in a unitary volume a pulse of energy and increase it up to the limit between recovery and expansion of the quench; the length of the resistive zone is the MPZ computed via the 3D model of the conductor. The injected energy at the limit should be the minimum quench energy (MQE). Nevertheless, it is strongly dependent on the step time used in the computations, contrary to the MPZ which is far less dependent. That is the main reason why we have studied the MPZ instead of the MQE.

Figures 9 and 10 show the results of the computations. The MPZ in the high field zone is 4.45 mm, a little bit lower than 5 mm, calculated with the formula (3). The agreement is even better in the low field region as the results of computations and formula calculation give the same value of 26.5 mm.

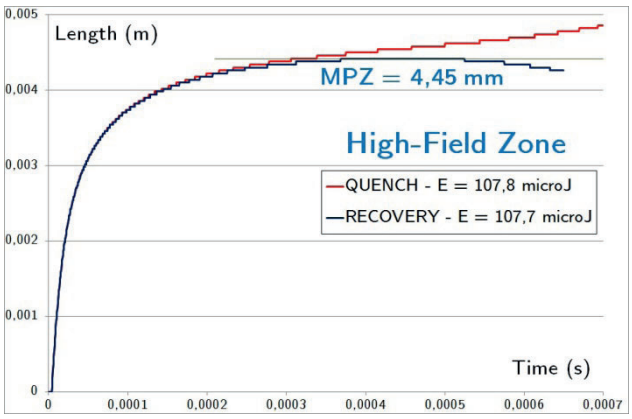

Figure 9: Length of the resistive zone - high field region.

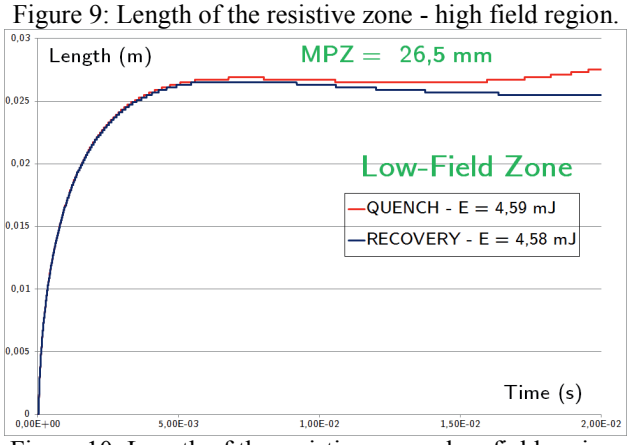

Figure 10: Length of the resistive zone - low field region.

The 3D model has been successfully benchmarked and if we quench a zone longer than the computed MPZ, we will initiate a quench that will spread in the whole magnet.

Propagation in the low field region

We now study the propagation of a quench in a 3D model of the complete dipole. After some transients due to the energy pulse, the propagation velocity in the low field zone (0.5 T averaged on a single conductor) tends to the value of 0.6 m/s. As above stated, in this region the quench expands very slowly in the magnet.

The internal voltage of the resistive zone is shown in Fig. 11. It takes 361 ms to exceed 100 mV. Nevertheless, due to the material characteristics in low field-especially the magnetoresistance-, the heating of the conductor is also very slow and the maximal temperature is only 47 K, 361 ms after the ignition of the quench, as shown in Fig. 12.

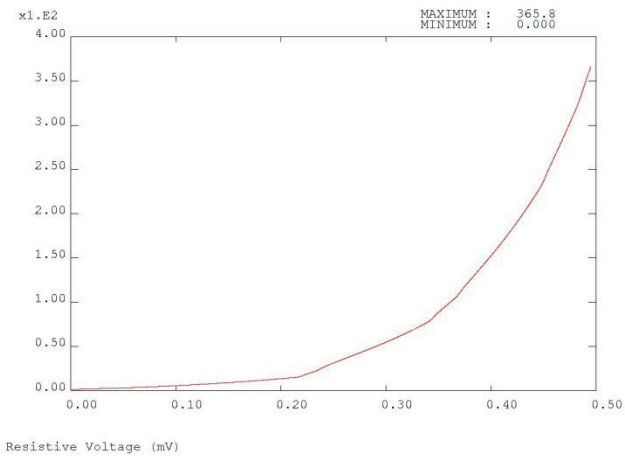

Figure 11: Resistive internal voltage in the low field region.

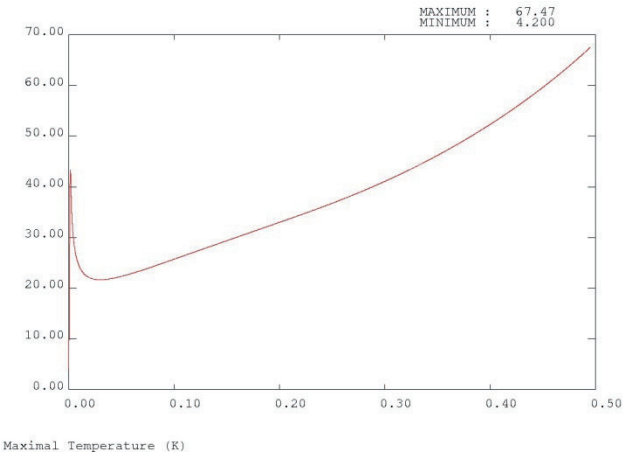

Figure 12: Maximal temperature in the low field region.

We can then compute the hot spot temperature from this point, adding 10 ms for the validation of the quench, 5 ms for the switch opening, and then injecting the current evolution computed from the 2D computations. If a quench occurs in the low field zone, with a detection threshold of 100 mV, the maximal temperature is 135 K.

Propagation in the high field region

The propagation is obviously higher with a velocity of 6 m/s. Figure 13 shows that it takes 28 ms to exceed 100 mV. The maximal temperature within the conductor is 33 K as shown in Fig. 14.

If a quench occurs in the high field zone, with a detection threshold of 100 mV, validation time of 10 ms, switch opening of 5 ms, the maximal temperature of the dipole at the end of the discharge is 157 K. We can compare this value with the 2D results taking into account a detection time of 43 ms; the temperature is slightly higher with a value of 166 K, as the adiabatic hot spot criteria is conservative.

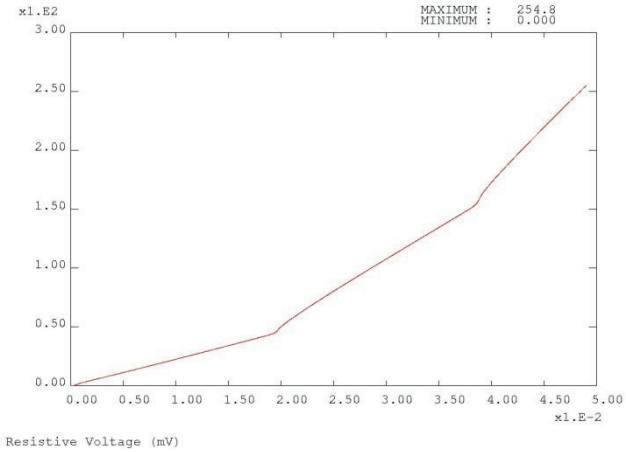

Figure 13: Resistive internal voltage in the high field region.

CONCLUSIONS

The quench study has been splitted in two parts. Before the detection, the quench ignition and expansion and the longitudinal propagation have been studied. The FEM based on Cast3m 3D has been benchmarked through estimation of the minimum propagating zone. The 3D computations in the low field zone show that the propagation is slow with a longitudinal velocity of 0.6 m/s but so is the temperature elevation; with a detection threshold of 100 mV, the maximal temperature is 135 K. In the high field region, the velocity is ten times larger and the 100 mV threshold is exceeded after 28 ms.

After the detection, heaters and dump resistor are taken into account and the problem, reduced to 2D computations, deals with the transverse propagation. Four heaters are needed to reduce thermal gradients. The voltage threshold of 100 mV led to a detection time of approximately 40 ms and a maximal temperature of approximately 160 K.

The Fresca II dipole will then not be endangered, mechanically or thermally, if the activation of the heaters is effective; the activation system must be redundant to avoid any fault scenario, invoking high thermal gradients and high temperature.

ACKNOWLEDGEMENTS

This work was supported by the European Commission under the FP7 Research Infrastructures project EuCARD, and is part of EuCARD Work Package 7: Superconducting High Field Magnets (HFM) for higher luminosities and energies.

REFERENCES

[1] G. de Rijk, "The EuCARD high field magnet project" *IEEE Trans. Appl. Supercond.* **22** 2012.

[2] P. Verpeaux, T. Charras, A. Millard, "CASTEM 2000 une approche moderne du calcul des structures", Calcul des structures et intelligence articielle (Fouet J.M., Ladeveze P., Ohayon R., Eds) *Pluralis* 1988, p. 261-271.

[3] P. Ferracin et al, "Development of the EuCARD Nb3Sn Dipole Magnet FRESCA2" *ASC conference* 2012.

[4] A. Stenvall et al, "Case study 6: protection of insert- outsert combined magnets - 6 T YBCO insert in 13 T background field produced with Nb3Sn Fresca II dipole" *WAMSDO 2013*.

PROTECTION OF THE 6 T YBCO INSERT IN THE 13 T NB_3SN FRESCA II DIPOLE

A. Stenvall, E. Haro, Tampere University of Technology, Department of Electrical Engineering, Electromagnetics, Tampere, Finland
Ph. Fazilleau, M. Devaux, M. Durante, T. Lecrevisse, J.-M. Rey, CEA DSM-IRFU-SACM, Gif-sur-Yvette, France
J. Fleiter, CERN, Geneva, Switzerland
M. Sorbi, G. Volpini, INFN Sezione di Milano LASA, Milano, Italy
P. Tixador, G2Elab/Institut Neel, CNRS/Grenoble-INP/UJF, Grenoble, France

Abstract

In the EuCARD project, we aim to construct a dipole magnet in YBCO producing 6 T in the background field of a 13 T Nb_3Sn dipole FRESCA II. This paper reviews the quench analysis and protection of the YBCO coil. In addition, a recommendation for the protection system of the YBCO coil is presented.

MAGNET SYSTEM

The YBCO dipole coil is a pre-accelerator magnet without beam tube. It consists of three stacked double pancake racetracks. A view of the coil is shown in Fig. 1. The magnet system is presented in detail in [1]. The magnet produces 6 T and it will be tested in the FRESCA II facility at CERN, providing a background field of 13 T [2].

The magnet will be wound from a cable made from two 12-mm-wide YBCO tapes manufactured by SuperPower. Additional copper stabilizer layers will be added to the cable. To reinforce the tape at its maximum operation field, 19 T, and high current density region, two 50 µm thick $CuBe_2$ layers are added to the cable. The cable is insulated with 30 µm thick Kapton insulation. A schematic view of the cable is shown in Fig. 2.

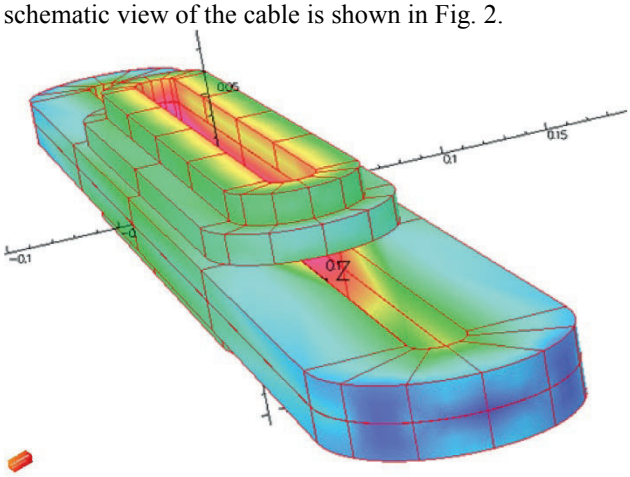

Figure 1: View of the YBCO racetrack insert.

In the coil, two of these cables are connected in parallel to reduce the coil inductance. The nominal operation current of the coil of 2800 A corresponds to an engineering current density of 252 A/mm^2. Critical current characteristics of the conductor were presented in [3]. Some characteristic values of the coil system, including the FRESCA II operating at bore magnetic field density of 13 T, are presented in Table 1. These parameters do not present the maximum operation conditions of FRESCA II at 1.8 K, but the design values for the combined operation with the YBCO insert at 4.2 K.

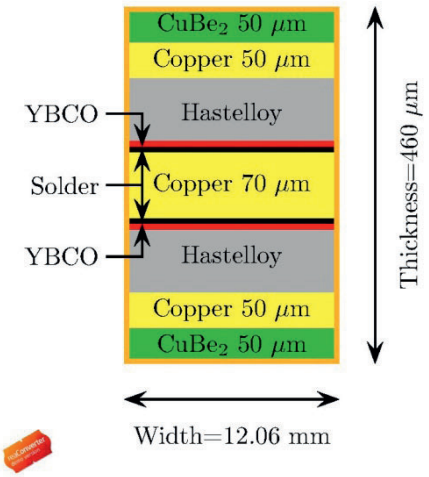

Figure 2: Schematic view of the cable for the YBCO racetrack insert.

Table 1: Parameters of the magnet system

YBCO insert		
Inductance	(mH)	4
Operation current	(A)	2800
Slef-energy	(kJ)	15.7
FrescaII		
Inductance	(mH)	98
Operation current	(A)	10500
Self-energy	(kJ)	5400
Mutual inductance	(mH)	9.3
Total energy	(kJ)	5690

QUENCH MODELING AND PROTECTION SCHEME

Preliminary quench analysis and protection scheme of the magnet have been presented in [4]. Rest of the work will be presented later [5]. Here we consider how the

temperature distribution evolves inside the YBCO coil when it quenches and how rapidly the current can be decreased to zero with an external dump resistor circuit. Due to the small energy stored in the insert, we considered only the external dump resistor circuits for the protection. We did not include the protection circuit into the finite element method based quench simulations.

Quenching an HTS magnet is difficult due to the high stability margin that HTS magnets typically have in large parts of the winding. There are, at least, two options to quench a magnet in simulations. First, one can simulate an additional heat input to some volume. This could, however, mean that in order to keep the volume small (length few mm of cable), one might need to increase the local temperature to as high as 100 K. This is not practical. Another option is to set a volume with reduced critical current to the coil. We used this option for quenching. The quench simulation time depends greatly on the size of this volume. We set this volume to the cable around the point where the minimum critical current was. To ignite the quench relatively fast, we set the length of this volume, part of the actual cable, to 10 cm and the critical current in this volume was fixed to 0 A. In [4] it was shown that the value of degraded critical current has negligible influence on the hot spot temperature at quench detection threshold voltage. Only the time from the beginning of the simulation to the quench detection changes considerably.

It is well known that in HTS coils the quench propagates very slowly and typically large part of the coil remains at operation temperature during a quench. Thus, we modelled only the top double pancake in the quench simulations. Different regions in the modelling domain are shown in Fig. 3.

We modelled part of the coil with insulation-tape-insulation structure and part of the coil was modelled as a homogeneous mixture of anisotropic material having effective material properties. In the upper coil, 11 of 35 turns were modelled with insulation-tape-insulation structure. In the lower coil 16 of 61 tapes were modelled in this way. Figure 4 shows the temperature distribution in that part of the coil where the temperature is higher than 8 K. Time instant is at the end of the simulation, i.e. maximum temperature is 400 K. As can be seen, the heat distributes only to a marginal part of the coil even at such a high hot spot temperature, thus demonstrating the feasibility of this approach.

In this simulation, the operation current was kept constant. Then, we can directly see what would be the temperature of the coil at given quench detection voltage. The simulation was terminated when the maximum temperature reached 400 K. Then the time was about 1 s. There were about 200 000 degrees of freedoms and the solution took about 50 hours. Custom-built finite element method quench software was used for the solution [4,6,7].

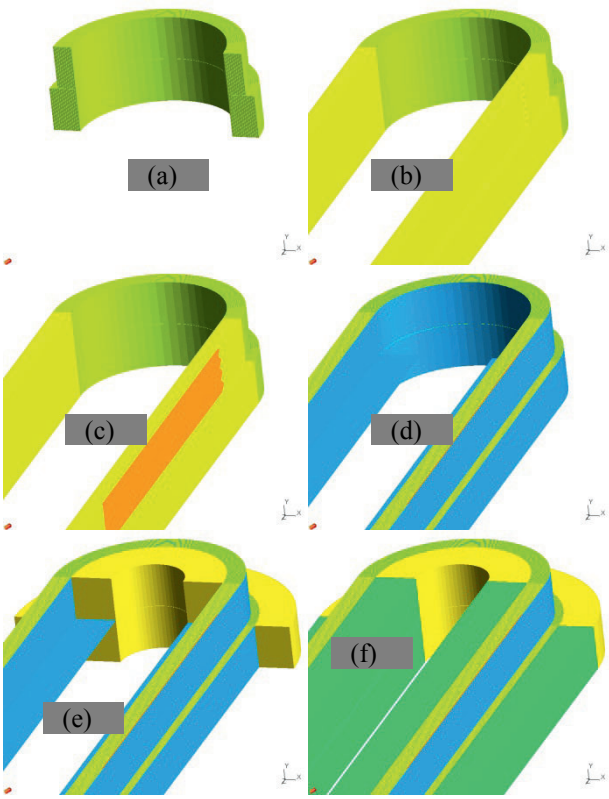

Figure 3: View of the different domains used in the quench simulations of the top double pancake shown in Fig. 1. One new domain type is added from subfigure to another. (a) tapes at the other end of the coil, (b) tapes at the straight parts, (c) volume with reduced critical current, (d) insulation, (e) other end modelled with effective homogeneous anisotropic material properties, (f) straight parts modelled with effective homogeneous anisotropic material properties.

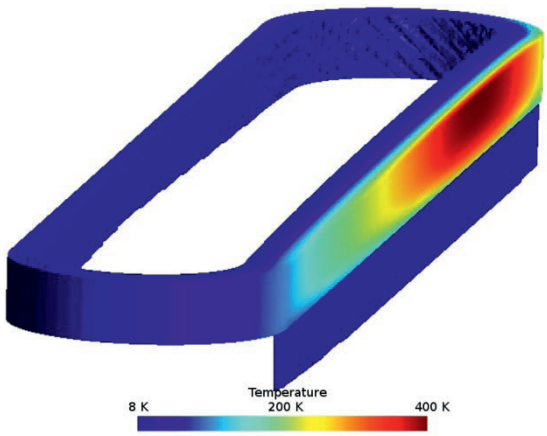

Figure 4: Temperature distribution at the end of the quench simulation.

Current sharing temperatures in the cross-section of the reduced domain and on top of the upper coil are shown in Fig. 5. These demonstrate the relatively large stability margin in the range 5-20 K.

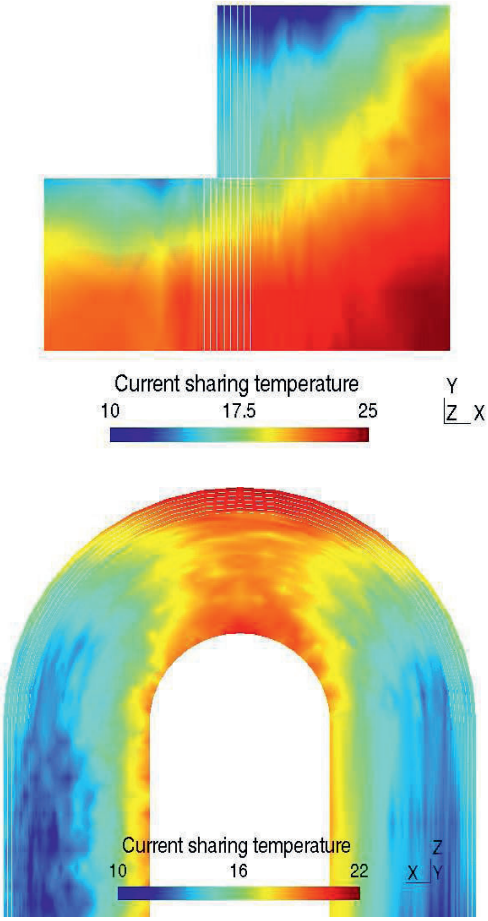

Figure 5: Current sharing temperature in the cross-section of the coil in the middle of the hot spot region (a) and on the top of the coil (b).

Especially in the lower coil, there are regions where a temperature increase to almost 25 K is required for current sharing temperature. In these simulations the redistribution of the current in one conductor during local heating was not considered, but the current density was always assumed to be homogeneously distributed in the cable and consequently heat generation was computed. It is of interest to develop modelling tools for this kind of modelling for the YBCO magnets of the future.

It is very unlikely that the middlemost coils quench, if the conductor is of good and homogeneous quality. Furthermore, the critical current decreases very slowly as a function of temperature and consequently heat generation increases slowly. This leads to slow normal zone resistance increase.

The hot spot temperature as a function of time and terminal voltage are shown in Fig. 6. The quench detection threshold voltage is expected to be 100 mV, corresponding to an hot spot temperature below 100 K at the quench detection time instant. This is safe and certainly allows a rapid discharge before the coil is damaged due to overheating and insulation or YBCO layer melting. The thermal stresses due to the localized hot spot might pose other problems, but they are not considered here.

Two possible protection circuits of the insert are shown in Fig. 7. In the simpler one, the dump resistance is determined by maximum allowable terminal voltage of the magnet, 800 V. For the variable dump resistor, a gate-turn-off-thyristor (GTO) circuit can be used to adjust very rapidly the dump resistance in order to speed up the current decay. This method is effective for coils where the normal zone resistance grows very slowly and if quench heaters are not used. However, it complicates the protection circuit and as a new proposal introduces reliability risks before the circuit is actually built and tested.

Fig. 8 presents the operation of the protection circuit with time varying dump resistance. The steps for switch openings are determined by the quench analysis of FRESCA II [8]. Analysis is performed in such a way that the insert terminal voltage is kept at maximum in the range 800-1000 V.

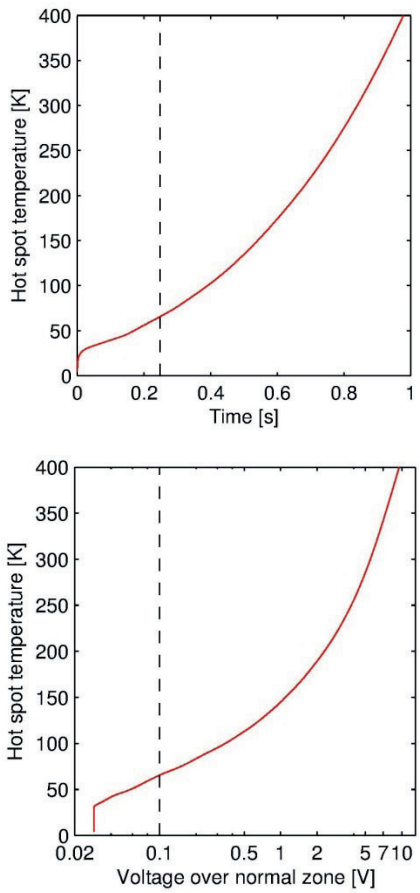

Figure 6: Hot spot temperature as a function of (a) time and (b) terminal voltage. Dashed lines present detection voltage threshold.

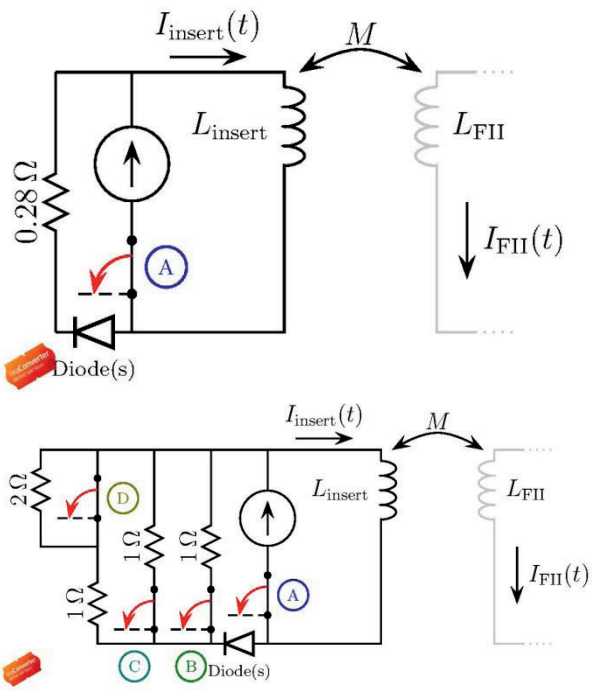

Figure 7: (a) basic protection circuit with a constant dump resistance. (b) protection circuit with varying dump resistance.

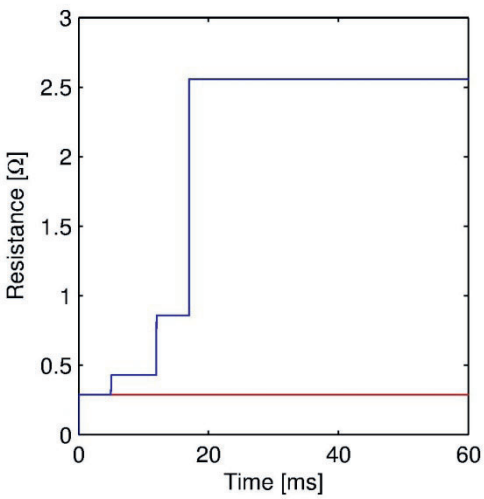

Figure 8: Effective resistance of the protection circuit during its operation.

Rapid insert discharge with the two possible protection circuits are illustrated in Fig. 9. With the time varying dump resistor, the current decay time can be reduced to 20 ms from 50 ms, still keeping the terminal voltage within acceptable limits at all times.

The variable dump resistor circuit allows the discharge of the insert in such a short time that the quench protection circuit of FRESCA II can be activated after the insert is in open circuit. This gives ultimate safety to the insert since no circulating currents are induced to it during the FRESCA II current decay. It is another question whether this is necessary or not because even with the constant dump resistor circuit no excess current is induced to the insert as shown in Fig. 10. Also in this case the insert terminal voltage remains within tolerable limits.

Finally, the open circuit voltage of insert during FRESCA II quench is shown in Fig. 11. This is clearly in safe limits. The rapid discharge of the insert might cause problems to the FRESCA II because of the induced current. This causes certain requirements to its power supply unit. It is to be explored whether this is tolerable or not and whether it is worth the risk to even consider this protection circuit. The simplest option would be to use the constant dump resistor circuit and in case of a quench, activate both the protection circuits simultaneously.

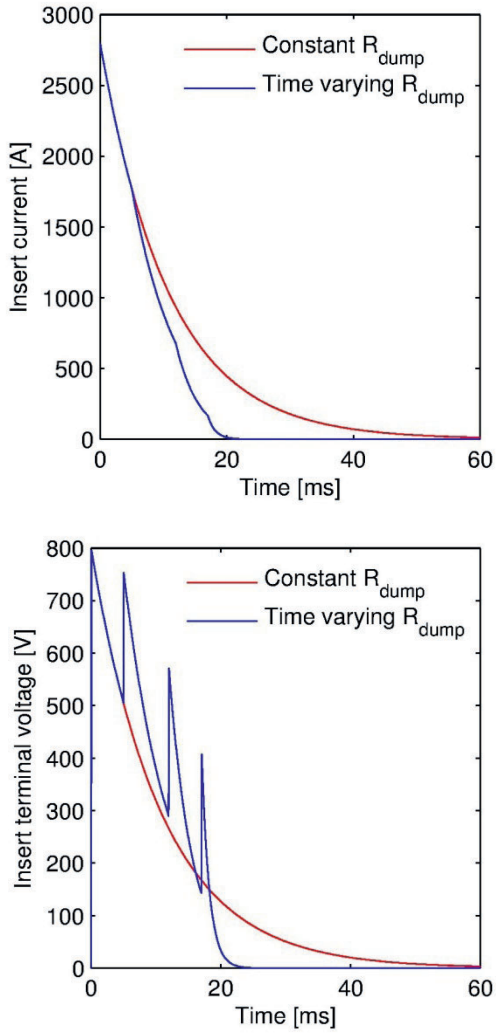

Figure 9: (a) insert current decay and (b) insert terminal voltage during insert rapid discharge.

DISCUSSION

Such a small YBCO coil is not difficult to protect, at least, if the tape has homogeneous critical current and in a long-term use does not quench due to very small local damage. However, the critical current characteristic of the cable is doubtful. No widely used scaling law for the critical current of long unit length YBCO tape over wide range of magnetic field, its angle and temperature is

available. Also, the tape properties vary from batch to batch depending on the doping of the coated conductor. Thus, the now used critical current hypersurface, including angular dependence of magnetic flux density, is not necessarily reliable.

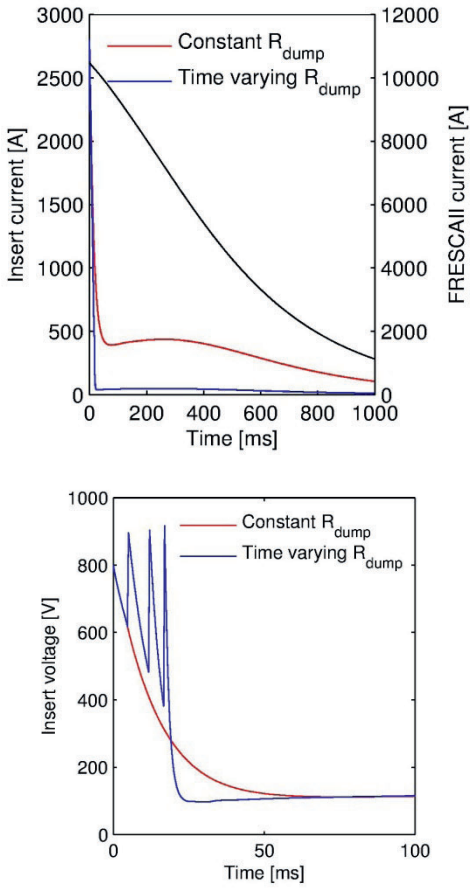

Figure 10: (a) FRESCA II [8] and insert current decay and (b) insert terminal voltage during FRESCA II quench.

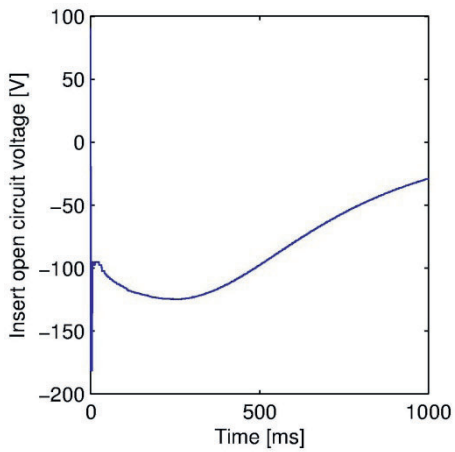

Figure 11: Insert open circuit voltage during FRESCA II quench.

Large HTS magnets can be very difficult to protect because quench heaters require high energies to ignite wide spread quench if compared to LTS counterparts. But before such detailed analysis can be performed, more fundamental research related to critical current hypersurface of coated conductors over wide range of parameters and heat generation at overcritical currents in YBCO is needed.

We also need to understand what kind of cable structures are beneficial for high current magnets and how current sharing occurs, because this has an important effect on the heat generation and thus normal zone propagation. Literature lacks this research especially in high field regime and at low temperatures. There is lot of quench related research of YBCO around 77 K but no conclusions should be drawn from these to 20 T region operation at 4.2 K.

In this work quench starting from the lowest critical current point was studied. Of course, the coil can quench also from the area where the field is parallel to the tape's wide surface, but this is highly unlikely, because the critical current of the cable at those regions is above 10 kA. Thus, a simulation at the low critical current region was only performed.

RECOMMENDATION FOR THE PROTECTION OF THE COIL

Because the coil operates at such a high current at 4.2 K, the protection of the coil should be easier than that of coils operating around 20 K or even at 77 K, where the higher volumetric specific heat increases considerably the stability margin and consequently the hot spot temperature at the quench detection time. However, there are uncertainties in the modelling related to the critical current surface. The angular dependence is estimated and the critical current is just scaled from the 4 mm wide tape to the presented cable.

Protection circuit

For simplicity, it is recommended to use only constant dump resistor for protection. The resistance should be sized according to the maximum allowed terminal voltage. If this value is 800 V, then the resistance is 0.28 Ω. However, to consider insert-outsert magnets of the future, research toward rapid discharge circuits could be started.

Quench detection

At least in several earlier HTS coils the quench detection proved to be problematic due to the very slow normal zone propagation. Regardless of this, it is expected that a quench in this coil can be detected from the terminal voltage. However, for safety, it is recommended that, in addition to the terminal voltage, voltages over each coil are monitored and three differential signals are formed from these to separate the inductive voltages during magnet loading and discharge. Then, each of these voltages should include only resistive part, and this voltage could be used directly for detecting the quench. Noise level should be considerably below 100 mV. There is a possibility of symmetric simultaneous quenches, for example, in the topmost and bottommost

pancakes, but then, the normal zone voltage grows twice as fast as in a single quench and therefore voltage allows quench detection.

The protection system of FRESCA II must also trigger the protection system of the insert and vice versa. Both systems can be launched in parallel, because it was shown that this causes no trouble to the insert. However, because the insert has much smaller energy than the FRESCA II and the coupling is good, high risk of damage to the insert and its power supply unit occurs, if the insert discharge switch does not open when the FRESCA II quench discharge begins. So there should be some redundancy for this aspect.

CONCLUSIONS

Quench in dipole YBCO insert producing 6 T in the background field of 13 T was considered. The magnet is being built within the EuCARD project framework and will be tested in the bore of FRESCA II facility. We found out that this coil can be quenched safely. This is mainly due to the very low inductance and high current which allows quite rapid quench detection and very rapid current decay. Basic constant dump resistor protection circuit was introduced for the magnet. Also, a protection circuit with time dependent dump resistor was considered. A quench in this YBCO insert was concluded to be safe event and in case of FRESCA II quench, a simultaneous discharge of the magnets can be carried out.

ACKNOWLEDGEMENTS

This work was supported by the European Commission under the FP7 Research Infrastructures project EuCARD, and is part of EuCARD Work Package 7: Superconducting High Field Magnets (HFM) for higher luminosities and energies.

REFERENCES

[1] J-M. Rey et al., HTS dipole insert developments, IEEE Trans. Appl. Supercond., vol. 23, 2013, in press, doi: 10.1109/TASC.2013.2237931.

[2] G. de Rijk, The EuCARD high field magnet project, IEEE Trans. Appl. Supercond., vol. 22, 2012, p. 4301204, doi: 10.1109/TASC.2011.2178220.

[3] T. Lecrevisse et al., Critical current and junction between pancake studies for HTS coil design, Physics Procedia, vol. 36, 2012, p. 681-686, doi: 10.1016/j.phpro.2012.06.267.

[4] E. Haro et al., Quench considerations and protectionscheme of a high field HTS dipole insert coil, IEEE Trans. Appl. Supercond., vol. 23, 2013, in press, doi: 10.1109/TASC.2012.2228890.

[5] A. Stenvall et al., Quench analysis of 6 T dipole YBCO insert coil at 13 T background field, Work in progress.

[6] E. Haro et al., Increasing reliability of quench simulations by using adaptive geometries, Abstract submitted to MT-23 conference, July 14-19 2013, Boston MA USA.

[7] E. Haro et al., Methods to speed-up quench simulations and their impact on computation time, Abstract submitted to MT-23 conference, July 14-19 2013, Boston MA USA.

[8] P. Fazilleau et al., Case study 5: Protection of FRESCA2, WAMSDO2013, these proceedings.

THE BEHAVIOUR OF COPPER IN VIEW OF RADIATION DAMAGE IN THE LHC LUMINOSITY UPGRADE

R. Flukiger, T. Spina, CERN, Geneva, Switzerland

Abstract

In view of the safe operation of the quadrupoles in the luminosity upgrade of the LHC accelerator, the response of the copper stabilizer at low temperatures to the various high energy radiation sources is of primary importance. The present study takes into account the expected high energy spectrum of the simultaneous radiation by neutrons, protons, pions, electrons and photons, calculated using the FLUKA code by F. Cerutti (CERN) as well as on literature values. It was found that proton irradiation causes a considerably higher damage than neutron irradiation: in spite of a 3.8% proton fraction, the measured damage is of the order of 20%, which fits with the calculations of N. Mokhov (Fermilab) on the contribution of protons to the dpa. The same calculations indicate that the total effect of protons, pions and electrons is at least as high as that of neutrons. Since recent neutron experiments of Nakamoto et al. show that the RRR of Cu is reduced from 200 to 50-120 for a fluence of 10^{21} n/cm^2, it follows that the inclusion of all high energy sources would lead to RRR values well below 50, thus endangering stability and protection. This result confirms the necessity of including a tungsten shield inside the quadrupoles.

INTRODUCTION

The operation of the luminosity upgrade of the LHC accelerator requires a rigorous control of the effects of high energy radiation on the performance of the quadrupole magnets. The stabilization problem is very complex, the quadrupoles being exposed to various radiation sources (photons, electrons, neutrons, protons and pions) over a broad energy spectrum reaching up to more than 10^3 GeV [1]. A main difficulty resides in the fact that these high energy sources act *simultaneously* on the quadrupoles. Since there is at present no facility where the effect of more than one radiation source at a time can be studied, the only possible analysis consists in a separate study of the effects of each singular radiation source on the quadrupole components, i.e. the Nb_3Sn superconductor, the Cu stabilizer and the insulator. At present, it is not yet possible to predict whether the combined effect due to high energy radiation sources can be simulated by the simple sum of each one of them. Nevertheless, there are reasons to think that that this approximation may be correct, taking into account that the dpa (displacement per atom) induced by the combined radiations during the lifetime of the quadrupoles is quite low, of the order of 10^{-4}.

The subject of the present paper is the description of the behavior of the Cu stabilizer present in the superconducting cable under the effect of the high energy irradiation in LHC Upgrade. Of particular interest is the enhancement of electrical resistivity, or in other words, the decrease of the Residual Resistivity Ratio (RRR). For Cu, the RRR is defined as the resistivity at room temperature divided by the one at 4.2 K, which is close to the 1.9 K operational temperature. The present study is based on a series of published works, relying on the radiation load inside of the quadrupole volume given by the calculations of F. Cerutti [1] with the FLUKA code [2]. These calculations show that there is a characteristic energy distribution for each one of the radiation sources mentioned above. The resulting radiation spectrum reaching the inner winding of Q2a (the quadrupole with the highest radiation load in the triplet, with an aperture of 150 mm) can be described by the fraction corresponding to each radiation source and the maximum energy of their respective distributions (Table 1).

Table 1: Radiation sources and track length fraction in LHC upgrade and approximate energies at the maximum of distribution

Radiation source	Track length fraction (%)	Energy at distribution maximum (MeV)
Photons	88	~ 0.5
Electrons/positrons	7	~1 – 10
Neutrons	4	1
Pions	0.45	100 - 200
Protons	0.15	100 - 200

The conditions inside the quadrupole winding vary for each one of the radiation sources. The gamma and neutron radiations will mainly traverse the magnet, in contrast to the charged particles: electrons and pions will be fully trapped. Protons show a more complex behavior: they will be almost fully trapped at energies below 100 MeV, where the penetration depth is of the order of the thickness of the inner winding (15 mm). The fact that the radiation sources acting on the quadrupoles have a wide distribution of energies renders the problem particularly difficult. Indeed, the presence of high energy gradients inside the windings leads to a highly inhomogeneous radiation damage, which will have strong consequences for the properties of the various quadrupole components, and thus also on the stabilizing Cu.

For LHC upgrade, the total absorbed radiation dose (in MGy = J/kg) has been calculated, as well as the number of dpa (displacements per atom), using the FLUKA code. The dpa value is not constant inside the inner coil of the quadrupole: a certain gradient is present as a consequence of the different particle energies and of the different penetration depths inside the coil. In order to guarantee a

safe operation, one has thus to take into account the maximum load, and the values of importance are the peak dose where the effects are highest. From the calculations given in [1] it follows that the high energy fluences inside the second quadrupole (Q2a) winding for neutrons, protons and pions for the target integrated luminosity of 3000 fb^{-1} will be approximately 2×10^{21} neutrons/m^2 and $>10^{20}$ p/m^2 for both protons and pions.

ELECTRICAL RESISTIVITY OF THE CU STABILIZER FOR DIFFERENT RADIATION SOURCES

A large quantity of data has been published in the last decades on the effects of the irradiation of Cu by various high energy sources and at various temperatures, from 4.2 K to room temperature. From the known literature data, the following conclusions can be drawn:

- The electrical resistivity $\rho(T)$ (and therefore the RRR value) of the Cu stabilizers in superconducting magnets is strongly affected by the various radiation sources (neutrons, protons and pions) The lowering of RRR after irradiation affects the quench stability and thus the protection scheme. The increase of resistivity in Cu can be explained by the generation of Frenkel pairs which change the scattering properties of conduction electrons: the electronic mean free path is reduced.
- The enhancement of electrical resistivity of Cu with irradiation depends strongly on the initial purity. The enhancement of resistivity (or decrease of the RRR) of Cu is considerably stronger for neutron irradiations at lower temperatures: the enhancement of electrical resistivity of high purity Cu (RRR ≥ 1'000) is of the order of 2 at room temperature and of ~ 5 at 77 K. Below 10 K, a factor of up to 50 was observed. In wires, with specified RRR values of the order of 150 - 200, the observed changes are considerably smaller.
- In order to be consistent with the behavior of magnets at 1.9 K, the following discussion will mainly consider data obtained on low temperature irradiations. After warming, a partial recovery of the RRR takes place: at 40 K, 30 - 50% of the RRR values are recovered (recovery stage I), depending on the initial state and purity of the Cu. Warming up to room temperature, the original RRR values are recovered up to ~ 90% (see Fig. 1).

Most known irradiation data on Cu been obtained on neutron irradiation. Due to the occurrence of various high energy radiation sources in LHC upgrade, it is important to evaluate the damage caused by each one of them. The energy loss due to atomic displacement as a particle traverses the material can be described by the Non-Ionizing Energy Loss (NIEL). The product of the NIEL and the particle fluence gives the displacement damage energy deposition per unit mass of material. This quantity has first been calculated for Si by van Ginneken [2] for various radiation sources, e.g. electrons, photons, neutrons, protons and pions. Si and GaAs are so far the only materials for which a detailed dependence of the NIEL for all these radiation sources has been published in detail. In the meantime, however, detailed calculations of the NIEL can already be performed by using the FLUKA transport code; this code has widely been applied for calculating the radiation load of the quadrupoles in LHC baseline and upgrade [1]. Although the conditions in Cu are very different from those encountered in Si, both material are crystalline, some general tendencies being expected to be similar. It appears from the calculations of van Ginneken [3] that for solid crystals, the NIEL by atomic displacement induced by electrons and photons is much smaller than that of neutrons, protons and pions, regardless of the particle energies. This tendency is also observed for the quadrupoles in the LHC upgrade.

Irradiation by high energy electrons and photons

Electron bombardment introduces isolated simple defects. As the electron energy increases, the probability for two or more point defects to form a cluster increases. As mentioned above, the effects of electron and photon irradiation on Cu are expected to be considerably smaller than those of neutrons, protons and pions. A literature study has been performed, but no data were found for the effect of high energy photon irradiation of Cu, in contrast to the effect of electron irradiation on the electrical resistivity of Cu, which has been studied by several authors. Sassin [4] showed that for electron energies of 2.8 MeV the initial RRR ratio of 800 decreased by a factor of 38 for a fluence of 1.15×10^{24} e/m^2. Taking into account that this fluence is > 100 times higher than the expected neutron fluence in LHC upgrade, the enhancement of the RRR ratio at equivalent electron fluences is expected to be considerably lower. The further considerations will be limited to the case of neutron and proton irradiation.

Irradiation by high energy neutrons

As mentioned above, warming up to room temperature of Cu after neutron irradiations at T< 10K leads to strong recovery of the physical properties: several authors found a recovery of ρ_o well above 90%. Guinan et al [5] and Horak et al. [6] have irradiated Cu samples characterized by RRR = 172 and 2'000, respectively. The irradiations were performed at 4.2 K with 14 MeV neutrons in the RTNS-II facility (fluence 10^{21} n/m^2) and at > 0.1 MeV (fluence 2×10^{22} n/m^2), respectively. The results are shown in Fig. 1. It should be mentioned here that the superconductor Nb_3Sn shows a markedly different recovery behavior: the recovery at 300 K is only of the order of 10%, full recovery occurring above 500°C.

Stage I recovery is generally attributed to recombination of close Frenkel pairs and to the long-range migration of interstitials. In Cu the recovery mechanism is probably related to the local situation of the close Frenkel pairs, which may be separated by at least

one stable lattice site beyond the spontaneous recombination radius (recombination will occur along the <110> or <100> directions). The total recovery in irradiated Cu is nearly identical for irradiations with 14 MeV neutrons (RTNS-II) and with reactor neutrons (> 0.1 MeV).

In a recent review article H. Weber [7] described the work of several authors on the behavior of the RRR of Cu after low temperature neutron irradiation. In particular, he mentioned the existence of a unique Kohler relation for Cu with RRR values close to the industrial ones. Kohler's rule states that the quantity $[\rho(B) - \rho(0)]/\rho(0)$ remains unchanged when increasing the impurity concentration c and the field B by the same factor. This dependence, i.e. $[\rho(B) - \rho(0)]/\rho(0)$ versus $B/\rho(0)$, where $\rho(0)$ is the zero-field resistivity, is important for predicting the evolution of ρ under various field and irradiation conditions, even for different RRR values prior to irradiation.

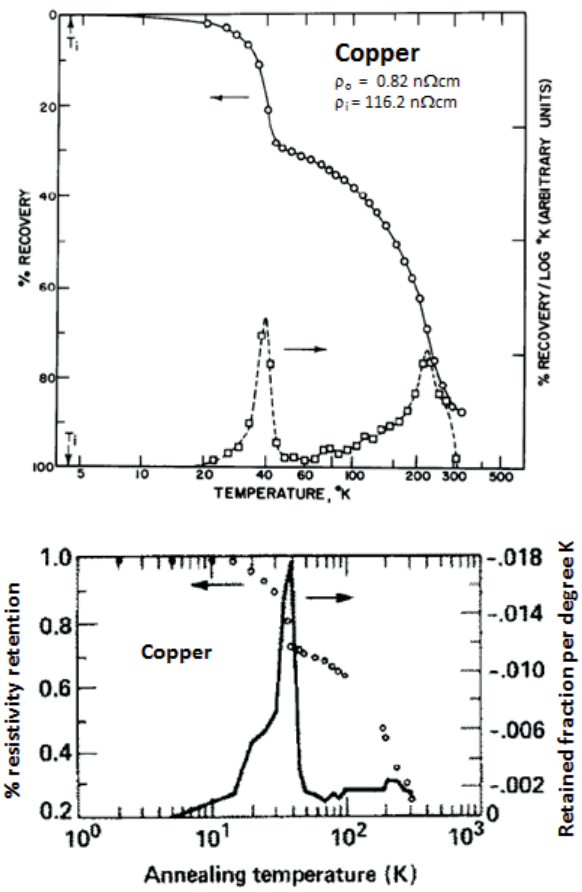

Figure 1: Post-irradiation, isochronal annealing results for Cu with different RRR values prior to irradiation, showing stage I recovery step at ~40 K. At 300 K, resistivity is recovered to 95% (Left: after Horak et al. [6], RRR = 2000; Right: after Guinan et al. [5], RRR = 100).

Recently, neutron irradiations on Cu have been performed at 14 K at KUR (Kyoto University Research Reactor Institute) at fluences up to of 2.8×10^{21} n/m^2 by Nakamoto et al. [8]. As illustrated in Fig. 3, the electrical resistance increased proportionally with fluence, increasing from 2.1 to 3.05 μΩ (~50%). These data can be compared with the data of Horak et al. [5] shown in Fig. 1 by introducing the degradation rate $\Delta\rho/\phi t$, the resistivity enhancement for the applied fluence. In spite of the very different initial RRR ratios (RRR = 2000 for Horak et al. [6] and 300 for Nakamoto et al. [8]), the results are quite similar, the values for the degradation rate $\Delta\rho/\phi t$ being 0.58 and 0.82×10^{-22} nΩm^3, respectively. Nakamoto et al. [8] have measured the effect of neutron irradiation at 10 K on the RRR of superconducting wires after different fluences and found an essential effect: An initial RRR ratio of 200 would decrease to RRR = 160-190 for a neutron fluence of 10^{20} n/m^2 and to RRR = 50-120 for 10^{21} n/m^2, the latter being close to the total neutron fluence expected in LHC upgrade.

A last point concerning the variation of the RRR ratio of irradiated Cu concerns its behavior in presence of magnetic field. The only results treating the increase of stabilizer resistivity with high energy radiation neutron fluence have been discussed for neutron irradiation by H. Weber [7] and are reproduced in Fig. 4, where the ratio $\rho(B)/\rho_o(B)$ between the resistivity $\rho(B)$ after irradiation at 5 K and that one before irradiation $\rho_o(B)$ is plotted as a function of neutron fluence. It is seen that the enhancement of $\rho(B)/\rho_o(B)$ with fluence in the presence of magnetic field is considerably reduced, as a consequence of the decrease of magnetoresistivity for increasing zero-field resistance after irradiation.

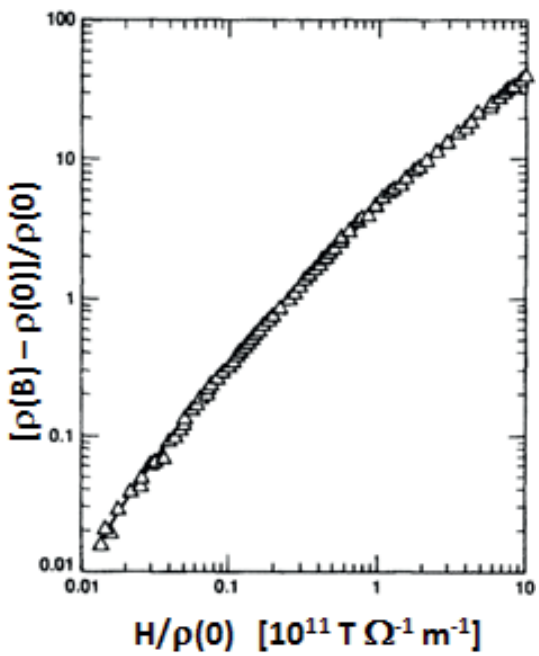

Figure 2: The Kohler plot for Cu samples for which the resistivity at zero field is entirely due to point defects (After Guinan et al. [5]).

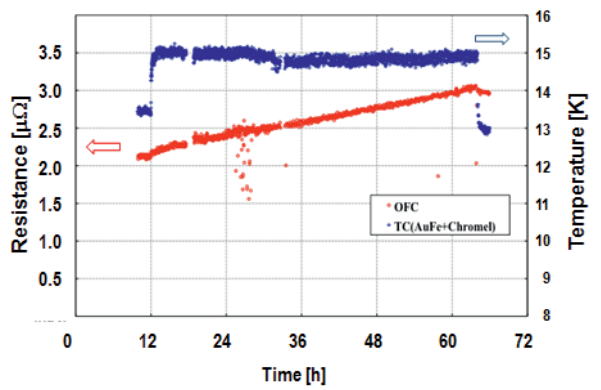

Figure 3: Enhancement of electrical resistance of Cu during irradiation at 14 K with fast neutrons (E>0.1 MeV). The temperature of 14 K was constant during the irradiation. This measurement has been extracted from the presentation of T. Nakamoto at the RESMM'12 [8].

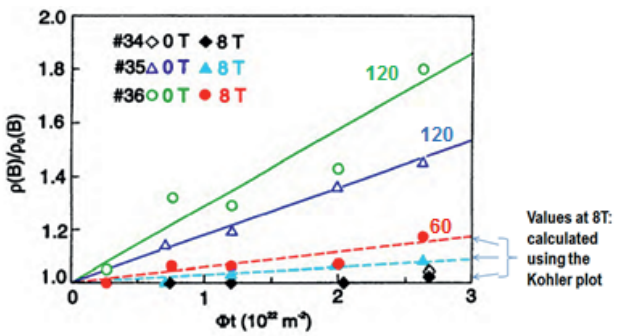

Figure 4: Increase of the electrical resistivity of the Cu stabilizer with neutron fluence (E > 0.1 MeV). The zero field data are measured, while the 8 T data were calculated from a Kohler plot. The data were obtained on Nb-Ti wires, but a similar effect is expected for Nb_3Sn wires. The RRR values for the sample #34, #35 and #36 prior to irradiation are indicated in the figure (from H. Weber [7]).

Irradiation by high energy protons

In contrast to neutrons, protons and pions are charged particles, thus Coulomb elastic scattering will take place, which will considerably change the interactions with matter. Taking into account secondary ions, using the PHITS [9] and the MARS code, Mokhov [10] has calculated the contributions of the various high energy particles to the average dpa. He found that the major contributors to dpa (40%) are sub-threshold particles (particles with E < 100 keV + all fragments). Other important contributions were found to arise from neutrons (26%), protons (5%) and pions (15%) (see Table 2). A comparison between the contributions of protons and of neutrons to the total dpa values in Table 2 shows a ratio of ~ 20%, which is much higher than the corresponding fraction of ~ 4% resulting from Table 2: it follows that the relative effect of proton irradiation on the physical properties of the irradiated materials is expected to be larger than for neutron irradiation.

Table 2: Mean energy, flux and dpa, averaged over four hot spots (data from Mokhov [10])

Particle j	<E> (GeV)	RMS (GeV)	Flux ($cm^{-2}s^{-1}$)	DPA/yr	DPA (%)
p	2.93	10.7	1.3e8	1.75e-5	5
n	0.22	3.7	2.3e9	8.24e-5	26
π, K	13.8	41.6	5.4e8	4.78e-5	15
μ	11.3	19.7	6.3e5	1.70e-9	-
γ	0.018	0.35	8.6e10	~2.e-5	6
e	0.077	0.5	9.8e9	2.47e-5	8
Sub-thresh.					40

In order to describe the situation in the Cu stabilizer in the quadrupoles under the effect of protons with very different proton energies, it is important to present very recent dpa calculations on proton irradiated Cu, by Fukahori et al. [11]. These authors have used the PHITS code for taking into account the fact that high energy protons induce the formation of secondary ions, or in other words nuclear reactions occur before the stopping range (or penetration depth) of the protons in Cu is reached. The behavior at 14, 50, 200 and 200 MeV is shown in Fig. 5. These graphs illustrate quite well what is going on in the Cu stabilizer of the quadrupoles, where protons of all energies are present: the classical Bragg peak only occurs for 14 and 50 MeV protons, an increasingly different behavior being expected at higher energies. The secondary ions create new PKA's (primary knock-on atoms), which in turn result in enhanced dpa values. Taking into account that the thickness of the inner coil of the quadrupoles has a thickness of 15 mm, it follows that the protons at lower energies will have a strong contribution to the dpa values.

Comparison between neutron and proton

The question arises about the relative effects of neutrons and protons on the RRR of the Cu stabilizer in LHC upgrade. There is no direct comparison between the electrical resistivities of Cu stabilized Nb_3Sn wires; the only comparative work was performed on the same Cu wire with a ratio RRR = 550 by Thompson et al. [12] (16 MeV protons at 4.2 K) and Roberto et al. [13] (15 MeV neutrons at 4.2 K). The RRR ratio is a factor ~ 2 higher than in Nb_3Sn wires, but is not thought to influence the following conclusions. These authors [12] found that the damage caused by the different radiation sources (neutrons or protons) can be compared using their respective slopes $d\Delta\rho_o/d\phi T$. From their results (Fig. 6), the ratio between the slopes for the neutron and the proton wires can be determined [12]:

$$\left.\frac{d\Delta\rho_0}{d\Phi T}\right|_n \Big/ \left.\frac{d\Delta\rho_0}{d\Phi T}\right|_p = 0.44$$

This ratio is approximately the same as the ratio between the corresponding damage energies cross sections E_{DC}, represented in Table 3.

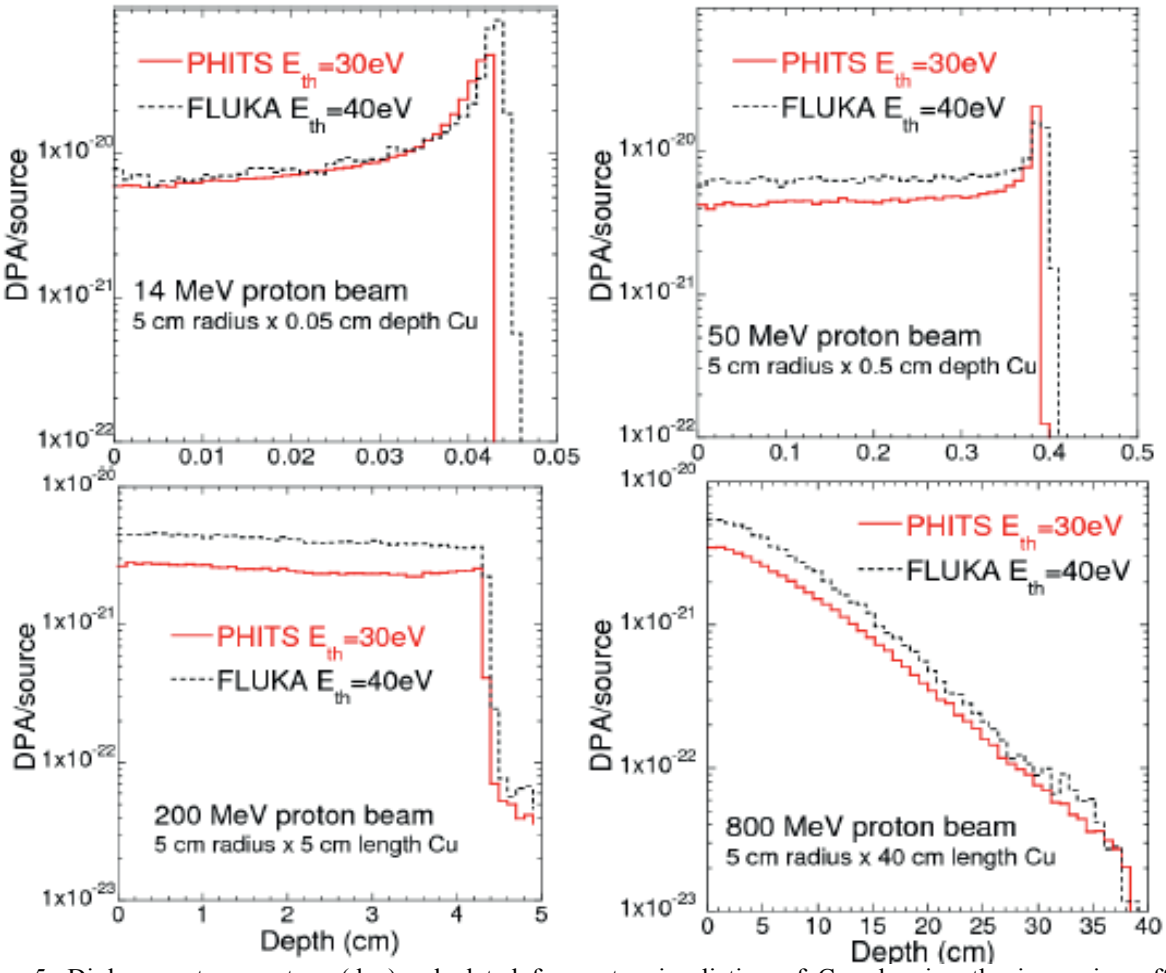

Figure 5: Diplacements per atom (dpa) calculated for proton irradiation of Cu, showing the increasing effect of secondary ions with increasing energies. Both PHITS and FLUKA codes yield comparable results (From Fukahori et al. [10]).

Table 3: Damage energy cross sections for 16 MeV neutrons (d-Be) [13], for 15 MeV protons [12] and for E>0.1 MeV neutrons [7]

Radiation source	Energy (MeV)	Damage energy cross sections E_{DC} (keV.barn)	Ref.
neutrons (d-Be)	15	263	13
protons	16	631	12
neutrons	>0.1	78	7

It was recently shown [14] that the ratio between the initial slopes $dT_c/d\phi t$ of various Nb_3Sn wires irradiated in two different reactors, RTNS-II (14MeV) and TRIGA (>0.1MeV), correspond roughly to the ratio between the corresponding damage energy cross sections, E_{DC}(14MeV)/E_D(<0.1MeV). Since the neutron spectrum for neutrons in LHC Upgrade (neutron energies centered at 1 MeV) is similar to that in a TRIGA Mark-II reactor with > 0.1 MeV neutrons [14], the same argument can be applied here, and one can extend the above comparison to the estimated damage energy cross section of Cu in the TRIGA reactor.

Since only the damage energy cross sections for Ti and Nb have been calculated so far, the value of Cu has been taken as an intermediate value between both: $E_{DC}(Nb_3Sn)$ ~ 75 keV · barn (see Table 3). The slope $d\Delta\rho_o/d\phi T$ corresponding to the lower damage energy for the 1 MeV neutrons has been plotted in Fig. 6. The present development constitutes only a first approximation, but indicates clearly that the same amount of damage on Cu wires (represented by $\Delta\rho/\rho$) produced by 16 MeV protons occurs at fluences a factor of 6 - 7 lower than for the 1 MeV neutrons produced in LHC Upgrade. It follows that in spite of the considerably lower proton fraction (3.8%) with respect to that of neutrons, the former induce a sizeable change of $\Delta\rho/\rho$ on the stabilizer, thus inducing an additional lowering of the RRR ratio. This confirms the dpa calculations of N. Mokhov shown in Table 2, where the percentage of total dpa caused by protons (Table 1) with respect to that of neutrons is 20%, i.e. much higher than the corresponding proton fraction.

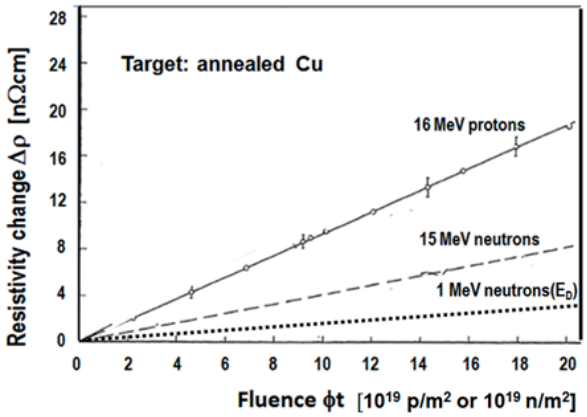

Figure 6: Enhancement of resistivity of Cu with RRR = 550 by 16 MeV neutrons [13] and by 15 MeV protons [12]. The dotted line at 1 MeV has been calculated assuming a ratio $E_{DC}(15MeV)/E_{DC}(1MeV) = 3.6$ [7].

Irradiation by high energy pions

Since there is no source with a sufficient pion flux to reach in reasonable time the fluences larger than the 10^{20} pions/m^2 expected in LHC upgrade, the effect can only be calculated. Supposing that the stopping range for the totality of pions falls inside of the quadrupole, Mokhov [10] calculated the contribution of pions on the total calculated dpa, based on the MARS code [15] and found ~ 15% (see Table 2). This is almost a factor three higher than the proton contribution. His results, listed in Table 2 for all high energy radiation sources, can now be used to get a rough estimation of the behavior of the Cu stabilizer in the quadrupoles. It follows that the total enhancement of the electrical resistivity of Cu due to the combined effect of protons and pions is almost as high as that one due to neutrons.

CONCLUSIONS

Based on literature data, the effects of high energy irradiation on the Cu stabilizer in LHC upgrade have been briefly discussed. A common point to all radiation sources is the sizeable decrease of the RRR ratio with fluence, regardless of the high energy source and the irradiation temperature T_i. In contrast to the properties of Nb_3Sn, where there is little difference between irradiation at low temperature (T< 10 K) and 300 K, the properties of Cu (e.g. electrical resistivity, hardness, lattice parameter) exhibit an almost complete recovery when warming up to 300 K.

The present data allow an approximate view of the total damage of the various high energy sources in LHC upgrade on Cu, taking into account the effect of each single source on the dpa values as shown in Table 2. After a neutron fluence of 10^{21} n/m^2, Nakamoto [7] reported an already important effect, the starting ratio RRR = 200 being decreased to values between 50 and 120. Since the combined effect of protons and pions is almost as important as that one caused by neutron irradiation, this means that these values would be further lowered to extremely low values that could endanger stability and protection, even without taking into account the effect of the subthreshold particles (E < 100 keV). The effect of the latter is not known yet, but due to their high contribution to the dpa values (40%), an additional decrease has to be expected.

The question arises about the possibilities to maintain the RRR ratio at reasonable values. A periodic warming up the quadrupoles to 300 K could be considered, but the safer solution consists in inserting an internal shield to protect the quadrupole coils. This possibility is presently under study.

REFERENCES

[1] F. Cerutti, A. Lechner, A. Mereghetti, M. Brugger, Particle fluence on LHC magnets, WAMSDO workshop, CERN, 4.11.2012, Geneva, Switzerland.

[2] A. Fasso, A. Ferrari, G. Smirnov, F. Sommerer, V. Vlachoudis, FLUKA realistic modeling of radiation induced damage, Progr. Nucl. Science and Technol., 2.769 (2011).

[3] A. van Ginneken, Non Ionizing Energy Deposition in Silicon for Radiation Damage Studies, Fermilab report Nr. 522, October 1989.

[4] W. Sassin, Defektaufbau in Kupfer und Aluminium bei Tieftemperatur-Elektronen-Bestrahlung, Jülich Report 586, April 1969.

[5] M.W. Guinan, J.H. Kinney and R.A. Van Konynenburg, J. Nucl. Mater., 133 & 134, 357 (1985).

[6] J.A. Horak, T.H. Blewitt, Isochronal recovery of fast neutron irradiated metals, J. Nucl. Mater., 49, 161 (1973/74).

[7] H. W. Weber, Int. J. Mod. Phys. E 20, 1325 (2011).

[8] T. Nakamoto Radiation Effects in Magnets, presented at Radiation Effects in Superconducting Magnet Materials Workshop (RESMM'12), 13.-15.2.2012, Fermilab, USA.

[9] Y. Iwamoto, K. Niita, T. Sawai, R.M. Ronningen, T. Baumann, Displacement damage calculations in PHITS for copper irradiated with charged particles and neutrons, Nucl. Instr. and Methods in Phys. Res., B (2012).

[10] N. Mokhov, A. Konobeyev, V. Pronskikh and S. Striganov, Exploring Parameter Space for Radiation Effects in SC Magnets, WAMSDO workshop, CERN, 4.11.2012, Geneva, Switzerland.

[11] T. Fukahori, Y. Iwamoto, A calculation method of PKA, KERMA and DPA from evaluated nuclear data with an effective single particle emission approximation (ESPEA) & Introduction of Event Generator Mode in PHITS Code, presented at IAEA/TM on Primary Radiation Damage: from nuclear reaction to point defect, 1-4 Oct. 2012, VIC, Room A2712, IAEA, Vienna, Austria.

[12] D. A. Thompson, A. M. Omar, J. E. Robinson, 10-16 MeV proton irradiation damage in Fe and Cu, J. Nucl. Mater., 85 - 86, 509(1979).

[13] J. B. Roberto, C. E. Klabunde, J. M. Williams, R. R. Coltman, M. J. Saltmarsh, C. B. Fulmer, Electrical resistivity of small dislocation loops in irradiated Cu, Appl. Phys. Lett., 30, 509 (1977).

[14] R. Flükiger, T. Baumgartner, M. Eisterer, H.W. Weber, T. Spina, C. Scheuerlein, C. Senatore, A. Ballarino and L. Bottura, Variation of $(J_c/J_{c0})_{max}$ of binary and ternary alloyed RRP and PIT Nb_3Sn wires exposed to fast neutron irradiation at ambient reactor temperature, presented at ASC2012, to be published in IEEE Trans. Appl. Supercond., 2013.

[15] N. V. Mokhov and O. E. Krivosheev, MARS Code Status, FERMILAB-Conf-008/181, August 2000.